UNIVERSITY OF MINNESOTA
ST. ANTHONY FALLS LABORATORY
Engineering, Environmental and Geophysical Fluid Dynamics

PROJECT REPORT 486

Testing of a 1:6 Scale Physical Model of the Large, Low-Noise Cavitation Tunnel (LOCAT)

By

Martin Wosnik and Roger Arndt

Prepared for
Maritime and Ocean Engineering and Research Institute (MOERI)
Republic of Korea

November 2006
Minneapolis, Minnesota

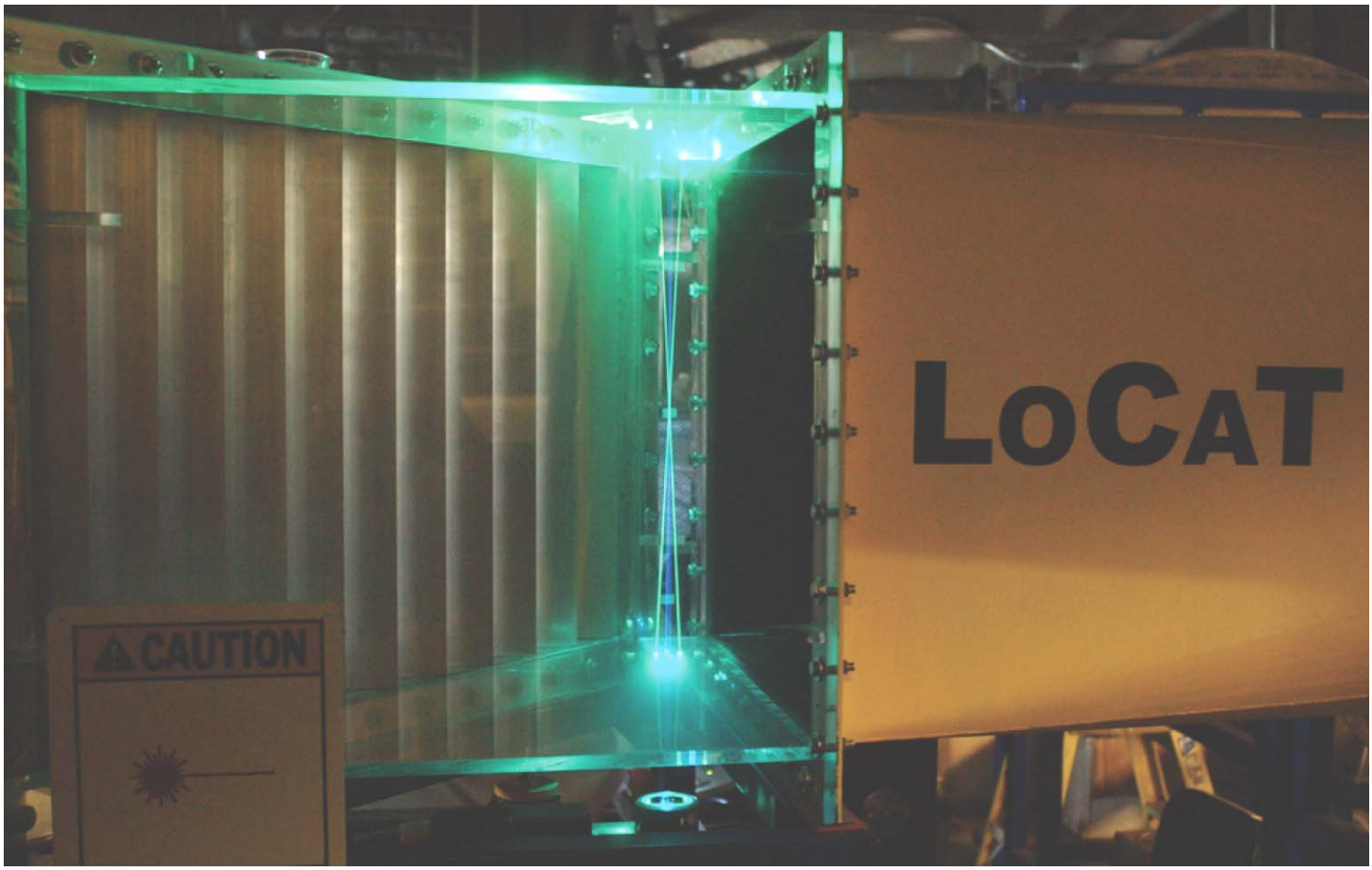
LoCaT
CAUTION

Abstract

As part of the conceptual and detailed design phases leading to the construction of the **LO**w Noise Large **CA**vitation **T**unnel (LOCAT) at the Maritime and Ocean Engineering and Research Institute (MOERI) of the Republic of Korea, an experimental analysis and verification of the design was carried out at the St. Anthony Falls Laboratory (SAFL). This report describes pressure and velocity measurements performed at a 1:6 scale physical model at SAFL using air as a working fluid.

The physical model is used to check the overall flow quality, including measurements of pump inflow, and to investigate contraction, diffuser and turning vane performance. High spatial resolution mean velocity and turbulence profiles were taken at 44 locations in the model, and mean pressure was measured at 183 locations. Here these results are summarized, and recommendations are made based on the experimental observations.

The results of the physical model can be used for comparison to numerical simulations at model Reynolds number, which can then be extrapolated to prototype Reynolds numbers to predict the performance of the full scale LOCAT.

Acknowledgements

The work reported herein was supported by Maritime and Ocean Engineering and Research Institute (MOERI) of the Republic of Korea. Dr. Jin Kim from MOERI was the project officer. We also thank Todd Barnacle, Mike Plante, Alex Ding, Chris Ellis, Jim Tucker and James Mullin of the St. Anthony Falls Laboratory for their contribution to the instrumentation of the tunnel.

Table of Contents

List of Figures

List of Tables

1. Introduction

As part of the conceptual and detailed design phases leading to the construction of the **LO**w Noise Large **CA**vitation **T**unnel (LOCAT) at the Maritime and Ocean Engineering and Research Institute (MOERI)[1] of the Republic of Korea (South Korea), an experimental analysis and verification of the design was carried out at the St. Anthony Falls Laboratory (SAFL). This report describes pressure and velocity measurements performed in a 1:6 scale physical model at SAFL using air as a working fluid.

LOCAT is an acronym for a water tunnel that will be used for both hydro-acoustic and cavitation testing. It has a somewhat different configuration than conventional water tunnels, and therefore requires considerable analysis, simulation and experimentation. The experimental analysis and verification will be coordinated with the analytic effort and numerical simulations. This project will draw on experience with similar models built and tested at SAFL, such as HYKAT and LCC (Wetzel and Arndt, 1994a and 1994b). The general layout of the LOCAT physical model is similar to the HYKAT facility previously modeled at SAFL (Song et al. 1987, Song et al. 1988). The flow loop of the LOCAT prototype is shown in Figure 1.

The overall size, operating range and design objectives of the LOCAT water tunnel prototype are as follows:

- Overall size: Length 60.0m, height 19.5 m, maximum width 5.8 m
- Test section dimensions: Width 2.8m, height 1.8m, length 12.5 m
- Maximum flow velocity in the test section: 15 m/s
- Static pressure Range 20 - 400 kPa (0.2 - 4 bar)
- Flow uniformity in the test section of less that 1% of the mean velocity
- Turbulence intensity in the test section of less than 0.2%

[1] Until recently MOERI was known as Korea Research Institute of Ships and Ocean Engineering (KRISO). MOERI performs Research & Development in the field of ship and offshore technologies. It is located in Daejeon City, and is an affiliated branch of the Korean Ocean Research and Development Institute (KORDI).

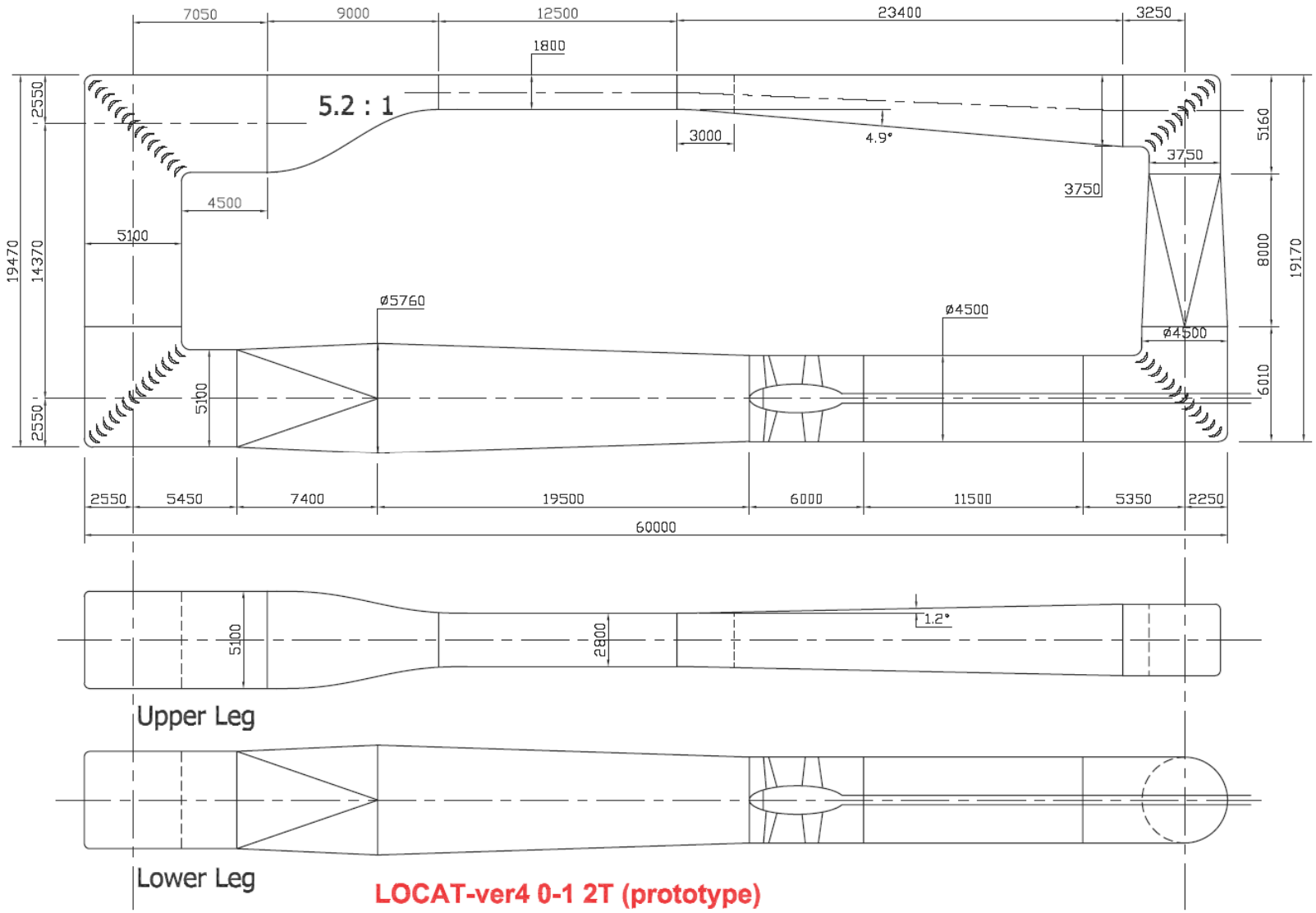

Figure 1. Flow loop of LOCAT prototype (version 4, with 2.0T vanes).

2. The 1:6 scale LOCAT physical model

2.1. Proposal for a physical model

A physical model of the proposed LOCAT water tunnel was to be built and tested with air as a working medium to save on structural cost. The scale was chosen to be 1:6 so that the model would fit in an available space on the turbine mezzanine level at SAFL and allow just enough room for instrumentation and measurements. A Reynolds number based on test section velocity and height, Re_H, can be defined as

$$Re_H = \frac{U_{max} H}{\nu} \tag{1}$$

Based on model size, loss factors and available fan an initial estimate of the maximum achievable model test section velocity was $U_{max,model} \approx 45$m/s. Thus the ratio of prototype and model Reynolds numbers becomes

$$\frac{Re_H}{Re_{H,model}} = \frac{\frac{U_{max} H}{\nu_{H_2O}}}{\frac{3 U_{max} \frac{1}{6} H}{15 \nu_{H_2O}}} \approx 30 \tag{2}$$

Therefore, the LOCAT physical model will approximately be a 1:30 dynamical model. The results of the physical model will be compared to a numerical simulation at model Reynolds number. This numerical simulation will then be extrapolated to prototype Reynolds numbers to predict the performance of the full scale LOCAT.

The 1:6 physical air model will focus on diffuser performance and will be used to check the overall flow quality, including measurements of the pump inflow. It was proposed to measure mean velocity, mean pressure and turbulence levels at the positions shown in Figure 2.[2] A series of pressure taps would be installed to measure pressure distribution of the contraction, the test section and the diffuser as shown. A fan, positioned as shown, was to be used to induce flow

[2] Figure 2 was presented in the beginning of the project when the scope of the work was being specified. The number of velocity and pressure measurements actually performed increased substantially during the project. For example, proposed at the pump inlet were 5 azimuthal locations with 6 radial positions each (=30 velocity measurements), actually performed and reported were 12 azimuthal locations with 58 radial positions each (=696 velocity measurements).

through the model (a “suck-down” facility). The water tunnel pump had not been specified yet when the LOCAT physical model was designed and will therefore not be modelled. However, since Laser Doppler Velocimetry (LDV) was chosen for the velocity measurements for a variety of reasons, the flow loop needed to be closed to contain the LDV seeding.

2.2. Design and construction of the 1:6 physical model

The LOCAT physical model was designed to fit in an available space on the turbine mezzanine level next to the SAFL high speed water tunnel. Initially a design on a scale of 1:5.7 was tried to maximize model size. Eventually, however, a scale of 1:6 was chosen to allow for better access with instrumentation, e.g., to permit the full range of radial traversing required in the round sections of corner #2 and the pump inlet. The layout of the model in the laboratory is shown in Figure 3. Note that the LDV optical bench and electronics were positioned so that all measurement locations could be reached by just moving the fiber optic probe. The model was laid on its side, with the plane of symmetry at a height of 65” (1.651m). Compared to the prototype drawing of Figure 1, and the earlier model drawing of Figure 2, it was flipped along its longitudinal axis.

The LOCAT physical model built at SAFL is shown in Figures 4, 5 and 6. Figure 4 shows a side and top view of the physical model shell (it even shows the LDV installed on the radial traversing plate at the pump inlet). The flow circuit was completed by a large diameter round section after the fan, which led into a seeding containment box. Screens break up large flow structures of the “fan signature”, and the flow enters the model via a bell-mouth. The yellow lines indicate where the part that is actually modeled begins (upstream of corner #4) and where it ends (at the pump inlet). Figure 5 shows a three dimensional view of the assembled physical model. The color coding, also used in painting the model, shows the modeled parts in yellow and light blue (=clear acrylic), and the non-model parts used to complete the flow loop in light gray and red. The supports, used to raise the model to a center-plane height of 65” (1.651m) and to mount the traversing slides for the LDV velocity measurements are shown in dark blue. Figure 6 shows a picture of the completed physical model at SAFL.

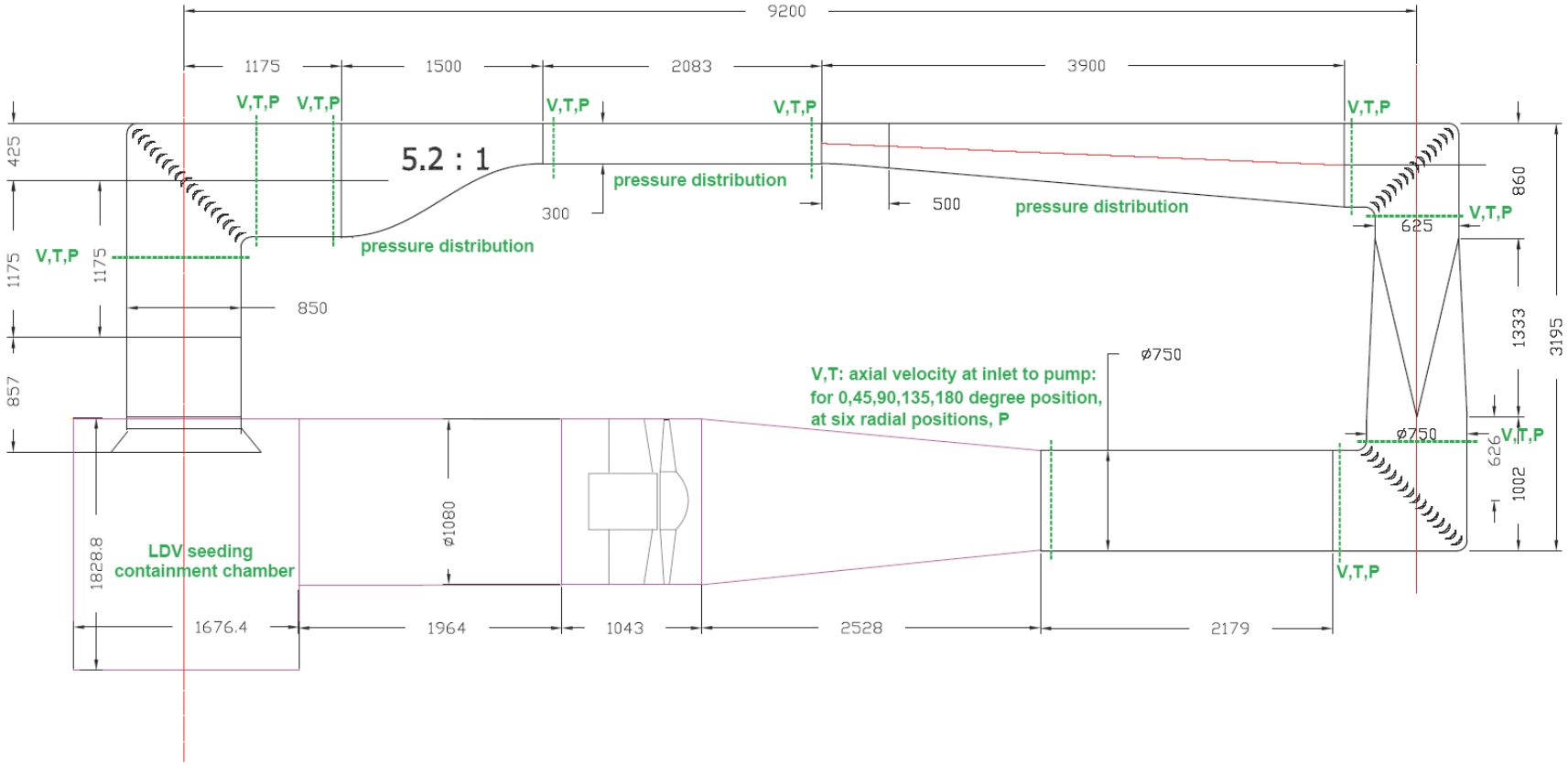

LOCAT-ver4.0-1 5T (MODEL LAYOUT)

Measurement Locations for LOCAT physical model: V-velocity, T-turbulence, P-pressure

Figure 2. Proposed measurement locations. This drawing of the LOCAT physical model (version 4, with 1.5T vanes) dates from early in the project when the scope of the work was being specified. Note that the actual model design, and the actual number of velocity and pressure measurements differ from the ones shown here.

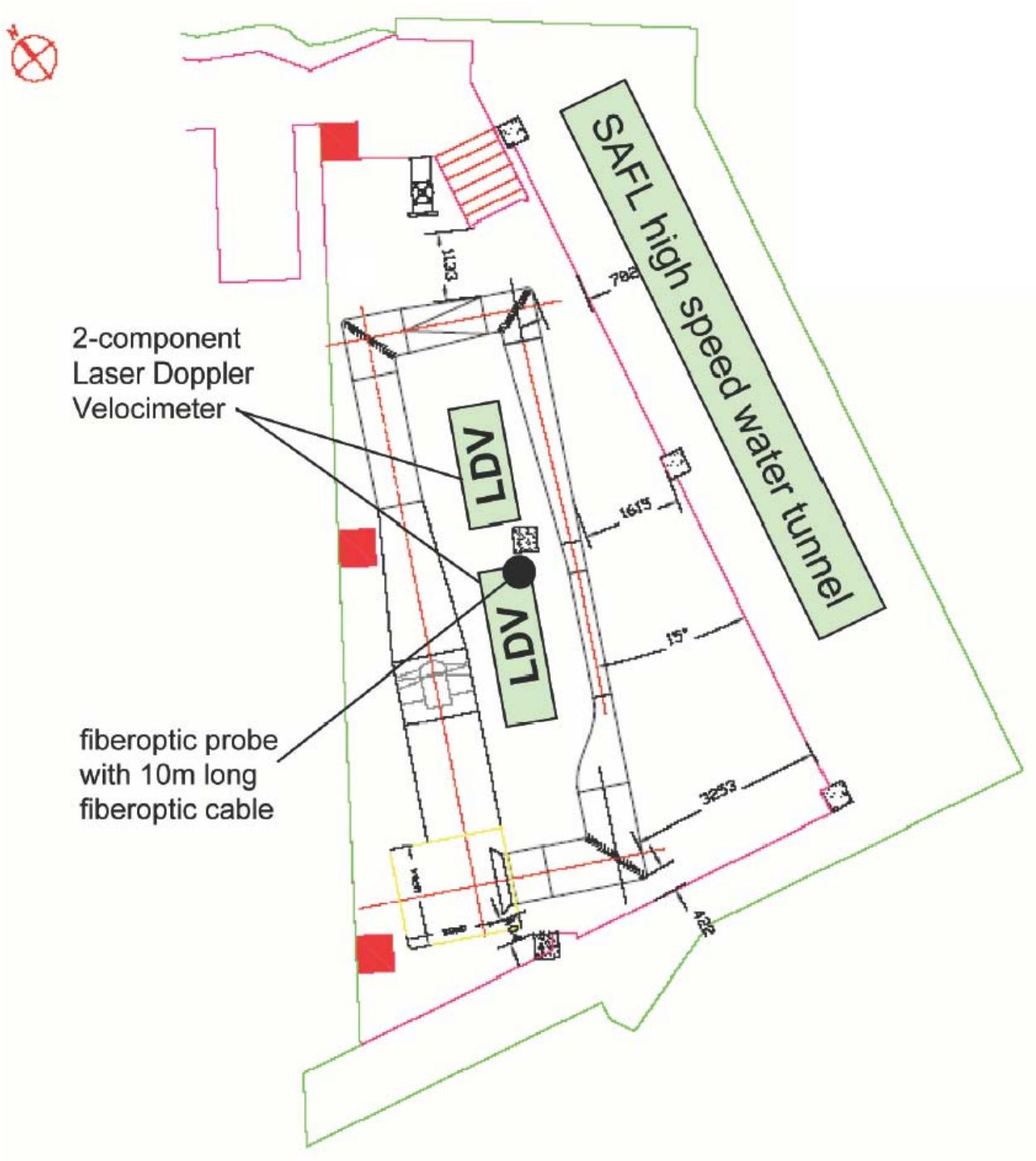

Figure 3. LOCAT 1:6 physical model layout in laboratory.

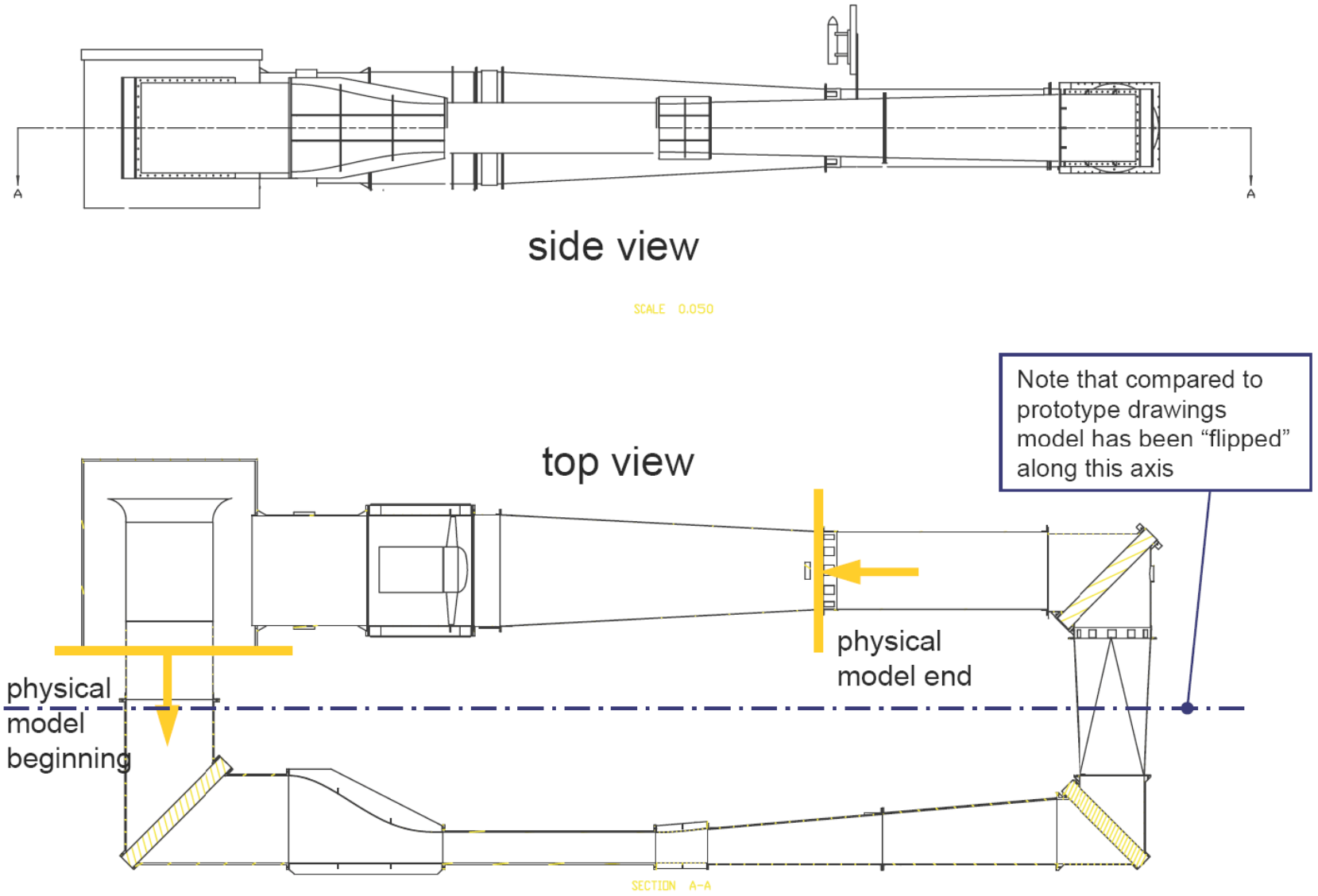

Figure 4. LOCAT 1:6 physical model drawing, side and top view.

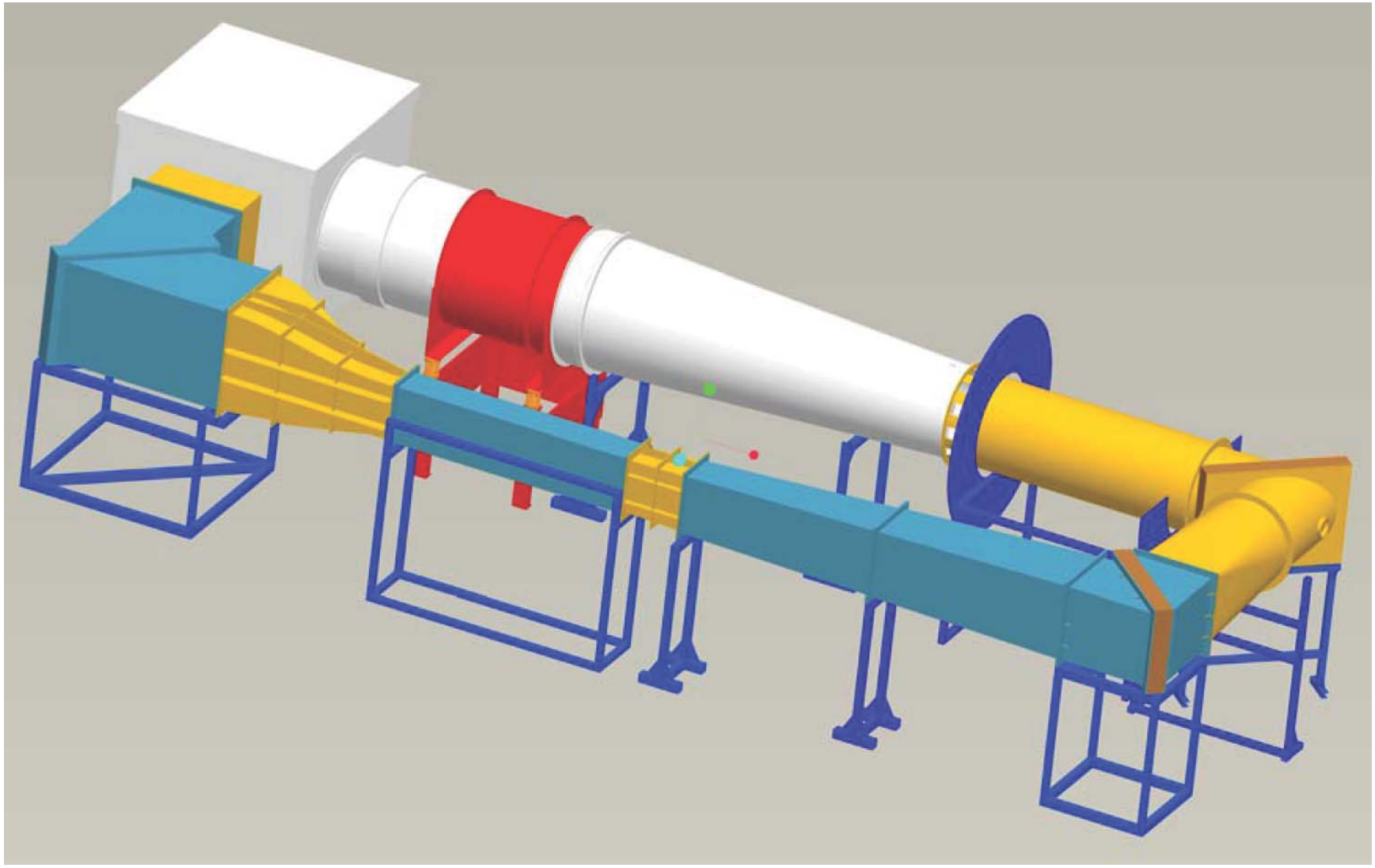

Figure 5. LOCAT 1:6 physical model drawing, 3D assembly. Yellow and blue (clear) colored parts are modeled, light gray and red are not.

Figure 6. LOCAT 1:6 physical model at St. Anthony Falls Laboratory.

The two main materials used in the construction of the model were 1/8" (3.2mm) soft steel for the contraction, transition, square-to-round transition, round corner, pump inlet and flow loop connection pieces, and 1/2" (12.7mm) polycast clear acrylic for the rectangular corners, test section and diffuser. Details of the design, construction and instrumentation of the 1:6 LOCAT physical model are reported in Wosnik et al. (2006). Key aspect of the design, construction and instrumentation will be mentioned in this report where necessary or appropriate.

2.3. Test conditions

2.3.1. Model test Reynolds number $Re_{H,model}$

The LOCAT physical model test section velocity vs. AC drive frequency is shown in Figure 7. It can be seen that the wind tunnel performed slightly better than estimated with a maximum test section velocity around 53m/s. A drive frequency of 48Hz was chosen as operating point for the measurement series. At 60 Hz the fan RPM was near the allowable short-term maximum RPM, whereas at a drive frequency of 48 Hz the fan was closer to (slightly above) its maximum RPM for continuous operation. This came at a cost of a slight reduction in Reynolds number, but was thought to be a safe choice since the model had to run continuously for many hours at a time. The air circulating in the LOCAT model will heat up over time due to dissipation, as the model wind tunnel is not equipped with a cooling system. Due to the simultaneous reduction of air density in the test section with increasing temperature, the test section velocity remained remarkably constant over time, as can be seen in Figure 8. However, the increase in absolute viscosity of air with temperature cannot quite compensate for the decrease in density, c.f. Figure 9. Therefore the physical model Reynolds number decreases slowly with run time, as shown in Figure 10.

In the final measurement programs for pressure and velocity reported here, the physical model was always started up first. Then various tasks such as mounting and alignment of the traversing system, alignment of the fiberoptic couplers of the LDV, seeding adjustment, test runs of the scanivalve assemblies, etc., were completed. When actual measurements were taken, the wind tunnel had been running at least for 90 minutes. From Figures 8 through 10 it can be seen that after 90 minutes – while not yet in steady state – the temperature variation, and with it the change of thermophysical properties of air and Reynolds number, was relatively small. In the

performance-benchmarking run shown in Figure 8 (1 June 2006) the test section velocity, measured with a pitot tube at x = 235 mm from the test section entrance (test section entrance = flange between contraction and test section), on the plane of symmetry at a distance of 50mm from the top wall (y/H=0.83), was steady at 41.9m/s (for the period from 90 minutes to 260 minutes of operation, $U_{average,TS,50mm}$ = 41.929m/s, $U_{StdDev,TS,50mm}$ = 0.008m/s). This corresponds to a centerline velocity of 42.2 m/s.

The actual physical model Reynolds number based on test section height and centerline velocity is then

$$Re_{H,model} = \frac{U_{TS,m} H_m}{\nu_m} = 0.766 \times 10^6 \qquad \left[\text{range: } 0.771 \ldots 0.762 \times 10^6\right] \tag{3}$$

With a prototype Reynolds number Re_H = 23.7 × 10^6 (at 15º C) the Reynolds number ratio between prototype and model becomes

$$\frac{Re_H}{Re_{H,model}} = \frac{23.7 \times 10^6}{0.766 \times 10^6} = 31 \tag{4}$$

The 1:6 scale physical air model as tested (at 48Hz AC drive frequency) and reported here is a **1:31 dynamical model** of the LOCAT prototype.

2.3.2. Turning vane angles of attack

Early results from numerical modeling (Song, 2006) showed that the turning vanes at design angle of attack were under-turning the flow somewhat in corners 1 and 2. The preliminary numerical results showed that an angle of attack of 2 or 3 degrees off the design angle of attack should work better. With the leading edge of the turning vane on the left, this angle change would be positive in an aerodynamic sense, i.e., the leading edge of the "wing" goes "up" with respect to the approaching flow, but negative in a mathematical sense in a right-hand coordinate system, i.e., turning clockwise around an axis pointing out of the drawing plane. A mechanism consisting of a pivot-bar and precisely machined spacers was installed that allowed the turning vane angle of attack to be changed, in an aerodynamic sense, from −2º to +6º in corners No. 1 and 4 (however, machined foam pieces in corner No. 2 – used to create an elliptical corner while

maintaining adjustable turning vane angle of attack – restricted the angle range from approximately −1º to +3º in that corner, c.f. Wosnik et al. (2006)).

The turning vane angle of attack for the data reported here was set +2º from the design angle of attack, in an aerodynamic sense, in corners 1 and 2, and was left at design angle of attack in corner 4 (upstream of the contraction). The turning vane angle of attack settings are summarized in Table 1. Experimentally verifiable angles are shown in Figure 11. The angle α was checked after the angle of attack was changed with the external mechanism (pivot-bar and spacers) from 0 to 2 degrees, and was found to be accurate to the target value to within the accuracy of the protractor used (0.25 degrees). The measured angles for corner No. 1 are shown in Table 2, an angle measurement with a protractor is shown in Figure 12.

Table 1. Turning vane angles of attack (AoA).

corner	α	ΔAoA (off design AoA)
1	82.9	+2 aerodyn. (-2 math.)
2	82.9	+2 aerodyn. (-2 math.)
4	84.9	0

Table 2. Turning vane angles in corner No. 1: angle α measured with a protractor (0.25º steps) after setting angle externally with spacer. Target value is 82.9º.

turning vane No. (from outside corner)	angle α as in Figure 11
1	82.75
2	82.75
3	83.0
4	83.0
5	83.0
6	83.0
7	83.0
8	83.0
9	82.75
10	83.0

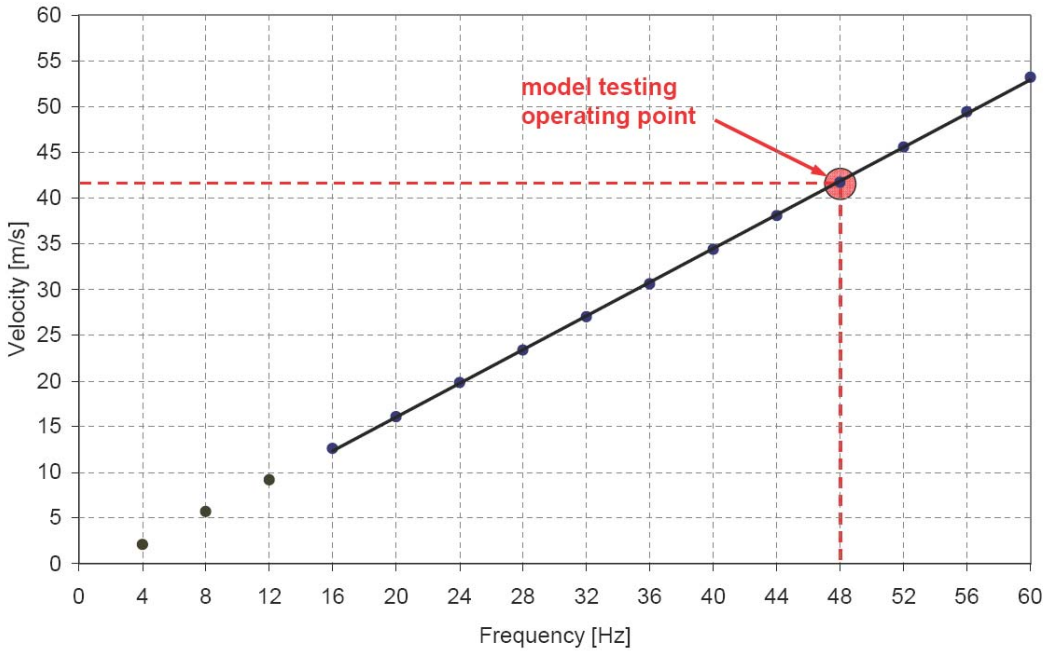

Figure 7. LOCAT physical model performance: Test section velocity vs. drive frequency (velocity measured with pitot tube on plane of symmetry at *y/H*=0.83).

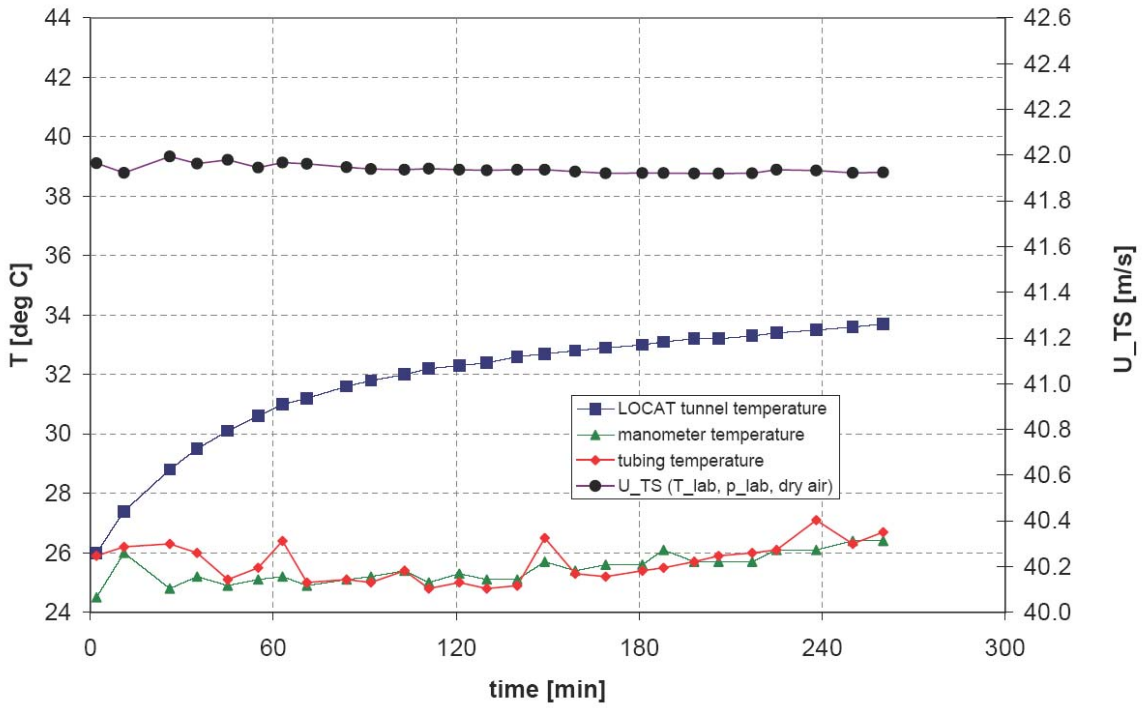

Figure 8. LOCAT physical model performance: Test section velocity and tunnel temperature vs. run time (velocity measured with pitot tube on plane of symmetry at *y/H*=0.83).

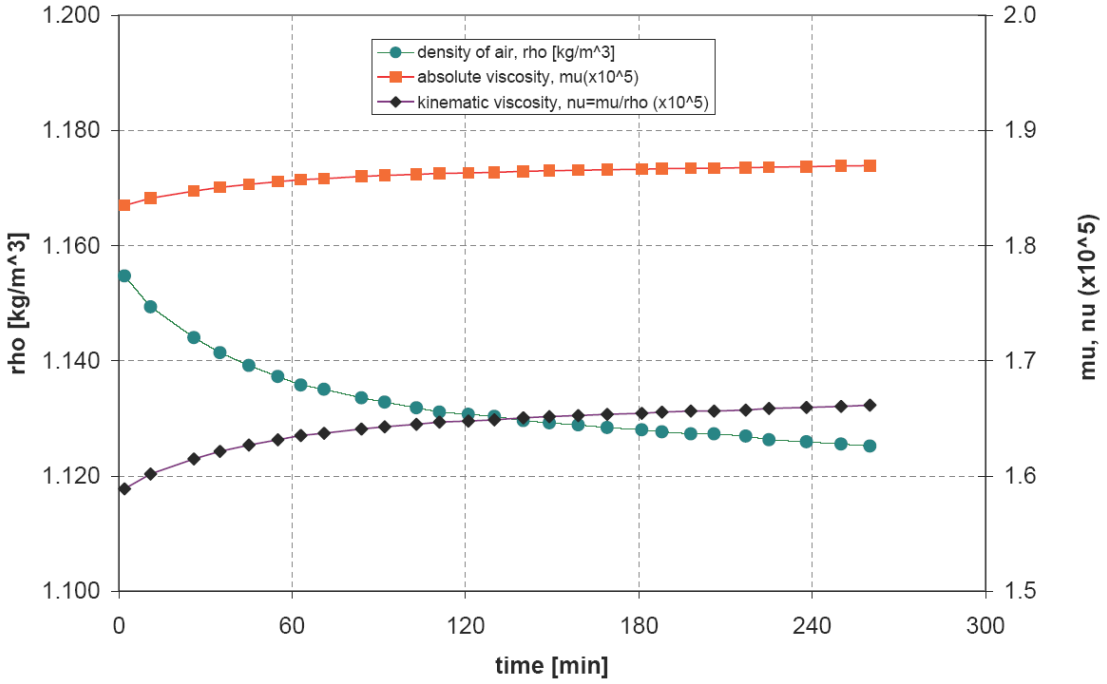

Figure 9. LOCAT physical model performance: Thermophysical properties of working fluid (air) vs. run time.

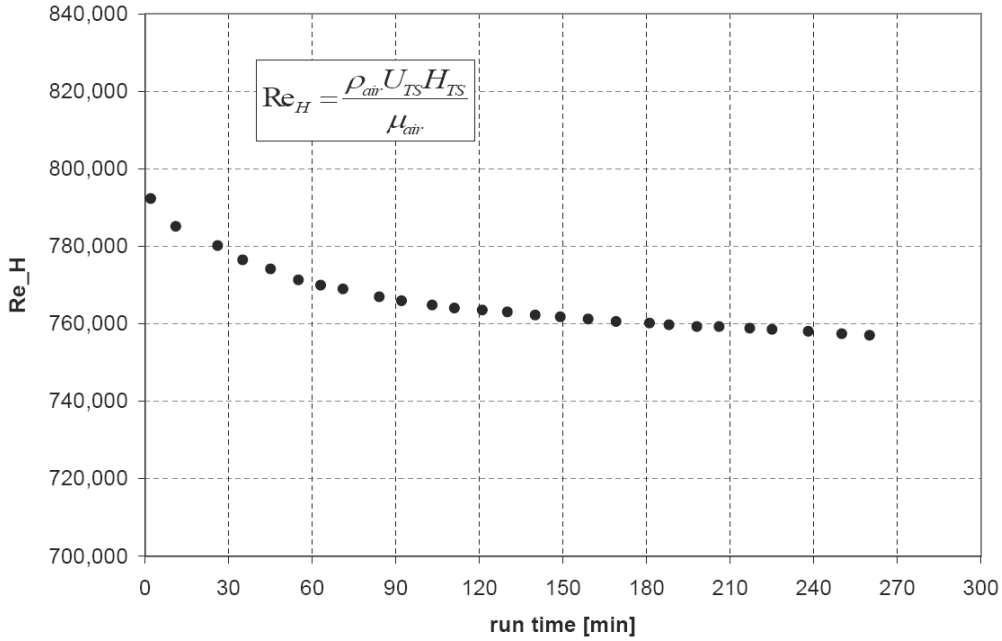

Figure 10. LOCAT physical model performance: Reynolds number based on test section height and velocity vs. run time (reference test section velocity measured with pitot tube on plane of symmetry at y/H=0.83).

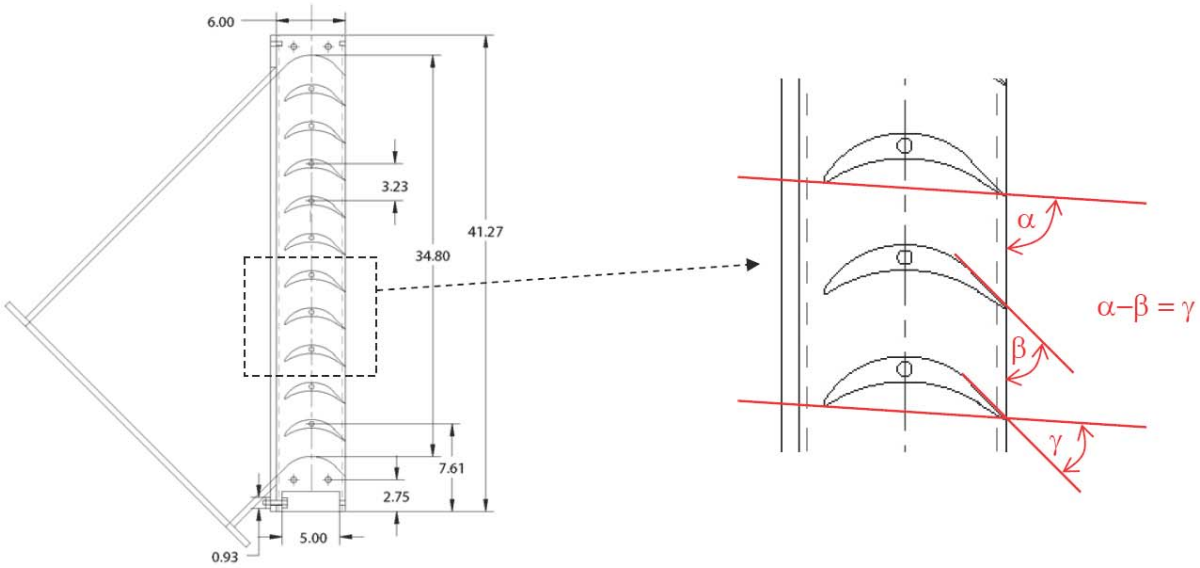

Figure 11. Experimentally verifiable (measurable) angles on the installed turning vanes, here illustrated on corner #1. Angle α was measured with a machinist's protractor.

Figure 12. Turning vane angles in corner No. 1: measuring angle α with a protractor (shown for design angle of attack, i.e., $\alpha = 84.9^{o}$). The square-to-round transition was removed for access.

3. Pressure measurements

3.1. Pressure measurement locations

Static pressure measurements were made to check the performance of the contraction and diffuser, and to document head losses around the flow circuit. During measurements of the LOCAT physical model a small gap just downstream of the fan was left open to the atmosphere. One can interpret the fan as simply providing a pressure jump to compensate for the losses around the flow circuit. Therefore the pressure immediately downstream of the fan is the highest pressure in the flow circuit. Since the gap forces the pressure at this point to be atmospheric, all other pressures in the tunnel will adjust themselves accordingly and the entire flow circuit will be sub-atmospheric.

A sufficiently large number of pressure taps was provided along the centerline of the inside walls of the contraction, test section, transition and diffuser. Upon request by the sponsor, additional pressure taps were added near the corners. The pressure in the corner can be significantly lower than at the centerline in parts such as the contraction, and corner measurements are needed to ensure that the performance of the prototype tunnel will not be limited by cavitation in the contraction. The corner pressure taps were placed at 2% of the total local width from the inside corner. For example, upstream of the contraction where the local model width is 850mm, the corner tap was positioned at 17mm from the inside corner, whereas in the test section, where the local model width is 467mm the corner tap was positioned at 9.3mm from the inside corner. When looking in the streamwise direction from the centerline of the tunnel in the test section leg, the corner taps are located in the bottom right corner. The pressure measurement locations are summarized in Table 3. More detail on tap locations in the contraction, test section, transition and diffuser is given in the tables in Figures 13 through 15.

3.2. Pressure measurement instrumentation

All pressure taps were drilled with a diameter of 0.79mm (1/32″), the smallest hole diameter deemed practical. Practical-size holes will result in a small measurement error because of flow in and around the hole opening. A hole size of 0.79mm causes an error of less than 1% of $1/2\rho U^2$ compared to an "ideal" hole (c.f. Blake 1983 [1]). The holes were drilled without burrs and so that the corners were "square", when viewed in a cut through the center of a hole.

Barbed brass fittings were installed with a 10-32 thread in the 1/2″ acrylic material, and in acrylic pieces epoxied to the 1/8″ steel before painting. 1/16″ I.D. (1/8″ O.D.) Superthane ether tubing (NewAge Industries, PA) was used to connect to eight 24-port Scanivalve W2 fluid switch wafers, for a total of 192 channels of pressure measurements.

Table 3. Pressure tap locations along physical model. Note that for rectangular cross-sections (from tap #0 to #169) even tap numbers are taps at the center, while odd tap numbers are taps in the corner – located at 2% of the total local height from the inside corner. Tap locations are given for model geometry.

model part	tap #	location	total taps
corner 4, before vanes	0,1	76mm from entrance to model	
corner 4, before vanes	2,3	486mm from entrance to model	
corner 4, after vanes	4,5	25mm from inside corner	
corner 4, after 1st HC	6,7	273mm from inside corner	
corner 4, after 2nd HC	8,9	565mm from inside corner	**10**
contraction	10–63	see separate table, Figure 13	**54**
test section	64–87	see separate table, Figure 14	**24**
transition	88–107	see separate table, Figure 14	**20**
diffuser	108–165	see separate table, Figure 15	**58**
corner 1, before vanes	166,167	64mm from entrance to corner	
corner 1, after vanes	168,169	64mm from exit of corner	**4**
square-to-round	179	51mm from entrance to SQ2R	
square-to-round	180	51mm from exit of SQ2R	**2**
corner 2, before vanes	170	64mm from entrance to corner	
corner 2, after vanes	171	22mm from exit of corner	**2**
straight pipe	172	76mm from entrance to pipe	
(pump inlet)	173	203mm from exit of pipe	
	174	16mm from exit of pipe	**3**
conical connector pipe	175	76mm from entrance to pipe	
	176	76mm from exit of pipe	**2**
fan	177	51mm from entrance to fan	
	178	638mm from entrance to fan	**2**
velocity static tap	181	235mm from test section entrance	
velocity stagnation tap	182	235mm from test section entrance	**2**
		total pressure measurements:	**183**

The collector port of each 24-port wafer was connected to a 12-port Scanivalve wafer, which was connected to a pressure transducer with a range of ten inches of water (approximately 2500 Pa). Thus eight 24-port Scanivalve wafers were effectively multiplexed into a single pressure transducer, eliminating any calibration ambiguity. The balance pressure applied to the Scanivalve cover should be above the measured pressures to form a pneumatic rotor thrust

bearing. Since it must not exceed the average measured pressure by 20 psi, atmospheric pressure was the logical choice for balance pressure. For calibration, six reference pressures (highest to lowest: atmospheric, tap #0, #8, #166, #136, #86,) could be switched into a micro-manometer with an accuracy of 0.001 inches of water (=0.25 Pa).

A VI (= "virtual instrument") written in LabVIEW was used to control the stepping of the scanivalve motors and to acquire data. Sensitivity tests were conducted for sample period and dead time between samples. For the data presented here each location was sampled for 5 seconds at 1000 samples per second, with a 2 second dead time between samples.

3.3 Pressure measurements, results and discussion

The bottom wall of the contraction is a fifth-order polynomial with an inflection point at x/L = 0.6. The pressure distribution along the centerline of the inside wall of the contraction and test section is shown in Figure 16. The measurement locations for each data set are normalized with the respective lengths of the contraction and test section, and a pressure coefficient was defined as

$$c_P = \frac{p - p_{TS}}{\frac{1}{2}\rho U_{TS}^2} \tag{5}$$

where p_{TS} is the reference static pressure measured at the entrance to the test section (tap #64), and U_{TS} is the mean streamwise reference velocity in the test section as measured with a pitot tube 50mm from the top wall. It can be seen that the pressure at x/L = 0.9 in the contraction is lower that at the contraction exit at x/L = 1.0. This pressure low would have been more severe had the inflection point occurred at x/L < 0.6. The lowest pressure along the centerline of the contraction is approximately equal to the lowest pressure along the centerline of the test section, which occurs at the test section exit. The test section pressure falls monotonously, a result of maintaining a constant cross-sectional area in the test section. As boundary layers grow along the wall, the flow in the center of the test section must speed up to satisfy continuity, thus resulting in a lower pressure at the wall. Note that the anomalous behavior of the second pressure tap from the exit of the contraction (tap #60) was traced to a small dent in the steel resulting from manufacturing.

The bottom wall of the transition between the test section and the diffuser is a third order polynomial. The pressure distribution along the centerline of the inside wall of the transition and diffuser is shown in Figure 17. Here the length L_{total} is the combined length of the transition (0.5m) and the diffuser (3.4m). As the flow enters the transition a dip in pressure occurs as a result of the change in curvature. Then the pressure rises monotonously throughout the diffuser, indicating that separation does not occur. However, the RMS value of the measured pressure increases towards the exit of the diffuser, indicating high turbulence levels in the boundary layer. Figures 18 and 19 show the comparison of inside wall centerline and corner pressures for the contraction and test section, and for the transition and diffuser, respectively. It can be seen that the corner pressures in the contraction are the ones that deviate most from the centerline pressures. The 10th corner tap from the exit of the contraction (tap #45) shows that there is some flow disturbance in the corner. Other possible causes for this sudden jump in pressure were carefully eliminated (hole re-drilled, sanded square with fine grain sandpaper, etc). As a check, the pressure measurements were repeated at different test section velocities; 10.5m/s (drive frequency 12Hz), 21m/s (24Hz), 31.5m/s (36Hz) and 52.5m/s (60Hz). The jump in pressure at corner tap #45 was found for all but the lowest velocity. Whether this flow disturbance is due to the model or the design can not be determined. Finally, Figure 20 shows the inside centerline wall pressure distribution along the entire model (dimensional data, length in meters, pressure in Pascal).

pressure taps in contraction: material 1/8" soft steel, pressure tap diameter 1/32"														
						(Note: corner taps are located 2% of total local width from inside corner)							where to drill before bending	
streamwise location			pressure tap	location		pressure tap	location		distance from corner		half-width		arc length of curve	
X[m]	X/L	X [in]	center	Y[m]	Y[in]	bott. corner	Y[m]	Y [in]	Yc[m]	Yc [in]	Yh[m]	Yh[in]	Lx[m]	Lx[in]
1.5	1	59.055	no			no	0.2240	8.819	0.0093	0.367	0.2333	9.186		
1.4875	0.992	58.563	1	0.000	0.000	1	0.2240	8.819	0.0093	0.367	0.2333	9.186	1.6139	63.539
1.4625	0.975	57.579	1	0.000	0.000	1	0.2240	8.820	0.0093	0.367	0.2334	9.187	1.5889	62.554
1.4375	0.958	56.594	1	0.000	0.000	1	0.2241	8.822	0.0093	0.368	0.2334	9.189	1.5639	61.570
1.4125	0.942	55.610	1	0.000	0.000	1	0.2242	8.827	0.0093	0.368	0.2335	9.195	1.5389	60.586
1.3875	0.925	54.626	1	0.000	0.000	1	0.2244	8.836	0.0094	0.368	0.2338	9.204	1.5139	59.601
1.3625	0.908	53.642	1	0.000	0.000	1	0.2248	8.849	0.0094	0.369	0.2341	9.218	1.4888	58.616
1.3375	0.892	52.657	1	0.000	0.000	1	0.2252	8.867	0.0094	0.369	0.2346	9.237	1.4638	57.630
1.3125	0.875	51.673	1	0.000	0.000	1	0.2259	8.892	0.0094	0.370	0.2353	9.262	1.4387	56.643
1.2875	0.858	50.689	1	0.000	0.000	1	0.2266	8.923	0.0094	0.372	0.2361	9.295	1.4136	55.655
1.2625	0.842	49.705	1	0.000	0.000	1	0.2276	8.961	0.0095	0.373	0.2371	9.334	1.3885	54.664
1.2375	0.825	48.720	1	0.000	0.000	1	0.2288	9.007	0.0095	0.375	0.2383	9.382	1.3632	53.670
1.2125	0.808	47.736	1	0.000	0.000	1	0.2301	9.060	0.0096	0.378	0.2397	9.438	1.3379	52.673
1.1625	0.775	45.768	1	0.000	0.000	1	0.2335	9.192	0.0097	0.383	0.2432	9.575	1.2869	50.665
1.1125	0.742	43.799	1	0.000	0.000	1	0.2377	9.359	0.0099	0.390	0.2476	9.749	1.2353	48.634
1.0500	0.700	41.339	1	0.000	0.000	1	0.2443	9.617	0.0102	0.401	0.2544	10.018	1.1698	46.055
0.9500	0.633	37.402	1	0.000	0.000	1	0.2576	10.141	0.0107	0.423	0.2683	10.564	1.0621	41.817
0.8500	0.567	33.465	1	0.000	0.000	1	0.2740	10.789	0.0114	0.450	0.2855	11.239	0.9507	37.428
0.7500	0.500	29.528	1	0.000	0.000	1	0.2930	11.535	0.0122	0.481	0.3052	12.016	0.8357	32.902
0.6500	0.433	25.591	1	0.000	0.000	1	0.3136	12.346	0.0131	0.514	0.3266	12.860	0.7183	28.280
0.6000	0.400	23.622	1	0.000	0.000	1	0.3242	12.762	0.0135	0.532	0.3377	13.294	0.6592	25.951
0.5500	0.367	21.654	1	0.000	0.000	1	0.3347	13.178	0.0139	0.549	0.3487	13.727	0.6000	23.622
0.4500	0.300	17.717	1	0.000	0.000	1	0.3553	13.987	0.0148	0.583	0.3701	14.570	0.4826	19.002
0.3500	0.233	13.780	1	0.000	0.000	1	0.3740	14.724	0.0156	0.613	0.3896	15.337	0.3681	14.490
0.2500	0.167	9.843	1	0.000	0.000	1	0.3896	15.340	0.0162	0.639	0.4059	15.979	0.2576	10.142
0.1500	0.100	5.906	1	0.000	0.000	1	0.4011	15.790	0.0167	0.658	0.4178	16.448	0.1519	5.979
0.0500	0.033	1.969	1	0.000	0.000	1	0.4072	16.031	0.0170	0.668	0.4242	16.699	0.0501	1.972
0.0250	0.017	0.984	1	0.000	0.000	1	0.4078	16.055	0.0170	0.669	0.4248	16.724	0.0250	0.985
0.0	0	0	no			no	0.4080	16.063	0.0170	0.669	0.4250	16.732		
# of taps			27	center		27	corner							
X: streamwise coordinate from contraction entrance, Y: position as measured from centerline, Yc: position as measured from corner, Lx: length of flat piece before bending														

Figure 13. Pressure tap locations in the contraction of the LOCAT physical model.

pressure taps in test section: material 1/2" acrylic, pressure tap diameter 1/32", 10-32 thread

						(Note: corner taps are located 2% of total local width from inside corner)						
streamwise location			pressure tap	location		pressure tap	location		distance from corner		half-width	
X[m]	X/L	**X [in]**	center	Y[m]	**Y[in]**	bott. corner	Y[m]	**Y [in]**	Yc[m]	**Yc [in]**	Yh[m]	**Yh[in]**
0	0	0.000	no			no						
0.0254	0.012	**1.000**	1	0.000	**0.000**	1	0.2240	**8.819**	0.0093	**0.367**	0.2333	**9.186**
0.0381	0.018	**1.500**	1	0.000	**0.000**	1	0.2240	**8.819**	0.0093	**0.367**	0.2333	**9.186**
0.0508	0.024	**2.000**	1	0.000	**0.000**	1	0.2240	**8.819**	0.0093	**0.367**	0.2333	**9.186**
0.1016	0.049	**4.000**	1	0.000	**0.000**	1	0.2240	**8.819**	0.0093	**0.367**	0.2333	**9.186**
0.2032	0.098	**8.000**	1	0.000	**0.000**	1	0.2240	**8.819**	0.0093	**0.367**	0.2333	**9.186**
0.3048	0.146	**12.000**	1	0.000	**0.000**	1	0.2240	**8.819**	0.0093	**0.367**	0.2333	**9.186**
0.6096	0.293	**24.000**	1	0.000	**0.000**	1	0.2240	**8.819**	0.0093	**0.367**	0.2333	**9.186**
0.9144	0.439	**36.000**	1	0.000	**0.000**	1	0.2240	**8.819**	0.0093	**0.367**	0.2333	**9.186**
1.2192	0.585	**48.000**	1	0.000	**0.000**	1	0.2240	**8.819**	0.0093	**0.367**	0.2333	**9.186**
1.5240	0.732	**60.000**	1	0.000	**0.000**	1	0.2240	**8.819**	0.0093	**0.367**	0.2333	**9.186**
1.8288	0.878	**72.000**	1	0.000	**0.000**	1	0.2240	**8.819**	0.0093	**0.367**	0.2333	**9.186**
2.0322	0.976	**80.008**	1	0.000	**0.000**	1	0.2240	**8.819**	0.0093	**0.367**	0.2333	**9.186**
2.0830	1.000	82.008	no	0	0	no	0.2240	**8.819**	0.0093	**0.367**	0.2333	**9.186**
# of taps			**12**	**center**		**12**	**corner**					

X: streamwise coordinate from test section entrance, Y: position as measured from centerline, Yc: position as measured from corner

pressure taps in transition from T.S. to diffuser: material 1/8" soft steel, pressure tap diameter 1/32"

						(Note: corner taps are located 2% of total local width from inside corner)							where to drill before bending	
streamwise location			pressure tap	location		pressure tap	location		distance from corner		half-width		arc length of curve	
X[m]	X/L	**X [in]**	center	Y[m]	**Y[in]**	bott. corner	Y[m]	**Y [in]**	Yc[m]	**Yc [in]**	Yh[m]	**Yh[in]**	Lx[m]	**Lx[in]**
0	0.00		no			no					0.2333			
0.0254	0.05	**1.000**	1	0.000	**0.000**	1	0.2240	**8.820**	0.0093	**0.368**	0.2334	**9.188**	0.0254	**1.000**
0.0762	0.15	**3.000**	1	0.000	**0.000**	1	0.2243	**8.831**	0.0093	**0.368**	0.2336	**9.199**	0.0762	**3.001**
0.1270	0.25	**5.000**	1	0.000	**0.000**	1	0.2248	**8.851**	0.0094	**0.369**	0.2342	**9.219**	0.1271	**5.002**
0.1778	0.36	**7.000**	1	0.000	**0.000**	1	0.2255	**8.878**	0.0094	**0.370**	0.2349	**9.248**	0.1779	**7.005**
0.2286	0.46	**9.000**	1	0.000	**0.000**	1	0.2264	**8.912**	0.0094	**0.371**	0.2358	**9.283**	0.2289	**9.010**
0.2794	0.56	**11.000**	1	0.000	**0.000**	1	0.2273	**8.950**	0.0095	**0.373**	0.2368	**9.323**	0.2798	**11.016**
0.3302	0.66	**13.000**	1	0.000	**0.000**	1	0.2284	**8.991**	0.0095	**0.375**	0.2379	**9.366**	0.3308	**13.024**
0.3810	0.76	**15.000**	1	0.000	**0.000**	1	0.2295	**9.034**	0.0096	**0.376**	0.2390	**9.411**	0.3818	**15.032**
0.4318	0.86	**17.000**	1	0.000	**0.000**	1	0.2306	**9.078**	0.0096	**0.378**	0.2402	**9.456**	0.4328	**17.040**
0.4750	0.95	**18.700**	1	0.000	**0.000**	1	0.2315	**9.114**	0.0096	**0.380**	0.2411	**9.494**	0.4762	**18.747**
0.5000	0		no	0	0	no	0.2320	9.134	0.0097	0.381	0.2417	9.514		
# of taps			**10**	**center**		**10**	**corner**							

X: streamwise coordinate from contraction entrance, Y: position as measured from centerline, Yc: position as measured from corner, Lx: length of flat piece before bending

Figure 14. Pressure tap locations in the test section and transition of the LOCAT physical model.

pressure taps in main diffuser: material 1/2" acrylic, pressure tap diameter 1/32", 10-32 thread														
						(Note: corner taps are located 2% of total local width from inside corner)							where to drill on flat sheet	
streamwise location			pressure tap	location		pressure tap	location		distance from corner		half-width		of 4.9 degree diffuser	
X[m]	X/L	**X [in]**	center	Y[m]	**Y[in]**	bott. corner	Y[m]	**Y [in]**	Yc[m]	**Yc [in]**	Yh[m]	**Yh[in]**	Lx[m]	**Lx[in]**
0	0		no			no					0.2417			
0.0508	0.015	**2.000**	1	0.000	**0.000**	1	0.2330	**9.174**	0.0097	**0.382**	0.2427	**9.556**	0.0510	**2.007**
0.1016	0.030	**4.000**	1	0.000	**0.000**	1	0.2340	**9.214**	0.0098	**0.384**	0.2438	**9.598**	0.1020	**4.015**
0.2032	0.060	**8.000**	1	0.000	**0.000**	1	0.2361	**9.294**	0.0098	**0.387**	0.2459	**9.681**	0.2039	**8.029**
0.3048	0.090	**12.000**	1	0.000	**0.000**	1	0.2381	**9.374**	0.0099	**0.391**	0.2480	**9.764**	0.3059	**12.044**
0.4064	0.120	**16.000**	1	0.000	**0.000**	1	0.2401	**9.454**	0.0100	**0.394**	0.2501	**9.848**	0.4079	**16.059**
0.5080	0.149	**20.000**	1	0.000	**0.000**	1	0.2422	**9.534**	0.0101	**0.397**	0.2523	**9.931**	0.5099	**20.073**
0.6350	0.187	**25.000**	1	0.000	**0.000**	1	0.2447	**9.634**	0.0102	**0.401**	0.2549	**10.035**	0.6373	**25.092**
0.7620	0.224	**30.000**	1	0.000	**0.000**	1	0.2472	**9.734**	0.0103	**0.406**	0.2575	**10.139**	0.7648	**30.110**
0.8890	0.261	**35.000**	1	0.000	**0.000**	1	0.2498	**9.834**	0.0104	**0.410**	0.2602	**10.244**	0.8923	**35.128**
1.0160	0.299	**40.000**	1	0.000	**0.000**	1	0.2523	**9.934**	0.0105	**0.414**	0.2628	**10.348**	1.0197	**40.147**
1.1430	0.336	**45.000**	1	0.000	**0.000**	1	0.2549	**10.034**	0.0106	**0.418**	0.2655	**10.452**	1.1472	**45.165**
1.2700	0.374	**50.000**	1	0.000	**0.000**	1	0.2574	**10.134**	0.0107	**0.422**	0.2681	**10.556**	1.2747	**50.183**
1.3970	0.411	**55.000**	1	0.000	**0.000**	1	0.2599	**10.234**	0.0108	**0.426**	0.2708	**10.660**	1.4021	**55.202**
1.5240	0.448	**60.000**	1	0.000	**0.000**	1	0.2625	**10.334**	0.0109	**0.431**	0.2734	**10.764**	1.5296	**60.220**
1.6510	0.486	**65.000**	1	0.000	**0.000**	1	0.2650	**10.434**	0.0110	**0.435**	0.2761	**10.869**	1.6571	**65.238**
1.7000	0.500	66.929	no	0	0	no	0.2660	10.472	0.0111	0.436	0.2771	10.909	1.7062	67.175
1.700	0.500	66.929	no			no	0.2660	10.472	0.0111	0.436	0.2771	10.909	1.7062	67.175
1.7780	0.523	**70.000**	1	0.000	**0.000**	1	0.2676	**10.534**	0.0111	**0.439**	0.2787	**10.973**	1.7845	**70.257**
1.9050	0.560	**75.000**	1	0.000	**0.000**	1	0.2701	**10.634**	0.0113	**0.443**	0.2814	**11.077**	1.9120	**75.275**
2.0320	0.598	**80.000**	1	0.000	**0.000**	1	0.2726	**10.734**	0.0114	**0.447**	0.2840	**11.181**	2.0395	**80.293**
2.1590	0.635	**85.000**	1	0.000	**0.000**	1	0.2752	**10.834**	0.0115	**0.451**	0.2866	**11.285**	2.1669	**85.312**
2.2860	0.672	**90.000**	1	0.000	**0.000**	1	0.2777	**10.934**	0.0116	**0.456**	0.2893	**11.389**	2.2944	**90.330**
2.4130	0.710	**95.000**	1	0.000	**0.000**	1	0.2803	**11.034**	0.0117	**0.460**	0.2919	**11.494**	2.4219	**95.348**
2.5400	0.747	**100.000**	1	0.000	**0.000**	1	0.2828	**11.134**	0.0118	**0.464**	0.2946	**11.598**	2.5493	**100.367**
2.6670	0.784	**105.000**	1	0.000	**0.000**	1	0.2853	**11.234**	0.0119	**0.468**	0.2972	**11.702**	2.6768	**105.385**
2.7940	0.822	**110.000**	1	0.000	**0.000**	1	0.2879	**11.334**	0.0120	**0.472**	0.2999	**11.806**	2.8042	**110.403**
2.9210	0.859	**115.000**	1	0.000	**0.000**	1	0.2904	**11.434**	0.0121	**0.476**	0.3025	**11.910**	2.9317	**115.422**
3.0480	0.896	**120.000**	1	0.000	**0.000**	1	0.2930	**11.534**	0.0122	**0.481**	0.3052	**12.014**	3.0592	**120.440**
3.1750	0.934	**125.000**	1	0.000	**0.000**	1	0.2955	**11.634**	0.0123	**0.485**	0.3078	**12.119**	3.1866	**125.459**
3.3020	0.971	**130.000**	1	0.000	**0.000**	1	0.2980	**11.734**	0.0124	**0.489**	0.3105	**12.223**	3.3141	**130.477**
3.3528	0.986	**132.000**	1	0.000	**0.000**	1	0.2991	**11.774**	0.0125	**0.491**	0.3115	**12.264**	3.3651	**132.484**
3.4000	1.000		no	0	0	no	0.3000	11.811	0.0125	0.492	0.3125	12.303	3.4125	134.349
# of taps			**29**	**center**		**29**	**corner**						1/cos(4.9deg)=	**1.0037**
X: streamwise coordinate from contraction entrance, Y: position as measured from centerline, Yc: position as measured from corner, Lx: length of flat piece before bending														

Figure 15. Pressure tap locations in the diffuser of the LOCAT physical model.

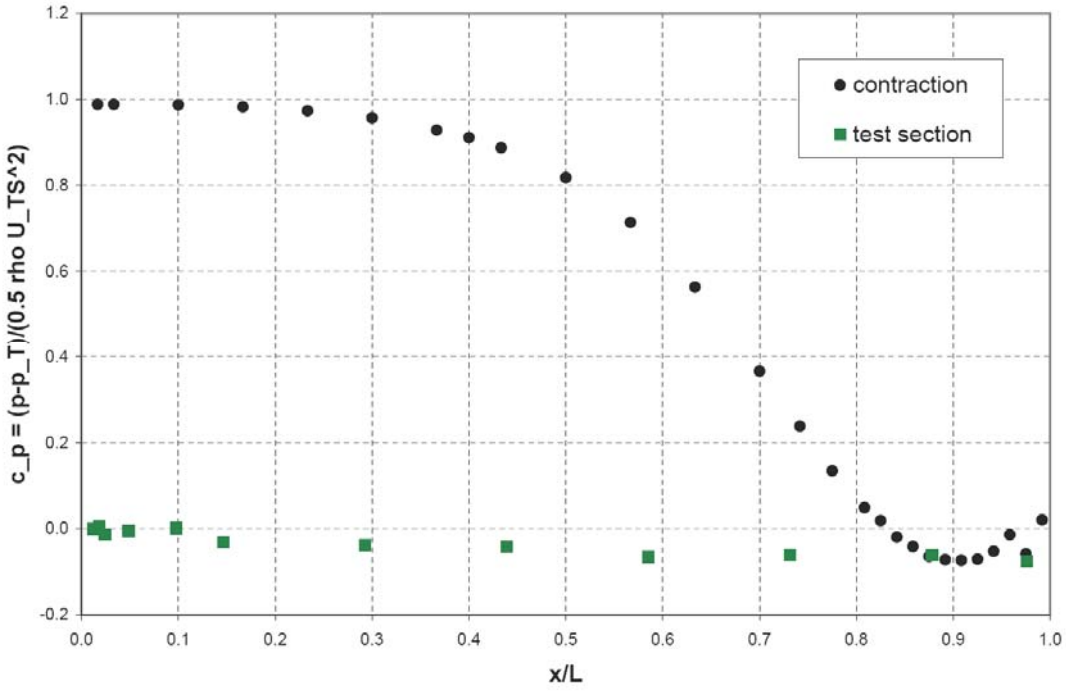

Figure 16. Pressure distribution in contraction and test section, inside centerline.

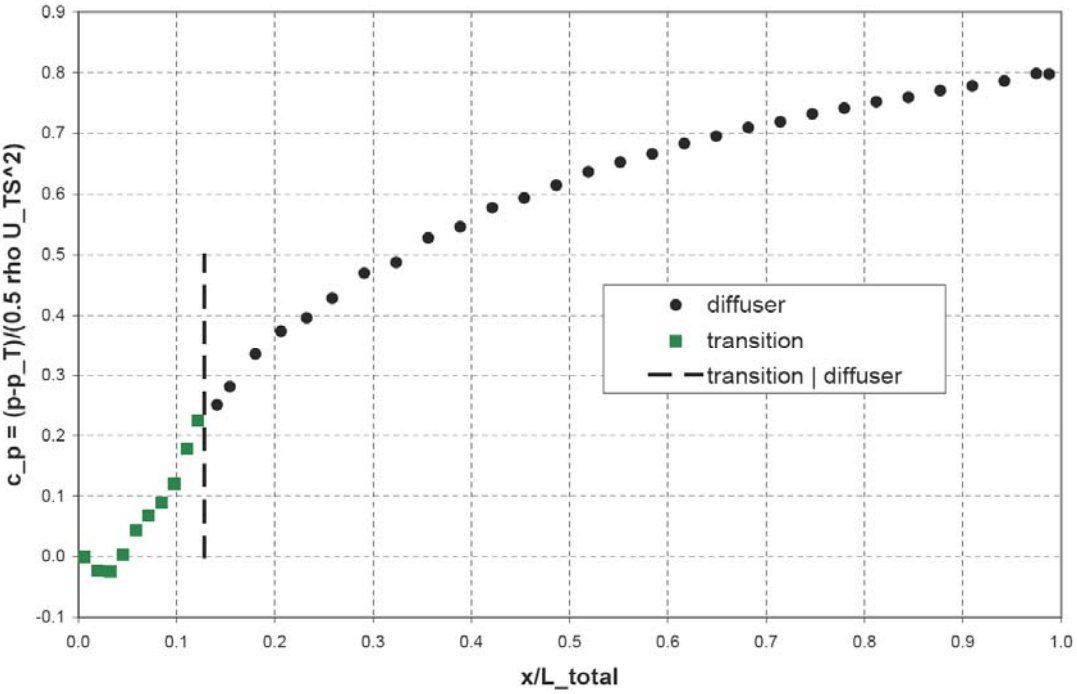

Figure 17. Pressure distribution in transition and diffuser, inside centerline.

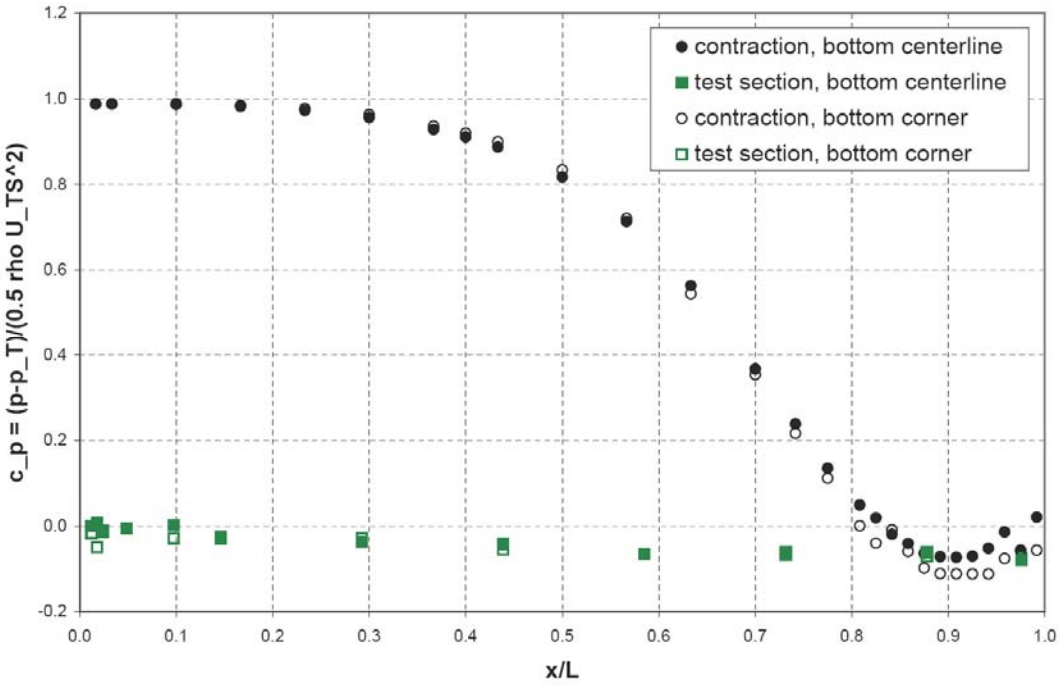

Figure 18. Pressure distribution in Contraction and test section, comparison of inside centerline (centerplane) and corner pressures (measured at 0.02 H(x)).

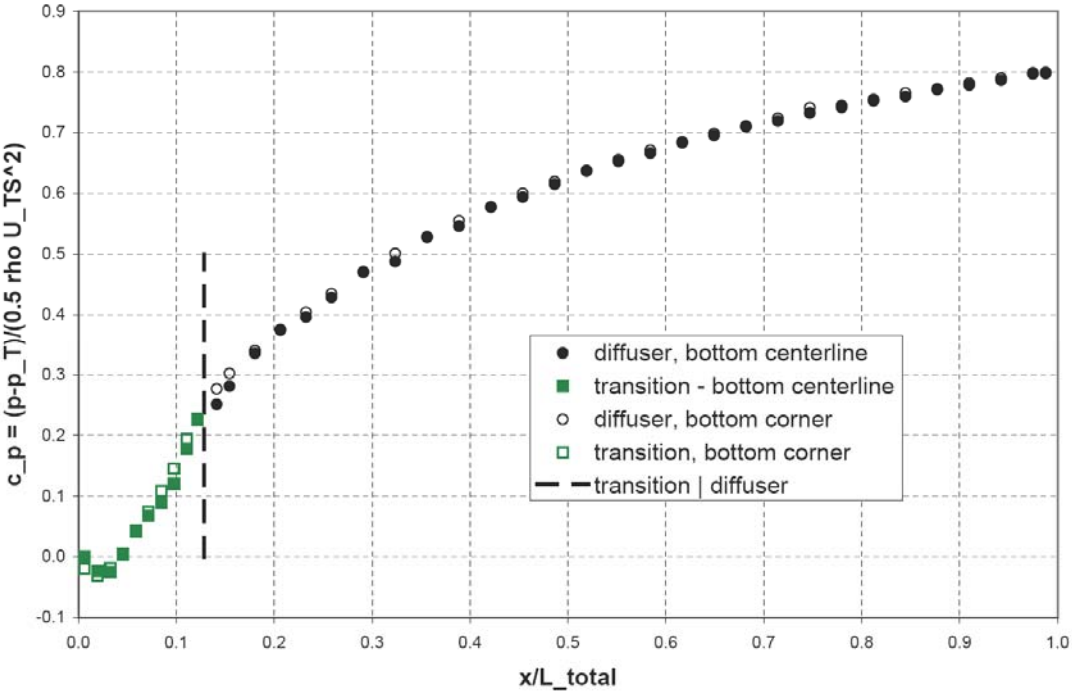

Figure 19. Pressure distribution in transition and diffuser, comparison of inside centerline (centerplane) and corner pressures (measured at 0.02 H(x)).

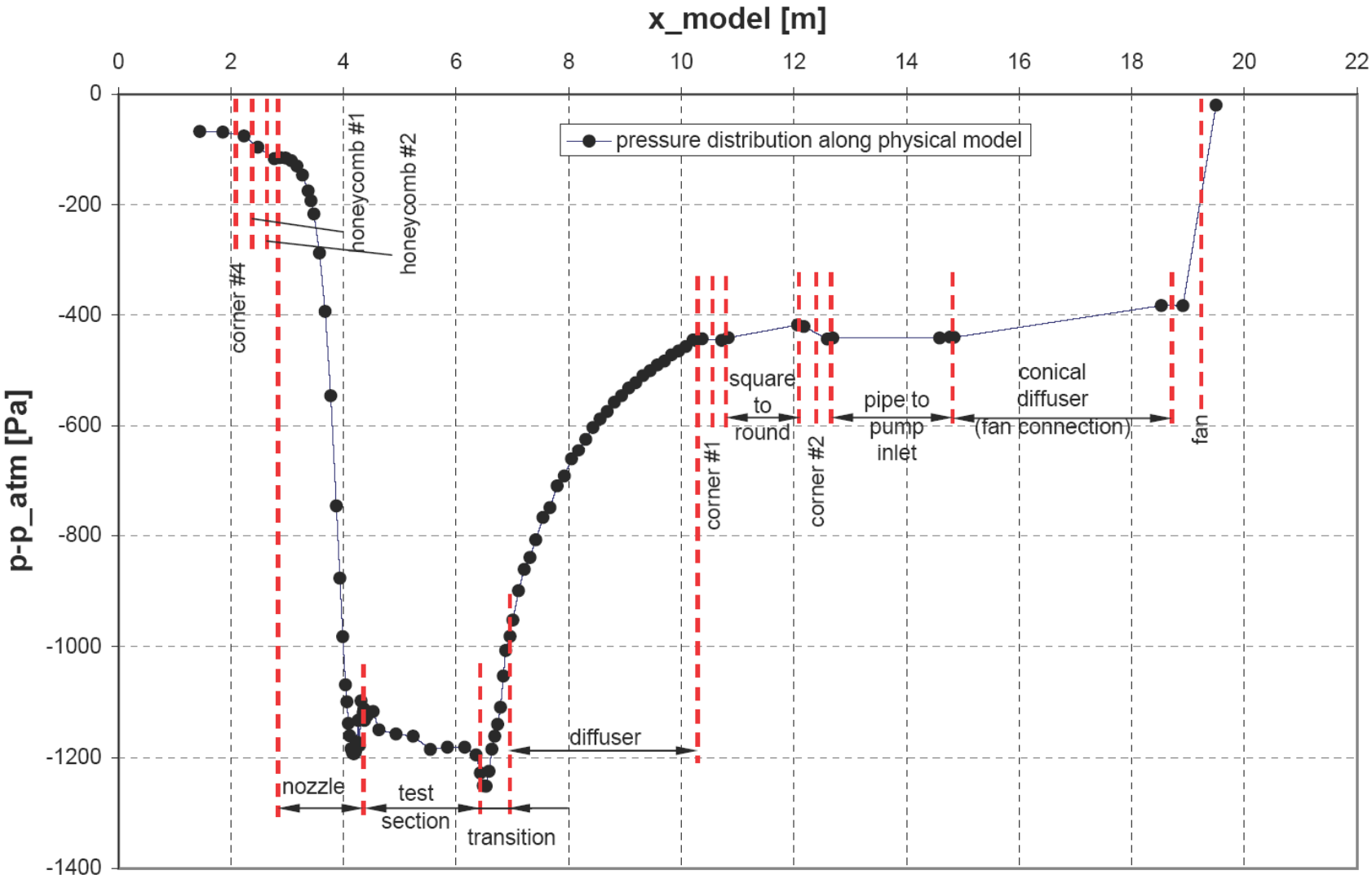

Figure 20. LOCAT physical model: Inside centerline wall pressure distribution along the entire model.

4. Velocity measurements

Pitot tubes, hot wire anemometry (HWA), particle image velocimetry (PIV) and laser Doppler velocimetry (LDV) all were candidates as techniques to measure flow velocities in the LOCAT physical model. The sponsor requested that a non-intrusive optical technique be used. As it was not possible to obtain cross-sectional profiles with PIV at most locations (where it would have been possible, e.g., in the test section, it would have been necessary to use Stereo-PIV with the streamwise direction being the 3rd velocity component associated with the highest uncertainty), it was decided to use LDV for both mean velocity and turbulence measurements.

Velocity profiles were obtained using a dual-beam 2-component Laser Doppler Velocimeter (LDV) manufactured by TSI. The LDV system consisted of: a water-cooled 5W Ar-Ion multi-line laser, beam-splitting optics with an acousto-optical cell for frequency shifting and fiber-optic couplers, a fiber-optic probe with 4 emitting fibers and one receiving fiber, electronics for processing the Doppler burst frequency spectra and electronic frequency shifting, and a personal computer with software for controlling the LDV electronics, traversing, data acquisition and processing. The fiber-optic probe is attached to a 10m long fiber-optic cable, which allows all LDV components to be stationary except for the fiber-optic probe. As seeding particles both glycol-based droplets obtained via condensation in a commercial fog machine and olive oil droplets created in a custom-built Laskin nozzle via atomization by pressurized air were extensively tested, with the Laskin nozzle giving somewhat better results in terms of monodispersity of droplets, droplet size ($\approx 1\mu m$) and obtainable LDV data rates.

In measurement positions with small cross section, such as the test section, the standard 350mm (363mm) lens for the fiber-optic probe could be used. However, in most locations a lens with 500mm (512mm) focal length had to be employed. As the signal-to-noise ratio *SNR* drops as the inverse square of the focal length of the length, f_l: $SNR \propto (A/f_l)^2$ (with A = const.), the longer focal length reduces the signal-to-noise ratio by about a factor of two. This affected mostly the *V*-component (blue beams, 488nm, cross-stream), since the blue beams have lower power than the green beams (streamwise, 514.5nm, *U*) at the higher laser power settings required for measurements in air. LDV parameters and seeding were adjusted for optimum performance, however, the maximum data rate of "good" data points was thus much lower for the *V*-

component than for the *U*-component. Typically 10,000 data samples were acquired per measurement point with the LDV in "random mode", meaning either a *U*-data point or *V*-data point could register. The fiber-optic probe would traverse to the next measurement point when the total of data samples from both *U* and *V* reached 10,000 or when a specified timeout of 60 seconds was reached. In certain near-wall locations much fewer than 10,000 valid data points could be obtained in 60 seconds due to noise from beam reflection.

At each measurement position with a rectangular cross section, a 2-axis traversing system was set up to traverse in both cross-stream directions *y* and *z*. At the circular cross-sections fixed angular positions were spaced 30 degrees apart and a 1-axis traversing system was set up for the radial direction *r*. The traversing slides used were Velmex Bi-Slides, with 2mm/revolution screws. Velmex drives perform half-steps on a 200 magnet pair stepper motor, resulting in 400 steps per revolution, or a 5 μm/step accuracy. The traversing steps in all the runs reported here were chosen to be small enough, typically 5mm, to be able to capture the wakes downstream of the turning vanes.[3] The streamwise LDV measurement locations are shown in Figure 21.

4.1. Uncertainty analysis

Note that the analysis below addresses *only* the uncertainty of a random variable with Gaussian distribution based on number of samples and standard deviation. It does not attempt to correct the bias introduced, e.g., by imperfections or scratches in the acrylic windows. This bias could be considerable, given the fact the polycast acrylic windows could have some waviness and variation in thickness and would scratch easily.

For an LDV measurement of the streamwise velocity component in a turbulent flow at a given location,

$$\tilde{u} = U + u; \qquad \text{with: } \overline{u} = 0 \tag{6}$$

where $\tilde{u}$ is the instantaneous velocity, *U* is the mean velocity and *u* is the fluctuating velocity. The square root of the variance of the n-th moment, ε_n^2, is an estimate of the uncertainty of the n-the moment of a random variable *x*, i.e.

[3] In other runs, not reported here, traversing steps were varied between 40 mm and 1 mm.

$$\epsilon_n = \left[\left\langle (\overline{x^n} - \langle x^n \rangle)^2 \right\rangle\right]^{1/2} \tag{7}$$

and the relative uncertainty can be written as

$$\frac{\delta\overline{x^n}}{\overline{x^n}} \approx \frac{\epsilon_n}{\overline{x^n}} \tag{8}$$

Assuming the experimental moments behave like Gaussian moments, i.e., $\varepsilon_1^2 = \sigma^2/N$, $\varepsilon_2^2 = 2\sigma^4/N$, $\varepsilon_3^2 = 15\sigma^6/N$, etc., the uncertainty for the mean velocity and for the turbulence intensity are

$$\delta U \sim \epsilon_1 = \sqrt{\frac{\sigma^2}{N}} \qquad \text{and} \qquad \delta\overline{u^2} \sim \epsilon_2 = \sqrt{\frac{2\sigma^4}{N}} \quad , \tag{9}$$

respectively. With $\sigma^2 \approx u_{rms}^2$ the relative uncertainty for the mean velocity and for the turbulence intensity can be written as

$$\frac{\delta U}{U} \sim \frac{u_{rms}/U}{\sqrt{N}} \qquad \text{and} \qquad \frac{\delta\overline{u^2}}{\overline{u^2}} \sim \sqrt{\frac{2}{N}} \quad , \tag{10}$$

respectively. For example, in a section of the LOCAT model where the turbulence intensity is 10%, 1000 valid samples would result in uncertainties of $\delta U/U \approx 0.32\%$ and $\overline{\delta u^2} / \overline{u^2} \approx 4.5\%$, whereas 5000 valid samples would result in uncertainties of $\delta U/U \approx 0.14\%$ and $\overline{\delta u^2} / \overline{u^2} \approx 2.0\%$. In the measurement series reported here, the "typical" uncertainty from random error for the mean streamwise velocity, *U*, is better than 0.2%, and for streamwise turbulence intensity, *U/U*, it is better than 2%.

4.2. Coordinate system for rectangular cross-sections

The coordinate convention used for all the figures presented for rectangular cross sections is shown in Figure 22, where a location in the test section was used as an example to explain terms and orientation. Figure 22 shows a cut through the test section in prototype orientation, looking downstream. Downstream is always the *x*-direction. The origin for each local coordinate system

is in the plane of symmetry on the inside wall, with y as wall-normal coordinate and z as transverse coordinate so that they from a right-hand system with x. In rectangular cross-sections, velocity profiles were measured in the plane of symmetry, $z/W = 0$, and at quarter width, $z/W = 0.25$. “Inside” and “outside” are local references with respect to the rest of the flow loop.

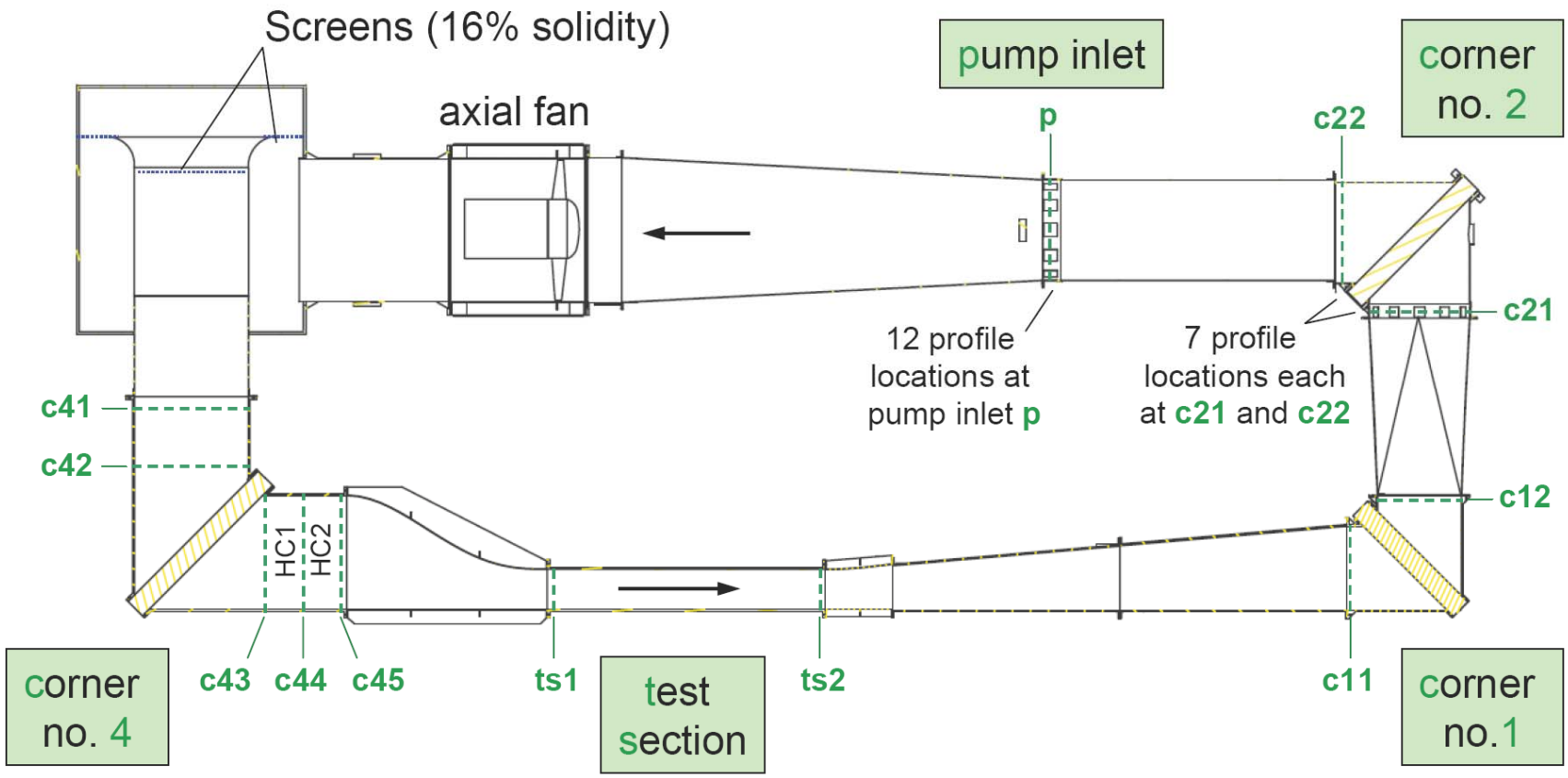

Figure 21. LOCAT physical model LDV measurement locations (shown in model layout).

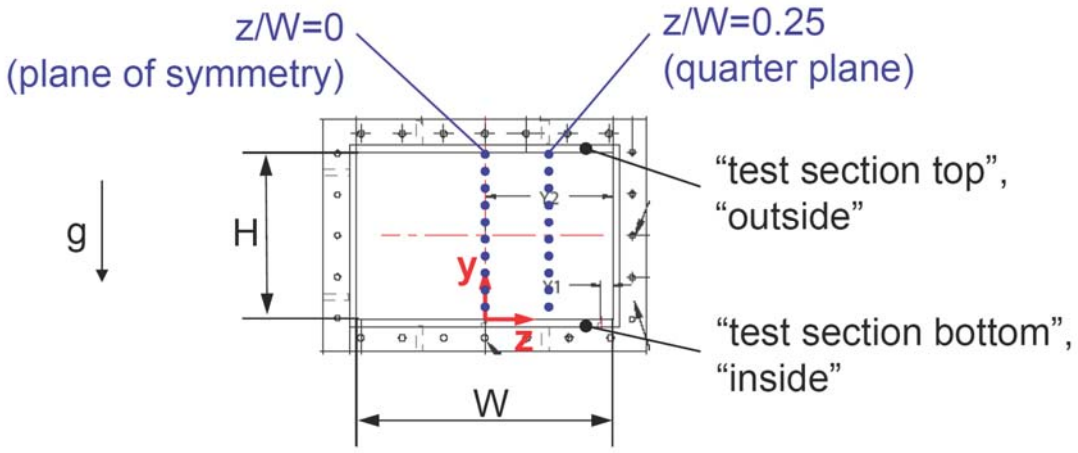

Figure 22. Coordinate system for plots in rectangular cross sections. Cut through test section, looking downstream (*x*-direction), in prototype orientation.

4.3. Corner No. 4

Corner #4 is located upstream of the contraction, and contains the turbulence management section with two honeycomb inserts. Velocity measurements were taken at five locations in corner #4, two upstream of the turning vanes, one downstream of the turning vanes before honeycomb #1 (HC1), one after honeycomb #1 and before honeycomb #2 (HC2), and one downstream of honeycomb #2 before the contraction. Traversing sliders were installed under the model so that the locations of the velocity profiles would coincide with the locations of the pressure taps, see Table 3.

The honeycombs were not scaled 1:6 as the rest of the model, since that would have led to a cell size small enough to have caused laminar flow in the cell (Reynolds number based on cell size less than 2000). Instead both the 20mm cell size HC1 and the 10mm cell size HC2 were modeled with 1/4″ (6.4mm) cell size honeycombs (this translates to a 1:3.2 model scale for HC1, and a 1:1.6 model for HC2). The model honeycombs were still chosen to be 20 cell sizes deep, and the arrangement as tested is shown in Figure 23. 1/8″ (3.2mm) thick spacers were fabricated and installed, so that the honeycomb arrangement can be changed somewhat for future tests.

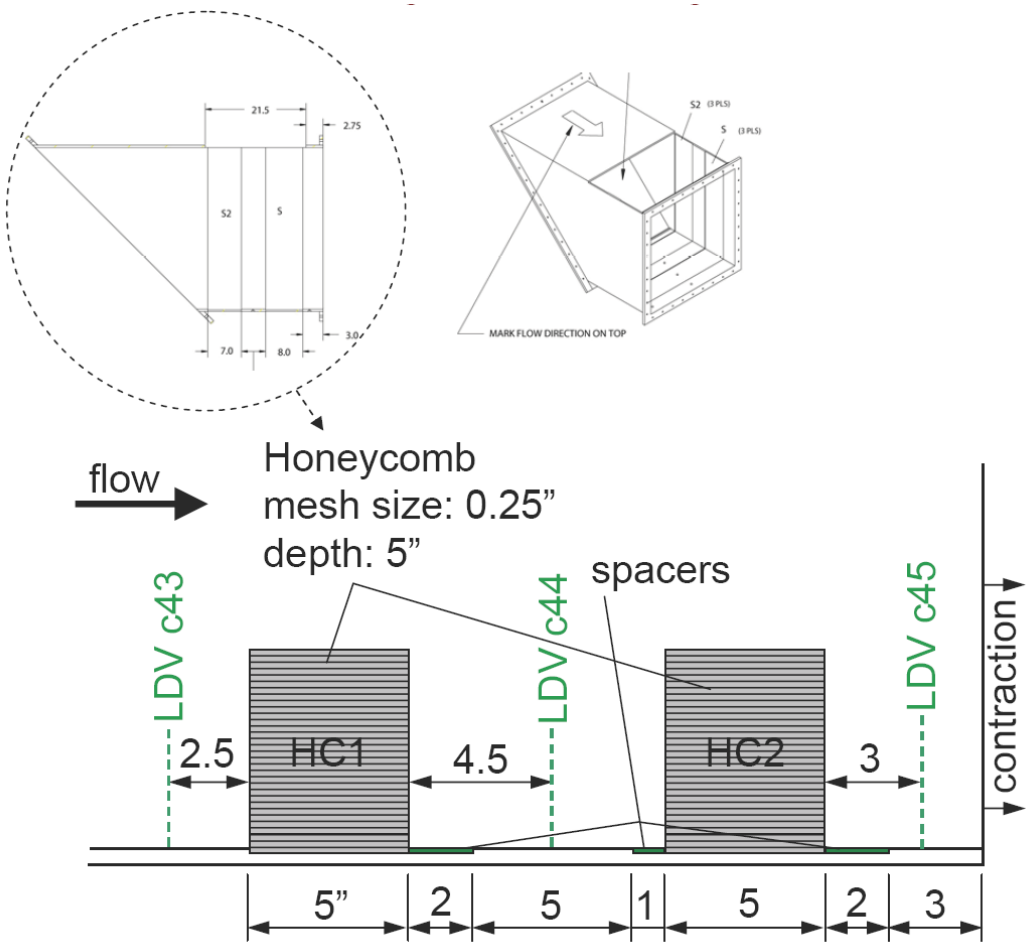

Figure 23. LOCAT physical model honeycomb arrangement and LDV measurement locations. All dimensions in inches.

The streamwise mean velocity and turbulence intensity in the tunnel plane of symmetry at corner #4, position 1, are shown in Figure 24. It can be seen the flow is highly turbulent due to recirculating the flow from the fan through 16% solidity screens, which was necessary to contain seeding for the optical flow measurements.

The streamwise mean velocity and turbulence intensity in the tunnel plane of symmetry at corner #4, position 2, just before the turning vanes, are shown in Figure 25. It was concluded that both mean velocity and turbulence intensity were sufficiently uniform to test the performance of the turning vanes and the turbulence management system.

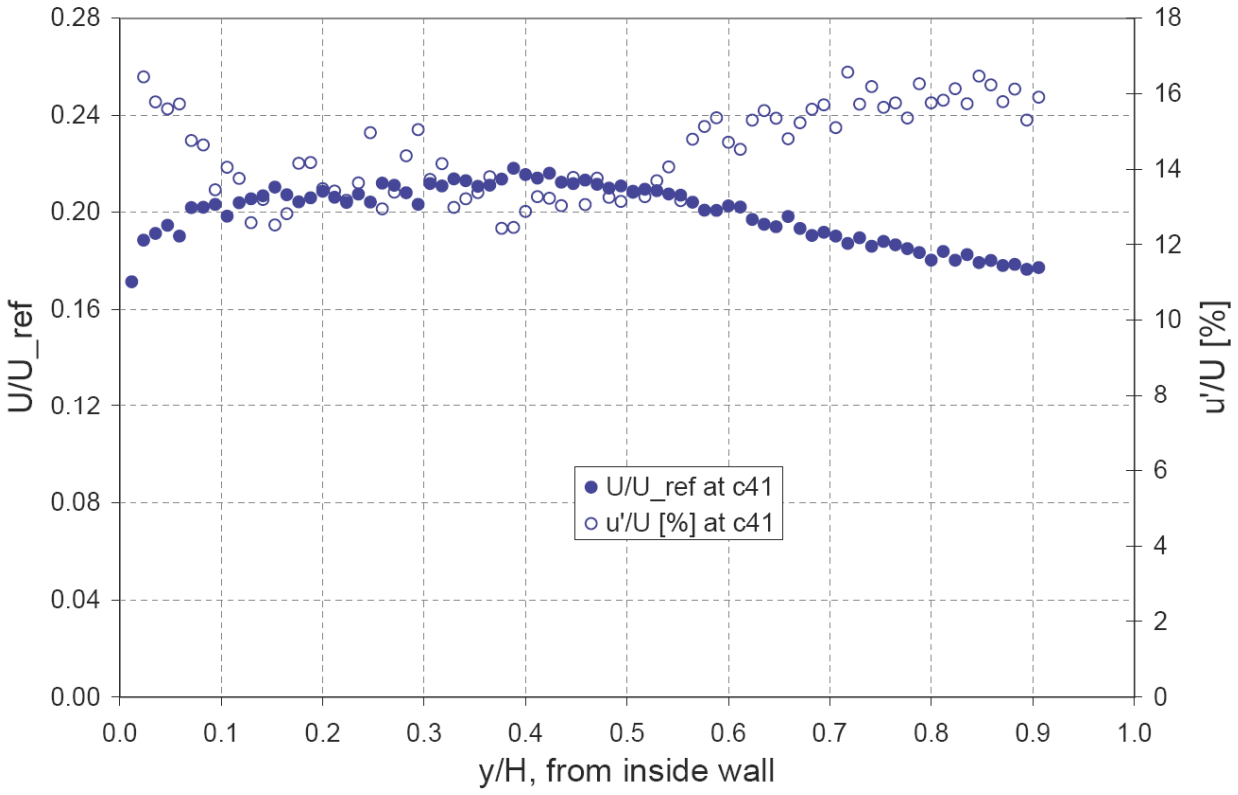

Figure 24. Streamwise mean velocity and turbulence intensity in the tunnel plane of symmetry at corner #4, position 1.

The streamwise mean velocity and turbulence intensity in the tunnel plane of symmetry at corner #4, position 3, just after the turning vanes and before honeycomb #1, are shown in Figure 26. With a 5mm spacing of measurement locations, the imprint of the turning vanes can clearly be seen on both the mean velocity and the turbulence profiles. The wake of the turning vanes, resulting in lower local velocity and higher local turbulence, can be seen more clearly on the inside, as the flow has traveled less distance from the vanes and had less space to recover. On the outside of the flow, the turning vane wakes have almost entirely disappeared, as the flow has had more distance to recover. Note how the turbulence intensity – aside from a few local maxima on the left resulting from velocity deficits in the near wake of the turning vanes – drops almost linearly from inside to outside, proportional to how much distance the flow has traveled after the turning vanes. Also note that due to space constraints under the model, measurements could not be taken very close to the wall both on the inside and outside.

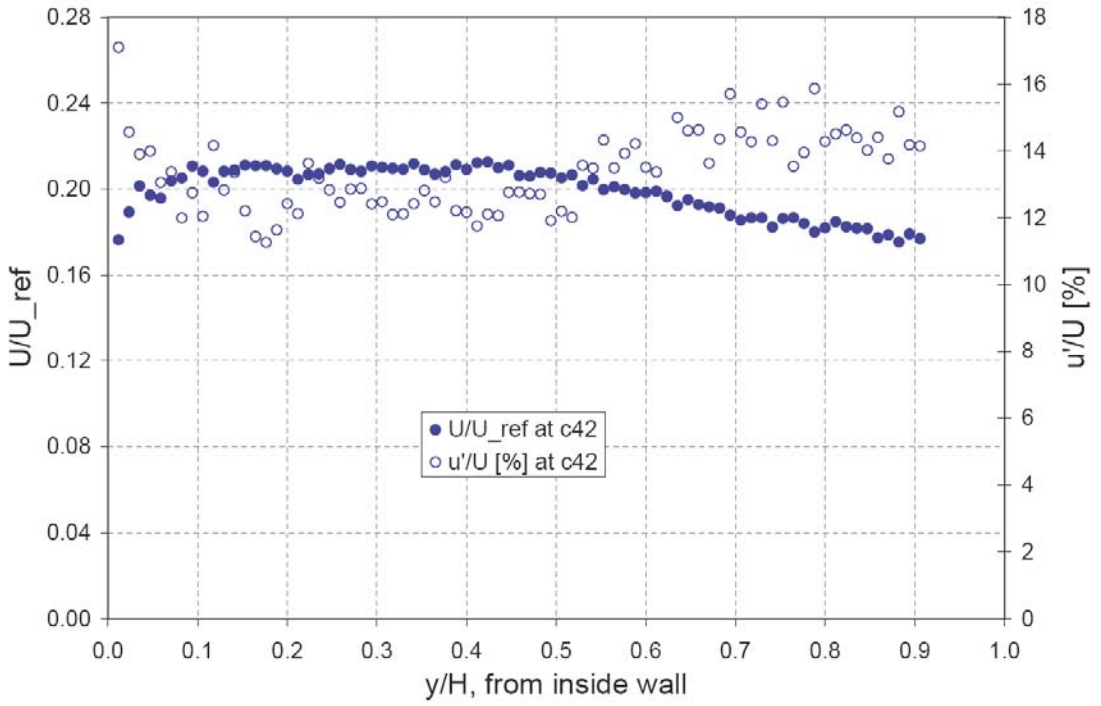

Figure 25. Streamwise mean velocity and turbulence intensity in the tunnel plane of symmetry at corner #4, position 2.

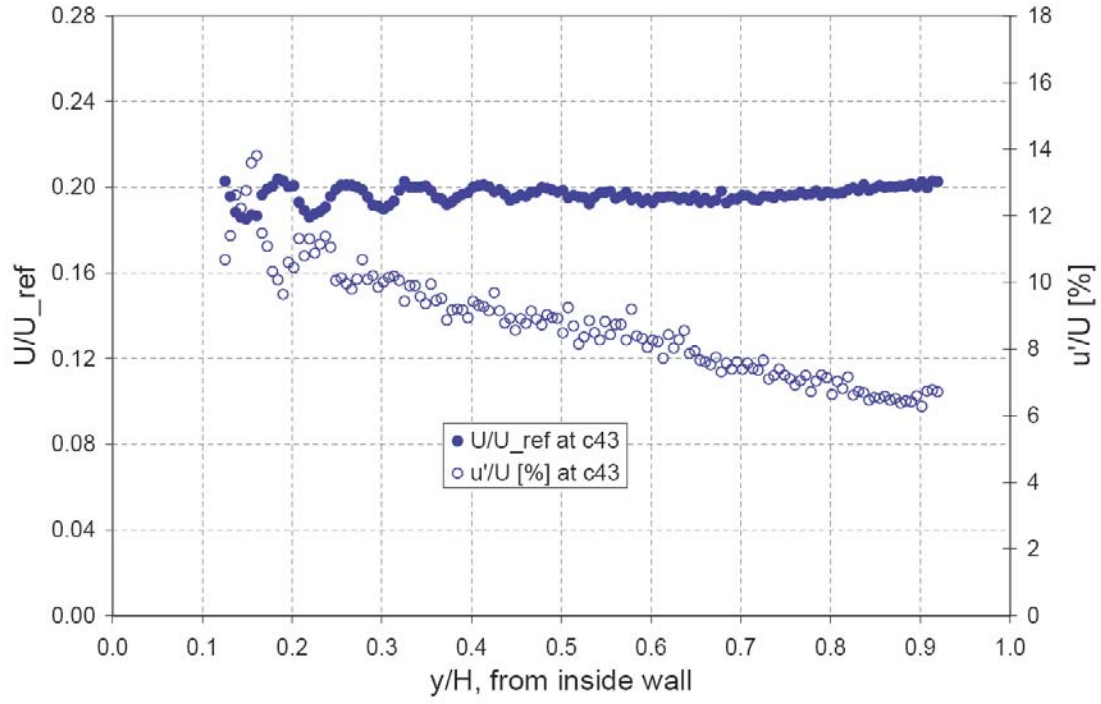

Figure 26. Streamwise mean velocity and turbulence intensity in the tunnel plane of symmetry at corner #4, position 3, 64 mm before honeycomb #1.

The streamwise mean velocity and turbulence intensity in the tunnel plane of symmetry at corner #4, position 4, after honeycomb #1 and before honeycomb #2, are shown in Figure 27. It is observed that the imprints of the turning vanes (wakes) remain remarkably intact through the honeycomb. It can also be observed that, as it passes through the honeycomb, the flow seems to lose more energy where the turbulence levels were higher before the honeycomb. Note that at this position measurements could be taken very close to the wall on the inside.

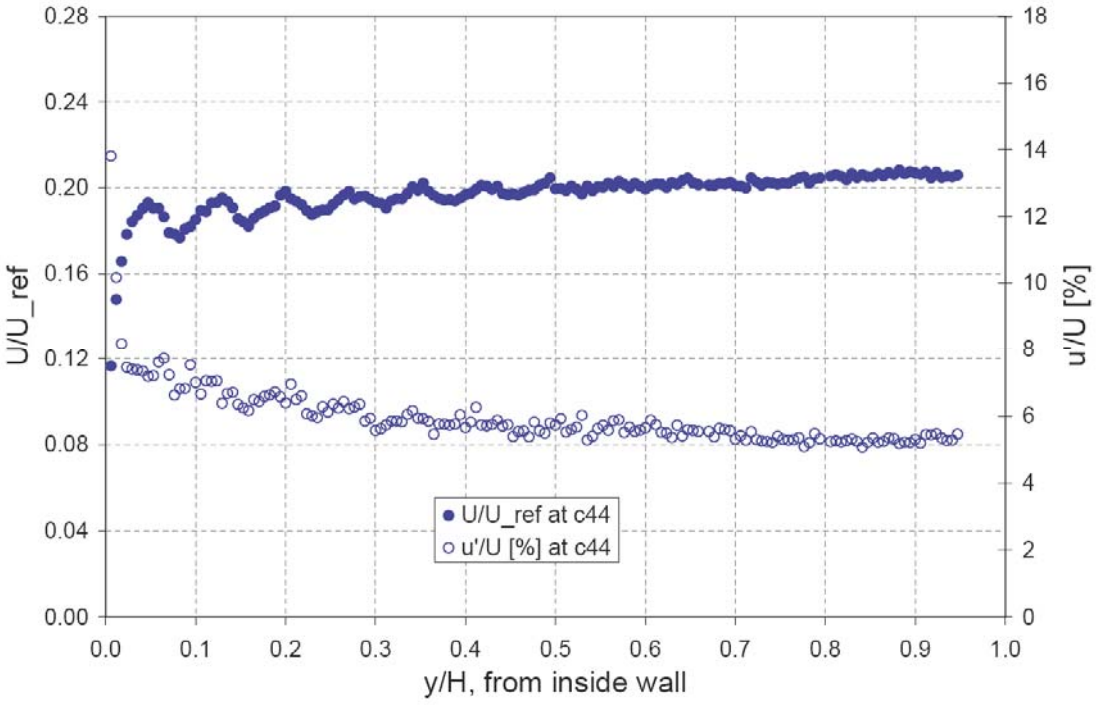

Figure 27. Streamwise mean velocity and turbulence intensity in plane of symmetry at corner #4, position 4, 115mm after honeycomb #1, 89mm before honeycomb #2.

The streamwise mean velocity and turbulence intensity in the tunnel plane of symmetry at corner #4, position 5, after honeycomb #2 and before the contraction are shown in Figure 28. Even after the second honeycomb, an imprint of the turning vanes can still be seen on the inside. As this measurement location is only 12 cell sizes downstream of the honeycomb, the mean velocity profile is not very smooth, and the turbulence levels are about as high as after honeycomb #1 (profile c44 was measured 18 cell sizes downstream of honeycomb #1). Again, as passes through the honeycomb the flow seems to lose more energy on the inside, where the turbulence levels were higher before the honeycomb.

To summarize what happens to the mean velocity profile as it passes through corner #4 and the turbulence management section, the streamwise mean velocity in the tunnel plane of symmetry at all 5 positions are shown in Figure 29. The scale has been enlarged to accentuate the differences between the profiles. It can clearly be seen that the wakes of the turning vanes persist through both honeycombs, and that the flow loses energy on the inside, where turbulence levels are higher after the turning vanes, as it goes through the honeycombs.

Figure 30 shows LDV measurements in progress at corner #4, position 5. In the view from the inside (on the right) pressure taps #8 and #9 can also be seen. Five inches, or 20 honeycomb cell sizes after honeycomb #2 the flow enters the contraction (or nozzle).

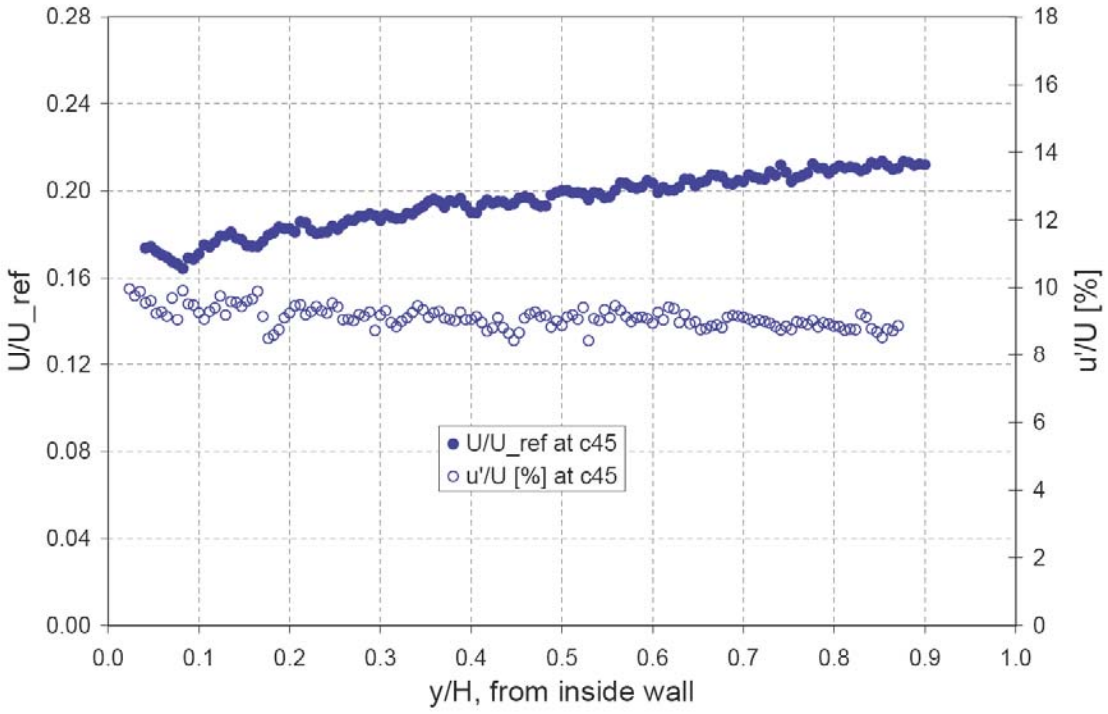

Figure 28. Streamwise mean velocity and turbulence intensity in the tunnel plane of symmetry at corner #4, position 5, 76mm after honeycomb #2, 51mm before the contraction.

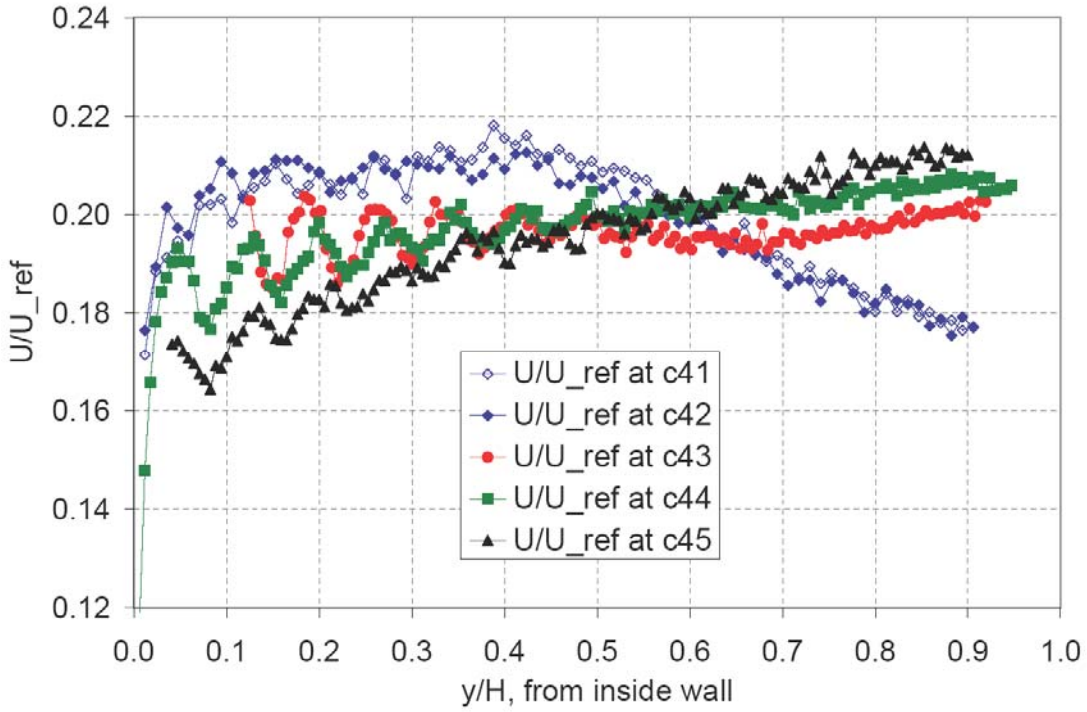

Figure 29. Streamwise mean velocity in the tunnel plane of symmetry at corner #4, at all 5 positions.

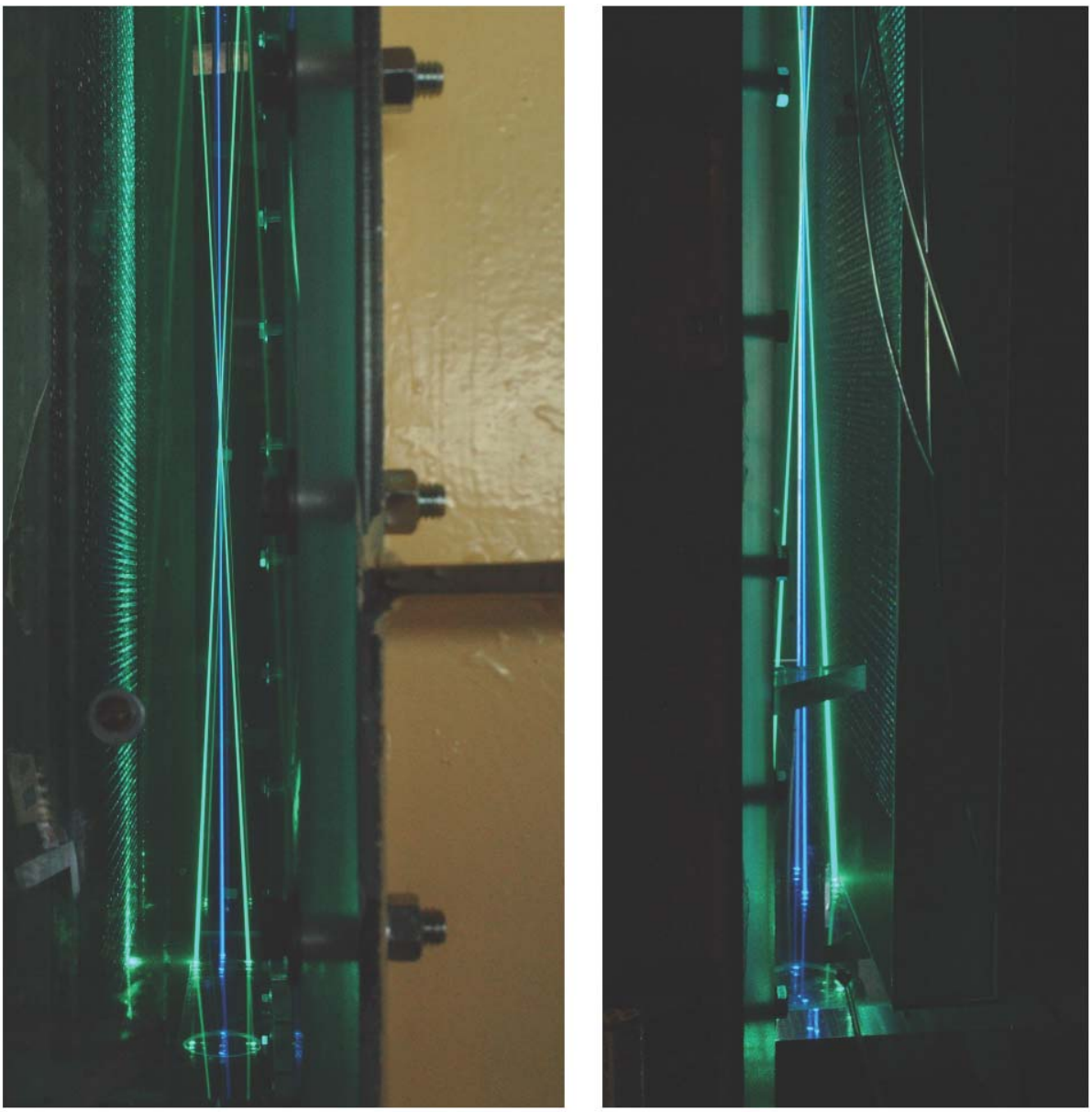

Figure 30. LDV measurement at corner #4, position 5. Left: view from the 'outside' (flow is left to right), Right: view from the 'inside' (flow is right to left) of the flow circuit.

4.4. Test section

The contraction is described by one fifth order polynomial on the bottom and another fifth order polynomial on the two sides, and reduces the flow cross-sectional area at a ratio of 5.16:1. It has a flat top so that the test section is at the highest point in the flow circuit in order to have the lowest hydrostatic pressure. The test section of the LOCAT physical model had constant cross-

sectional area with a model width of 467mm and a model height of 300mm. Figure 31 shows the streamwise (U) and cross-stream (V) mean velocity, and streamwise turbulence intensity at the test section inlet in the tunnel plane of symmetry (51mm from inlet). The flow is reasonably uniform with negligible cross-stream component, however, it can be seen that the mean streamwise velocity U varies 2.7% from $0.05 < y/H < 0.95$. This is significantly more than the design goal of 1%. The turbulence level is near 1% through most of the test section. These issues can be attributed to the turbulence management section not functioning properly with its insufficient overall length for the larger-than-model-scale honeycombs and the short distance after the second honeycomb before it enters the contraction, c.f. Figure 23. In contrast to upstream of the contraction, c.f. Figure 28, the flow is now faster on the inside. One possible cause for this could be strong corner vortices in the contraction, as supported by the disturbance in corner pressure observed in Figure 18. Another observation is that the boundary layers are quite thick. This is one hand attributable to having low Reynolds number, but could also again be the result of not having enough distance after the second honeycomb: Honeycomb-near wall disturbances are propagated into the contraction before they were able to decay sufficiently.

Figure 32 shows streamwise (U) and cross-stream (V) mean velocity, and streamwise turbulence intensity at the test section exit in the tunnel plane of symmetry. The boundary layers in this low-Reynolds number physical model have now grown to over 10% of the test section width, which is also reflected in the turbulence intensity near the walls. The flow at the center of the test section has sped up somewhat to compensate for the area constriction due to the growth of the boundary layers on the walls.

Figure 33 shows LDV measurements in progress at the entrance of the test section, here the LDV is traversing at quarter width z/W=0.25.

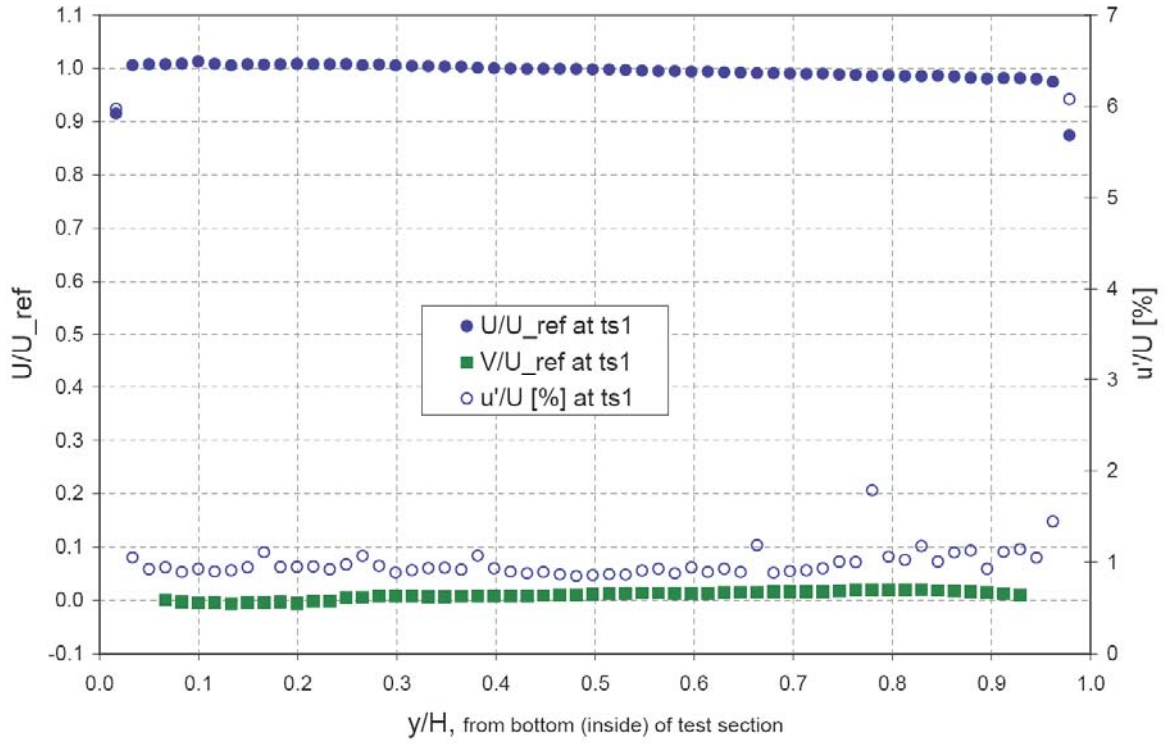

Figure 31. Streamwise (*U*) and cross-stream (*V*) mean velocity, and streamwise turbulence intensity at the test section inlet in the tunnel plane of symmetry.

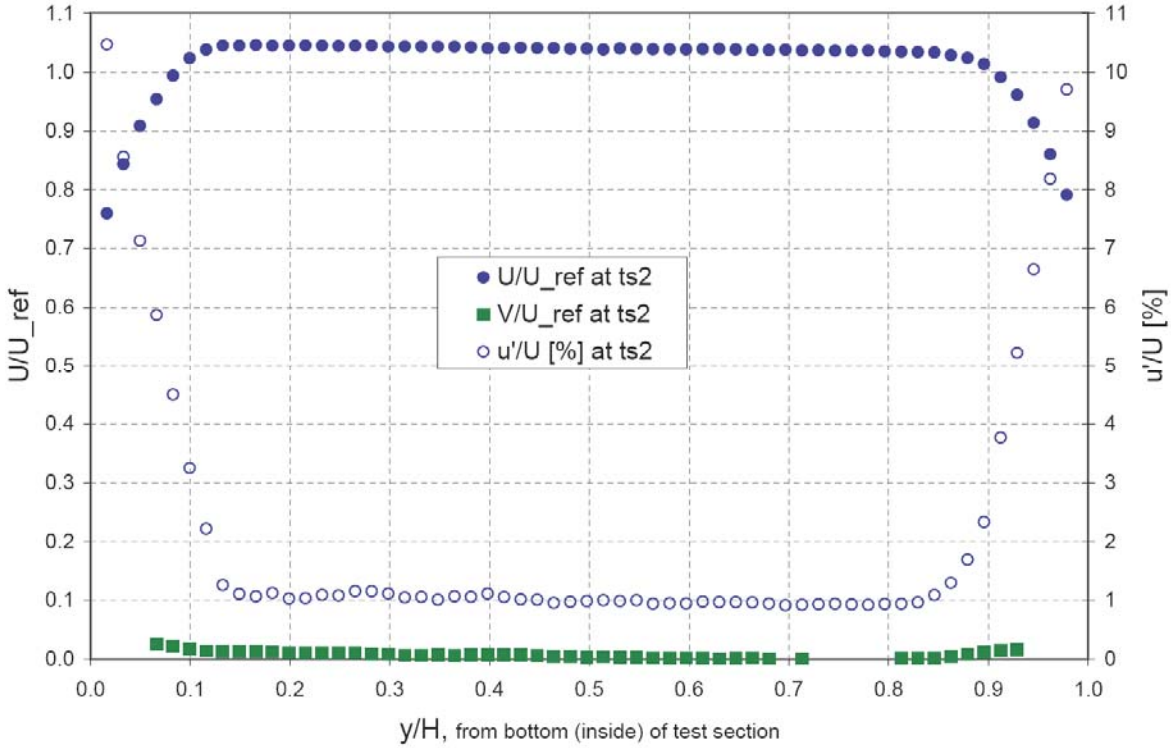

Figure 32. Streamwise (*U*) and cross-stream (*V*) mean velocity, and streamwise turbulence intensity at the test section exit in the tunnel plane of symmetry.

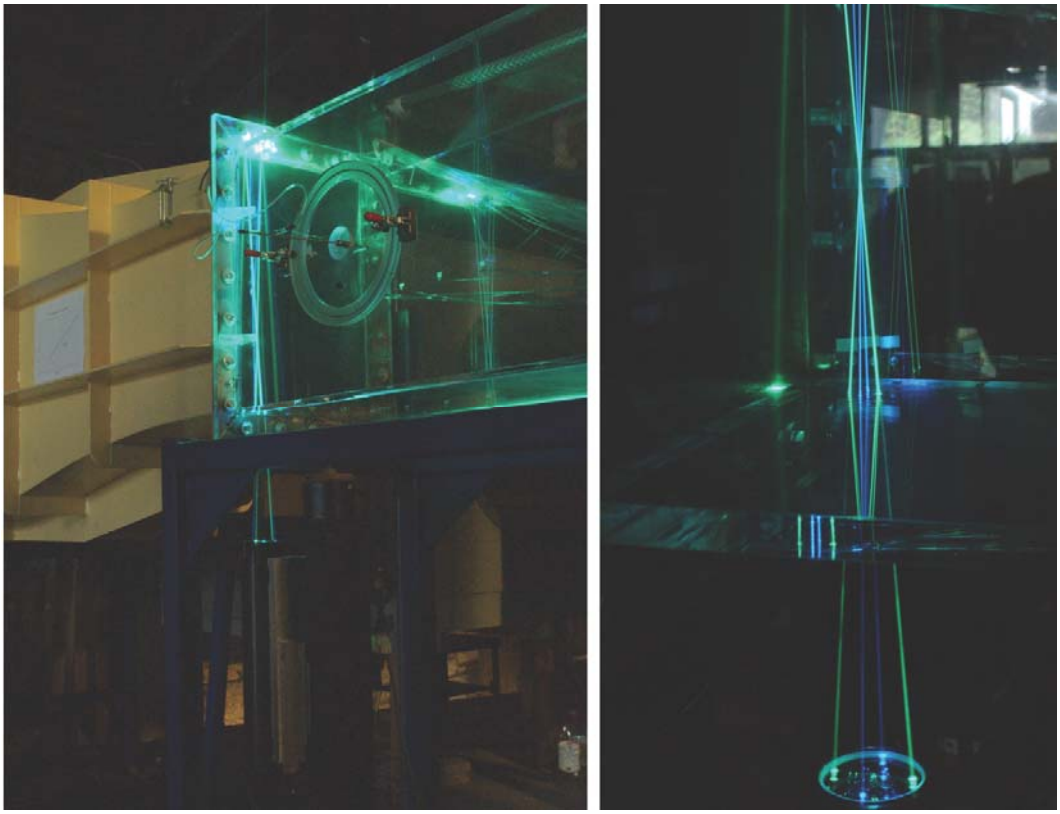

Figure 33. LDV measurement at the test section entrance. Flow is left to right.

4.5. Corner No. 1

After the test section, the flow goes through a short transition leading to an asymmetric diffuser. The diffuser bottom angle is 4.9 degrees, the side angles are 1.2 degrees. As for the entire upper leg, its top wall is horizontal. Corner #1 is located downstream of the diffuser, has 10 turning vanes and leads into the square-to-round transition. Figure 34 shows the streamwise mean velocity (U), and streamwise turbulence intensity at corner #1, position 1, just after the exit of the diffuser and before the turning vanes. From the mean velocity profile it can be seen that the flow is not separated. The boundary layers are large, and there is only a small portion of the velocity profile in the center that is still flat. The mean velocity profile is slightly asymmetric. The turbulence intensity near the inside wall is quite high, which is in agreement with the high RMS wall pressures seen towards the end of the diffuser.

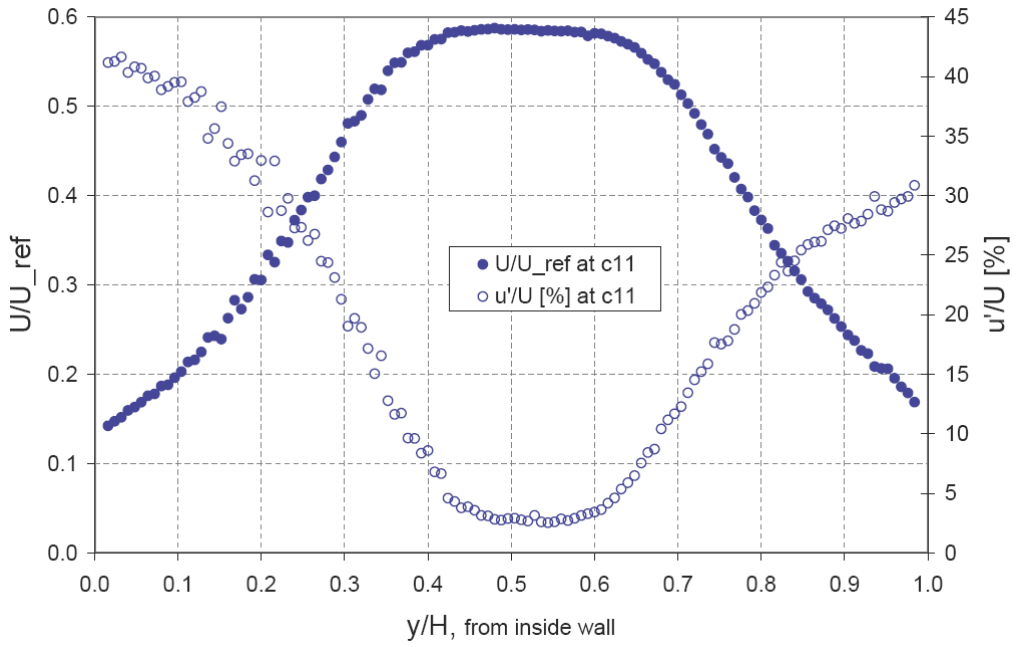

Figure 34. Streamwise mean velocity (*U*) and streamwise turbulence intensity at corner #1, position 1.

Figure 35 shows the streamwise mean velocity (*U*), and streamwise turbulence intensity at corner #1, position 2, after the turning vanes, just before entering the square-to-round transition. The wakes of the turning vanes, which are set to +2 degrees (in an aerodynamic sense) off design angle of attack, can clearly be seen in the velocity profiles. The mean velocity profile is slightly skewed towards the outside, which could be a result of the slight asymmetry observed at position 1 before the turning vanes, and/or an under-turning of the flow by the turning vanes. Even more of an asymmetry is observed in the turbulence intensity as the flow enters the square to round-transition.

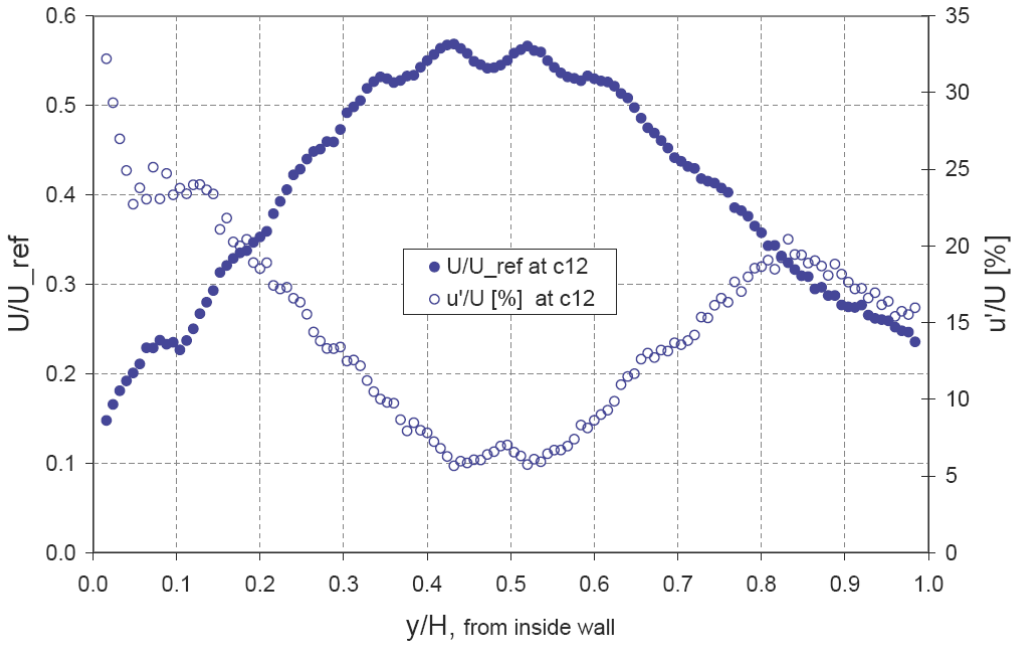

Figure 35. Streamwise mean velocity (*U*) and streamwise turbulence intensity at corner #1, position 2.

Figure 36. LDV measurements in corner #1, after turning vanes in plane of symmetry, $z/W = 0$.

4.6. Corner No. 2

Corner No. 2 is situated after the square-to-round transition. The inlet and outlet are circular, while the 45-degree miter line of the turning vane box describes an elliptical shape. The turning vane assembly houses 12 vanes. Measurement windows (made from 1/8 inch acrylic, recessed into the 1/8 inch steel using a collar) were provided at 7 locations each at the inlet and the outlet of corner No. 2 and spaced 30 degrees apart, thus covering a 180 degree semi-circle on the left side of the plane of symmetry. Semi-circular positioning plates for the LDV traversing slide were mounted on a frame on the outside of the model tunnel, and were aligned with the axis of the tunnel using a bearing-supported shaft and a micrometer. Shims were used to make the plates flat to within 0.025". First, velocity profiles in the tunnel plane of symmetry at corner #2, position 1, before the turning vanes, are presented. Figure 37 shows the positions of LDV traverses p01 and p07, and Figure 38 shows the data from these traverses, acquired from both sides with some overlap at the center. The mean velocity profile is still skewed towards the outside, and the flow is much more turbulent on the inside, which could be a result of the high turbulence intensity observed on the inside wall of the asymmetric diffuser. There is a negligible cross-stream component of mean velocity.

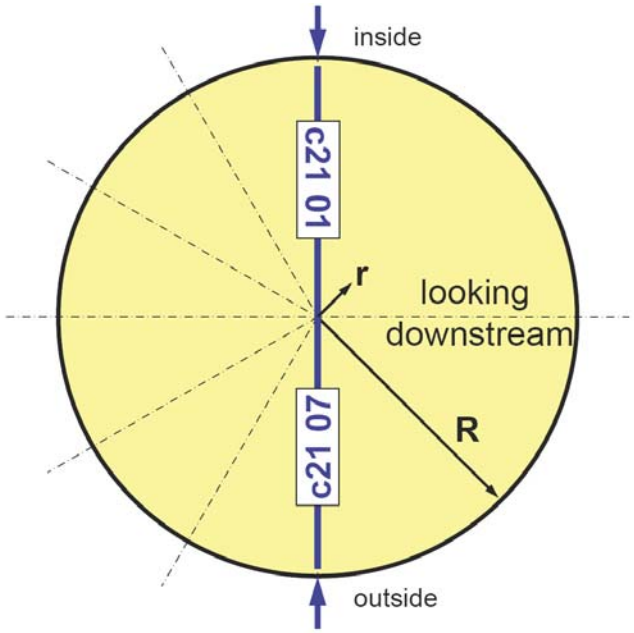

Figure 37. LDV velocity profile measurement positions in the tunnel plane of symmetry at corner #2, position 1, in prototype orientation looking downstream. *U* is positive in streamwise direction, $V_{azimuthal}$ is positive in the clockwise direction.

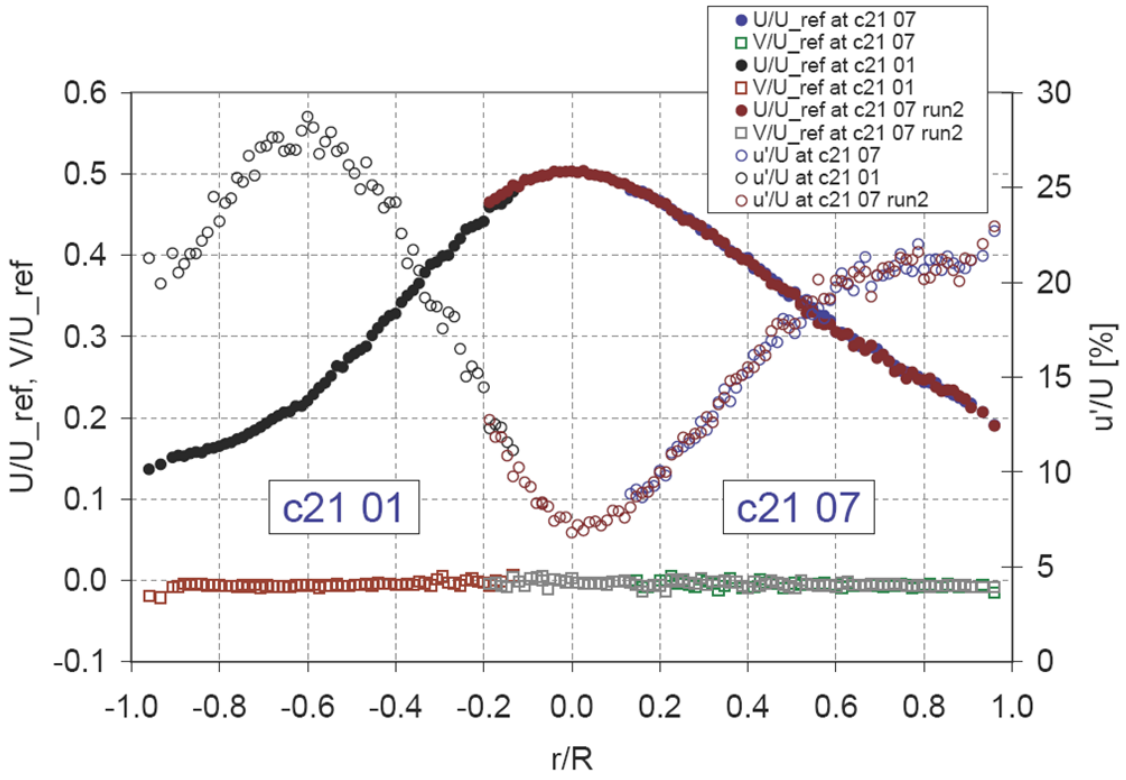

Figure 38. Streamwise (*U*) and azimuthal (*V*) mean velocity, and streamwise turbulence intensity in the tunnel plane of symmetry at corner #2, position 1.

Figure 39 shows LDV measurements in corner #2 before the turning vanes. On the left, the semi-circular positioning plate for the LDV traversing slide can be seen. On the right, several other windows at this position can be seen in the background.

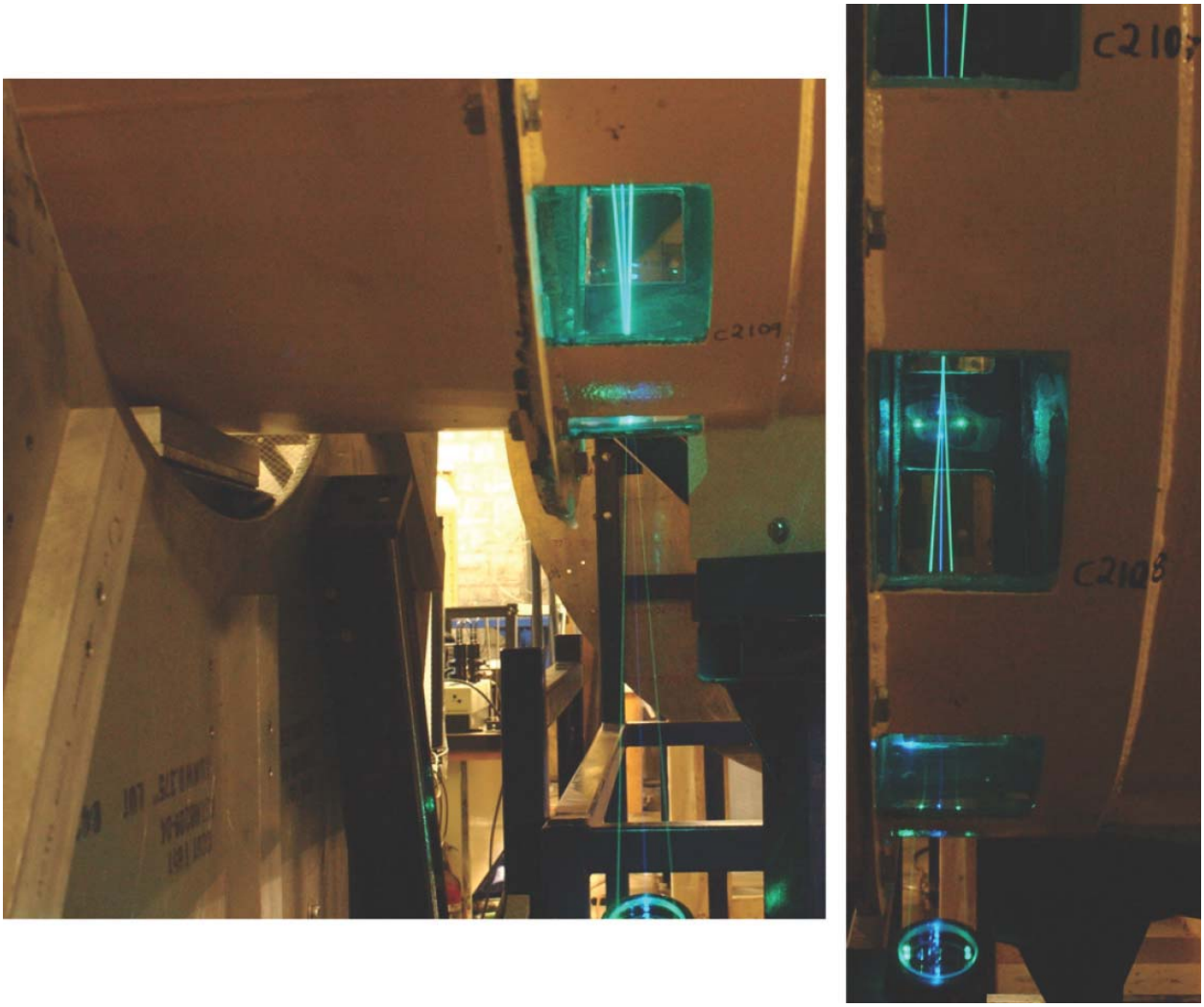

Figure 39. LDV measurements in corner #2, before turning vanes, at position c21 10.

Next, all velocity measurements at corner #2, position 1, are presented. Figure 40 shows the positions of the respective LDV traverses, and Figures 41 through 47 show the data from these traverses.

From these data, contour maps for mean velocity and turbulence intensity were computed, shown in Figure 48 and 49, respectively. The contour plots show a flow with a reasonably symmetrical mean velocity, somewhat skewed towards the outside. Turbulence levels are higher towards the inside and outside of the flow circuit, and lower towards the part of the pipe that corresponds to the 1.2 degree side wall of the diffuser upstream.

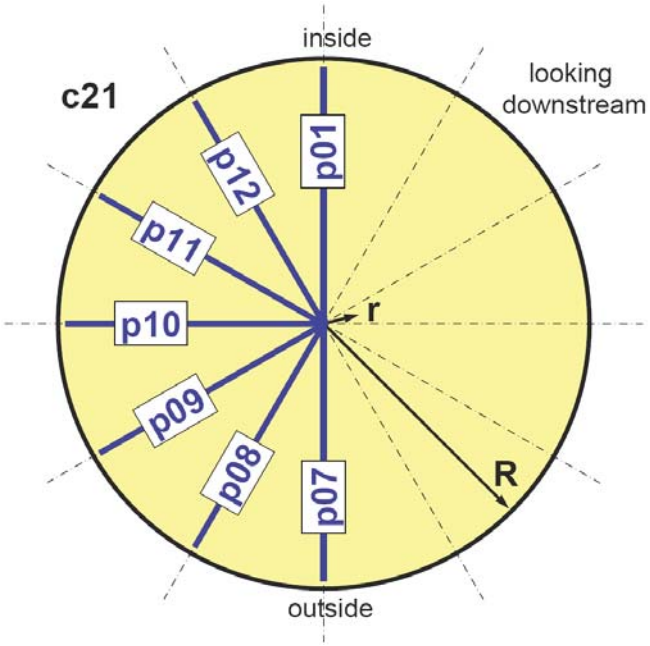

Figure 40. LDV velocity profile measurement positions at corner #2, position 1, in prototype orientation looking downstream. *U* is positive in streamwise direction, $V_{azimuthal}$ is positive in the clockwise direction.

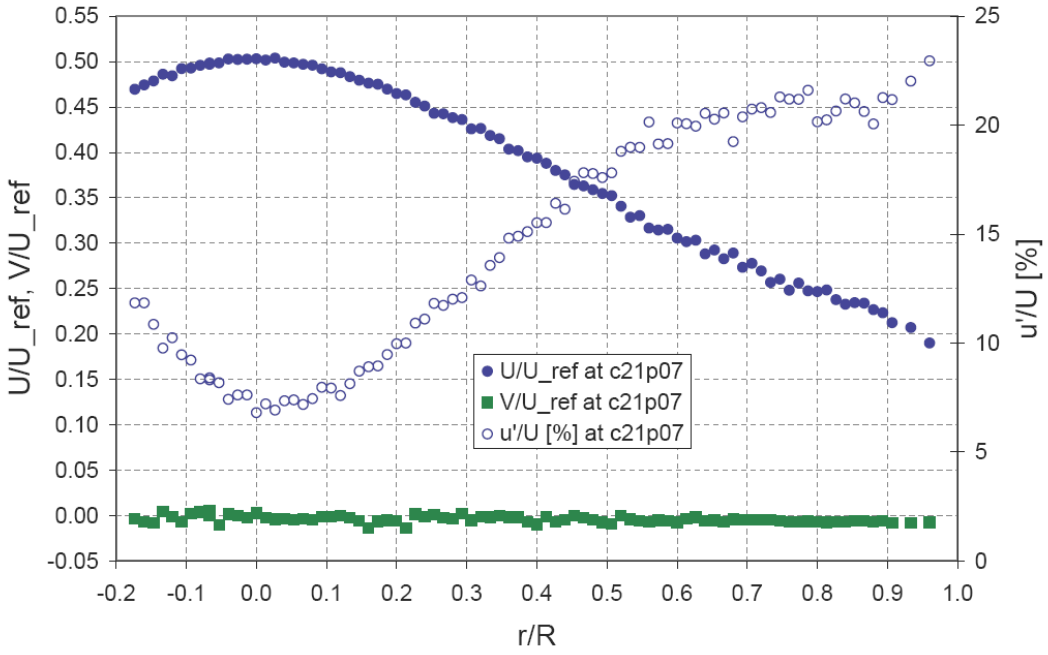

Figure 41. Streamwise (*U*) and azimuthal (*V*) mean velocity, and streamwise turbulence intensity at measurement position p07 at corner #2, position 1.

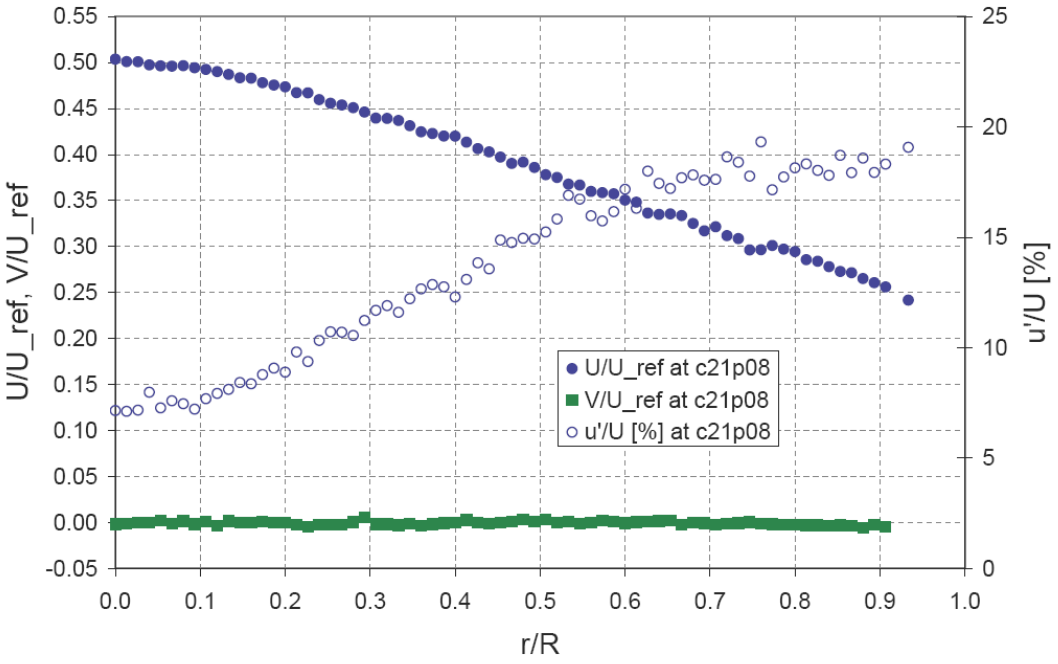

Figure 42. Streamwise (*U*) and azimuthal (*V*) mean velocity, and streamwise turbulence intensity at measurement position p08 at corner #2, position 1.

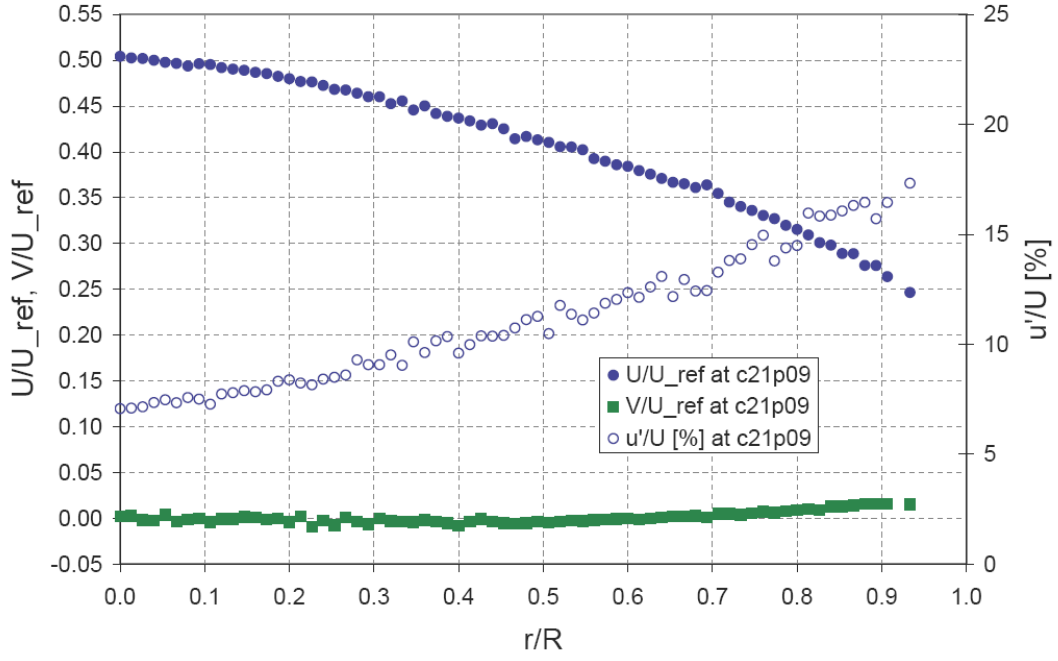

Figure 43. Streamwise (*U*) and azimuthal (*V*) mean velocity, and streamwise turbulence intensity at measurement position p09 at corner #2, position 1.

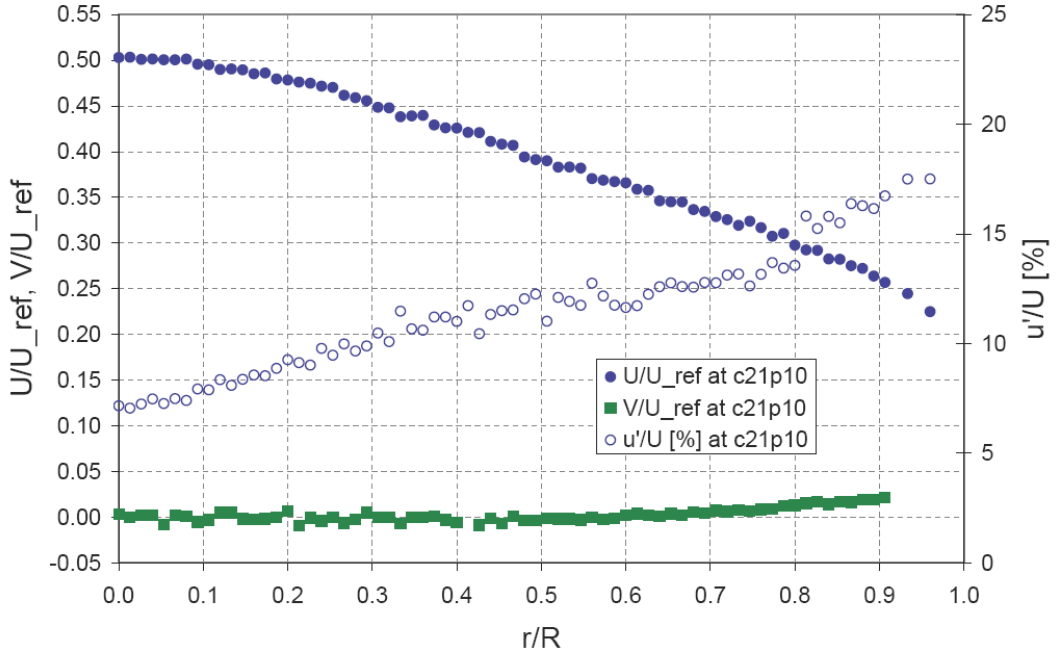

Figure 44. Streamwise (*U*) and azimuthal (*V*) mean velocity, and streamwise turbulence intensity at measurement position p10 at corner #2, position 1.

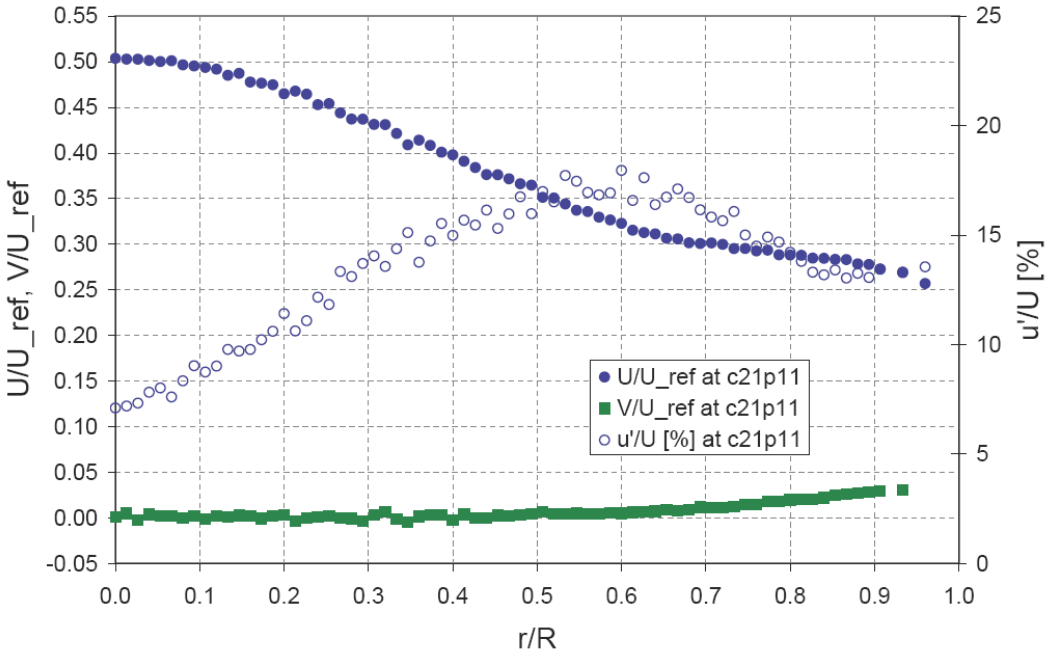

Figure 45. Streamwise (*U*) and azimuthal (*V*) mean velocity, and streamwise turbulence intensity at measurement position p11 at corner #2, position 1.

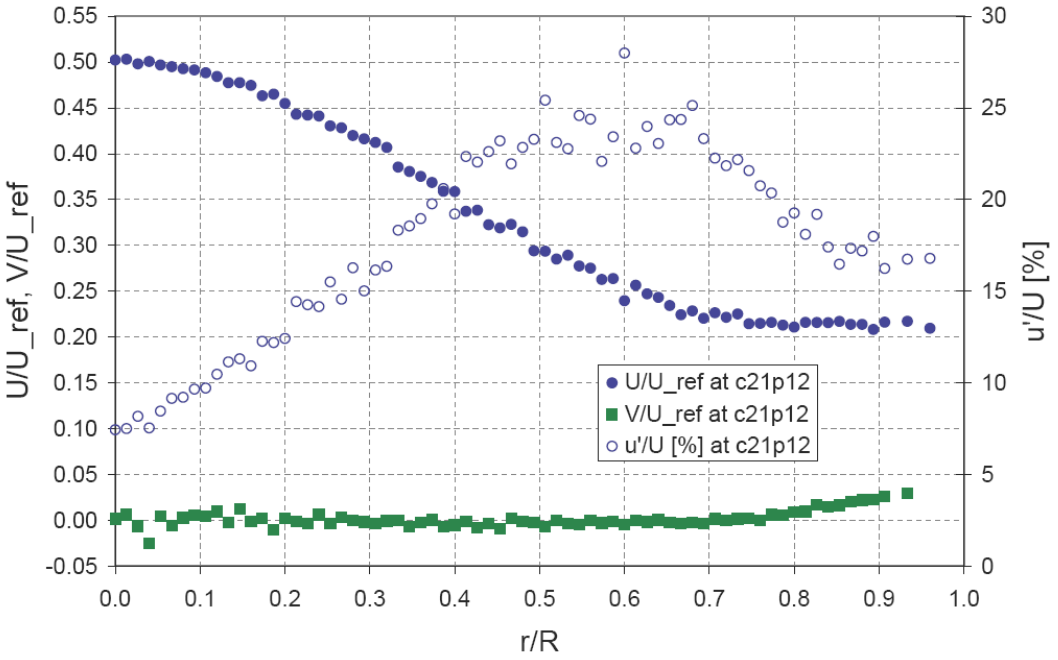

Figure 46. Streamwise (*U*) and azimuthal (*V*) mean velocity, and streamwise turbulence intensity at measurement position p12 at corner #2, position 1.

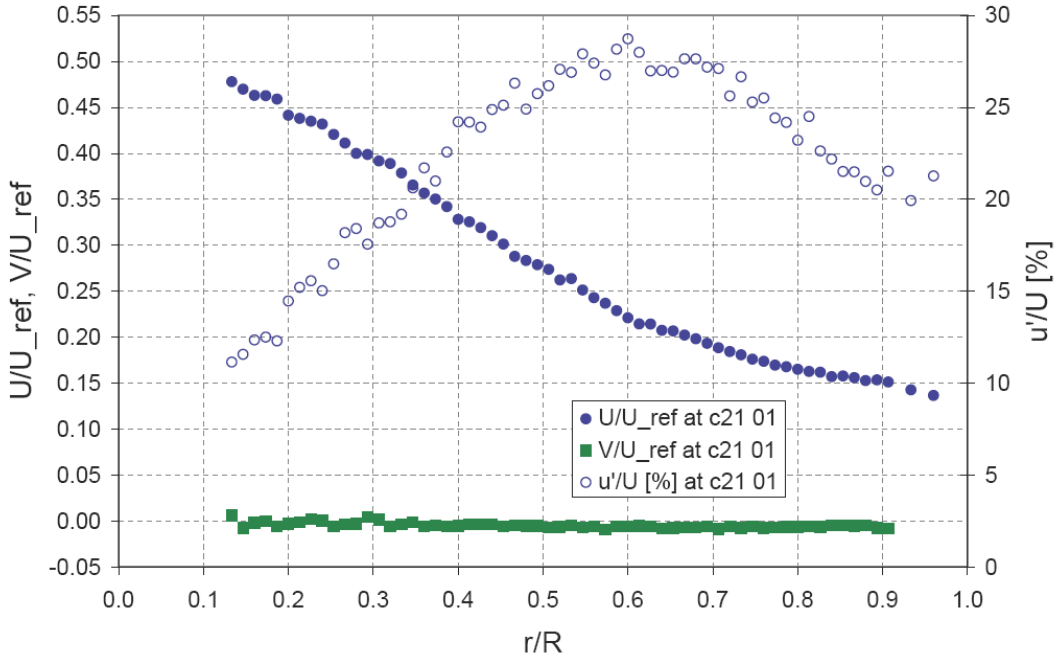

Figure 47. Streamwise (*U*) and azimuthal (*V*) mean velocity, and streamwise turbulence intensity at measurement position p01 at corner #2, position 1.

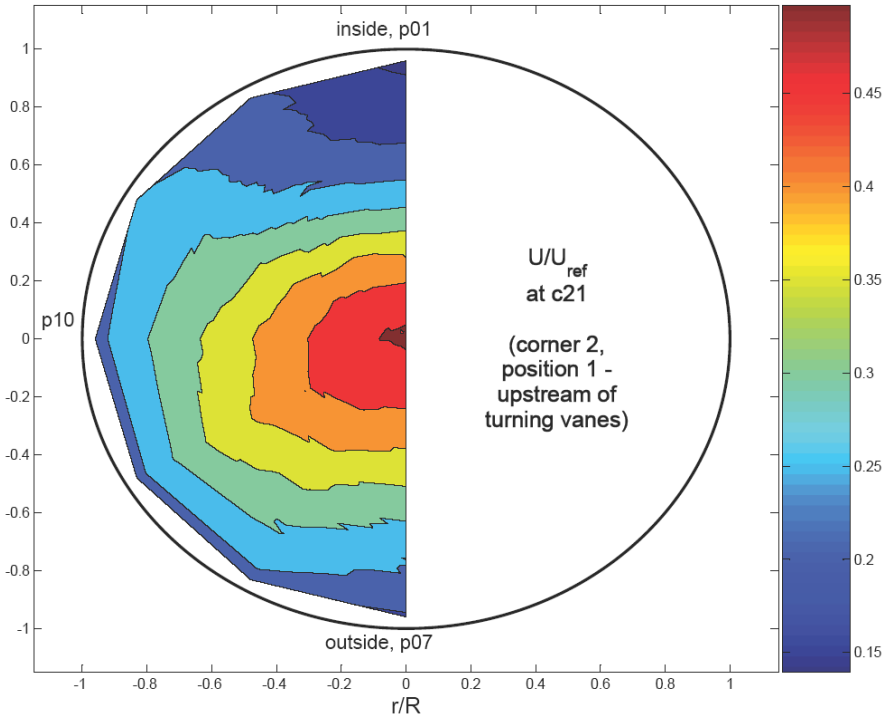

Figure 48. Normalized mean velocity at corner 2, position 1.

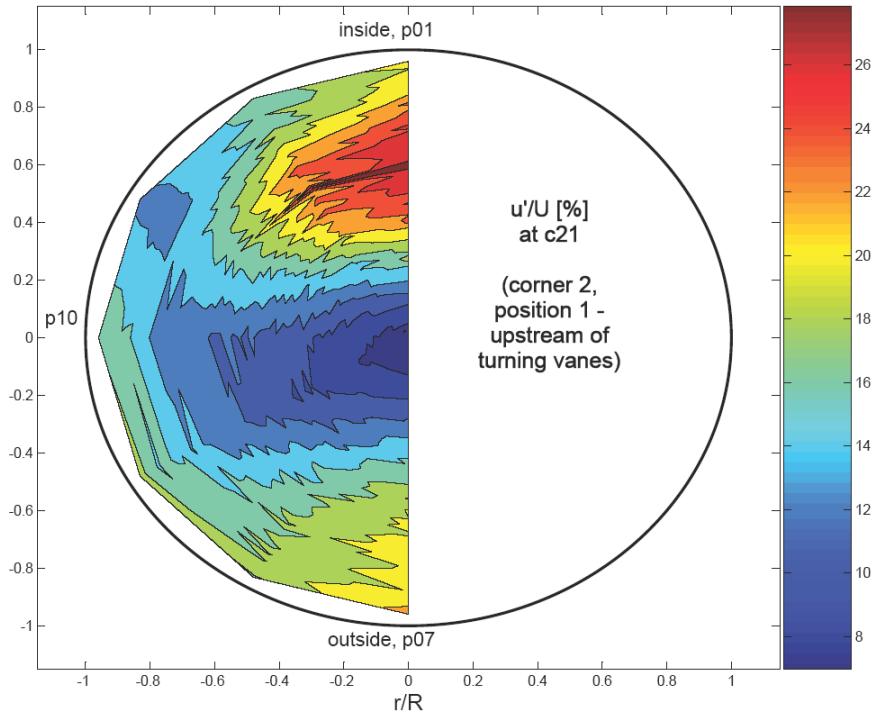

Figure 49. Local turbulence intensity at corner 2, position 1.

Now velocity profiles in the tunnel plane of symmetry at corner #2, position 2, after the turning vanes, are presented. Figure 50 shows the positions of LDV traverses p01 and p07, and Figure 51 shows the data from these traverses, acquired from both sides and measured up to the non-rotating modeled pump shaft. Lower mean velocities and higher turbulence intensities are observed on the outside due to the wake of the pump shaft. On the inside, the imprint of the turning vanes can again be seen, as the flow has not traveled enough distance to recover from the wakes.

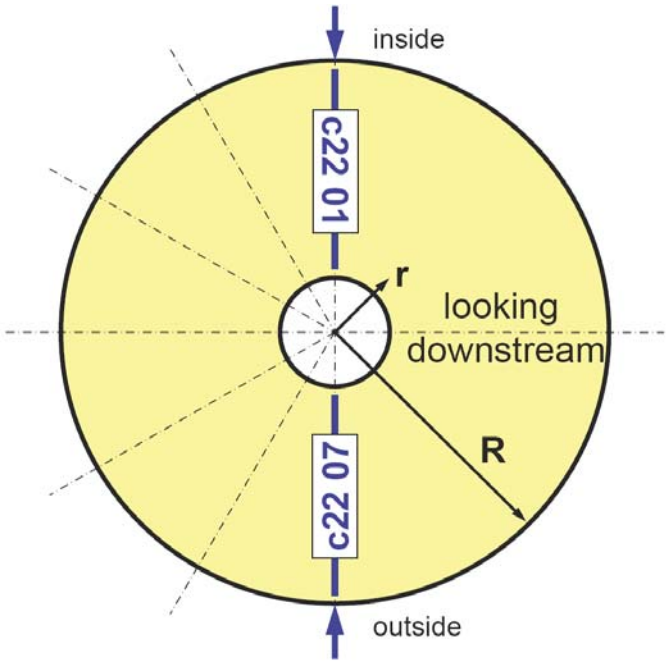

Figure 50. LDV velocity profile measurement positions in the tunnel plane of symmetry at corner #2, position 2, in prototype orientation looking downstream. *U* is positive in streamwise direction, $V_{azimuthal}$ is positive in the clockwise direction.

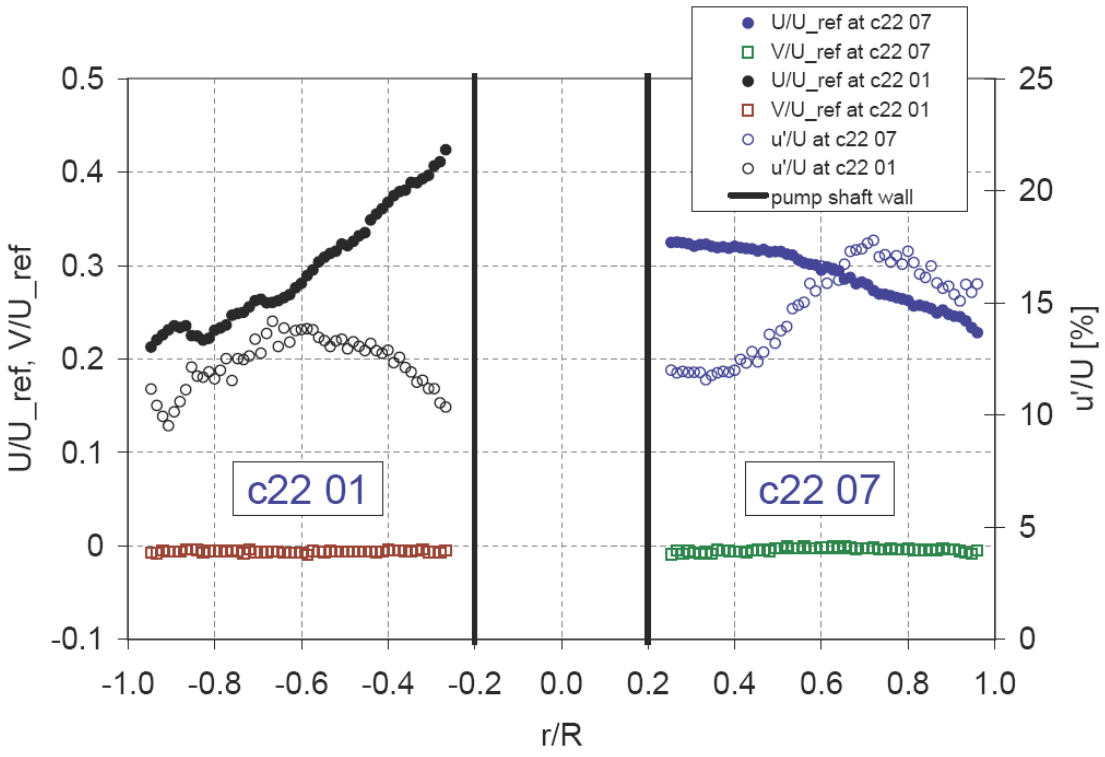

Figure 51. Streamwise (*U*) and azimuthal (*V*) mean velocity, and streamwise turbulence intensity in the tunnel plane of symmetry at corner #2, position 2.

Next, all velocity measurements at corner #2, position 2, are presented. Figure 52 shows the positions of the respective LDV traverses, and Figures 53 through 77 show the data from these traverses.

From these data, contour maps for mean velocity and turbulence intensity were computed, shown in Figure 60 and 61, respectively. The contour plots show a large wake region downstream of the modeled pump shaft, and associated higher turbulence levels. Another region of higher turbulence intensity is observed to the left of the pump shaft near the center; it seems to also be due to the way the mean velocity profiles adjusts because of the pump shaft, possible exacerbated by the way the pump shaft was cut to accommodate the turning vanes.

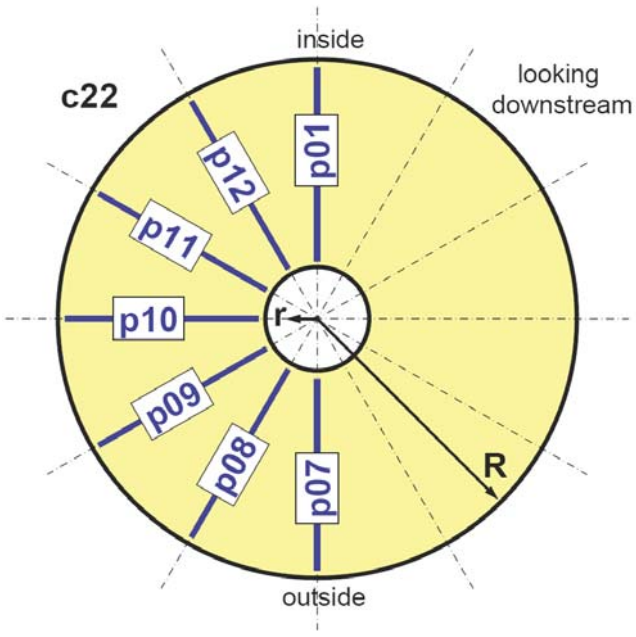

Figure 52. LDV velocity profile measurement positions at corner #2, position 2, in prototype orientation looking downstream. *U* is positive in streamwise direction, $V_{azimuthal}$ is positive in the clockwise direction.

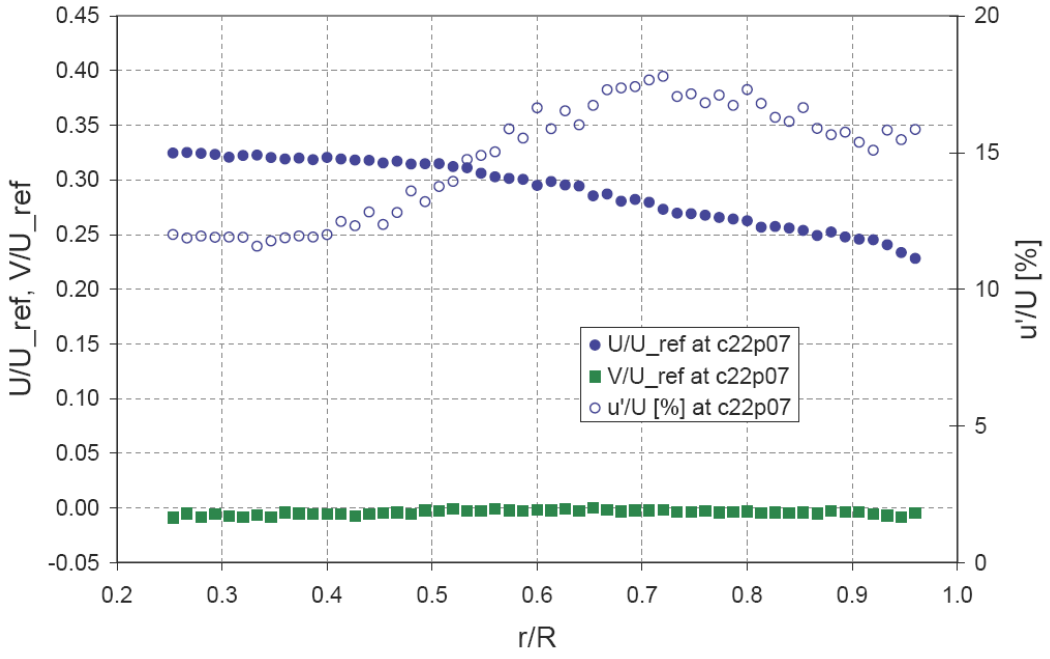

Figure 53. Streamwise (*U*) and azimuthal (*V*) mean velocity, and streamwise turbulence intensity at measurement position p07 at corner #2, position 2.

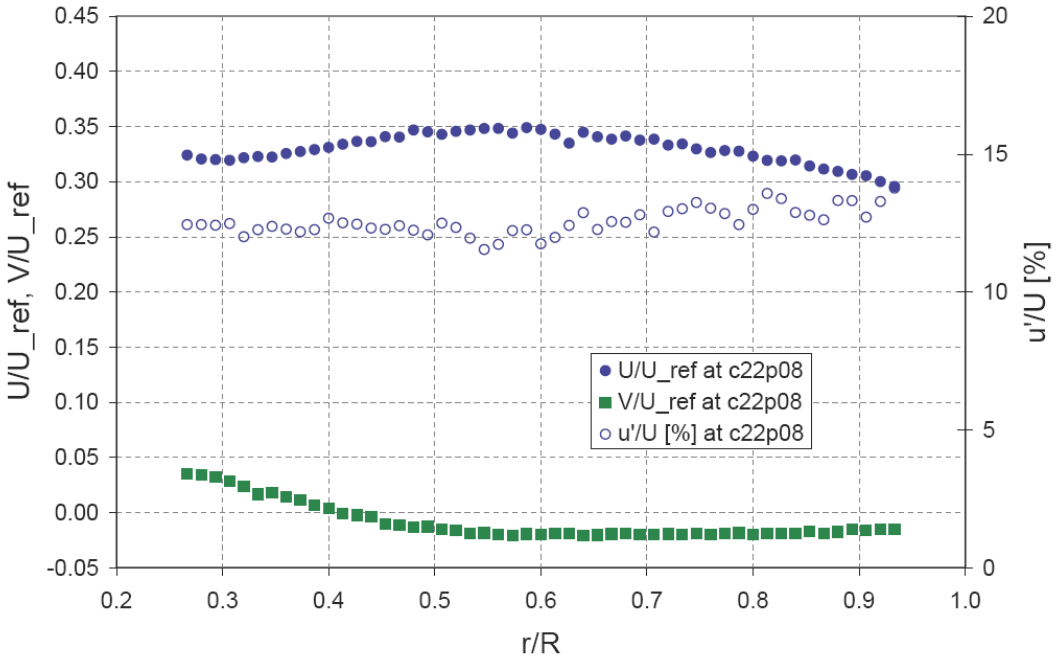

Figure 54. Streamwise (*U*) and azimuthal (*V*) mean velocity, and streamwise turbulence intensity at measurement position p08 at corner #2, position 2.

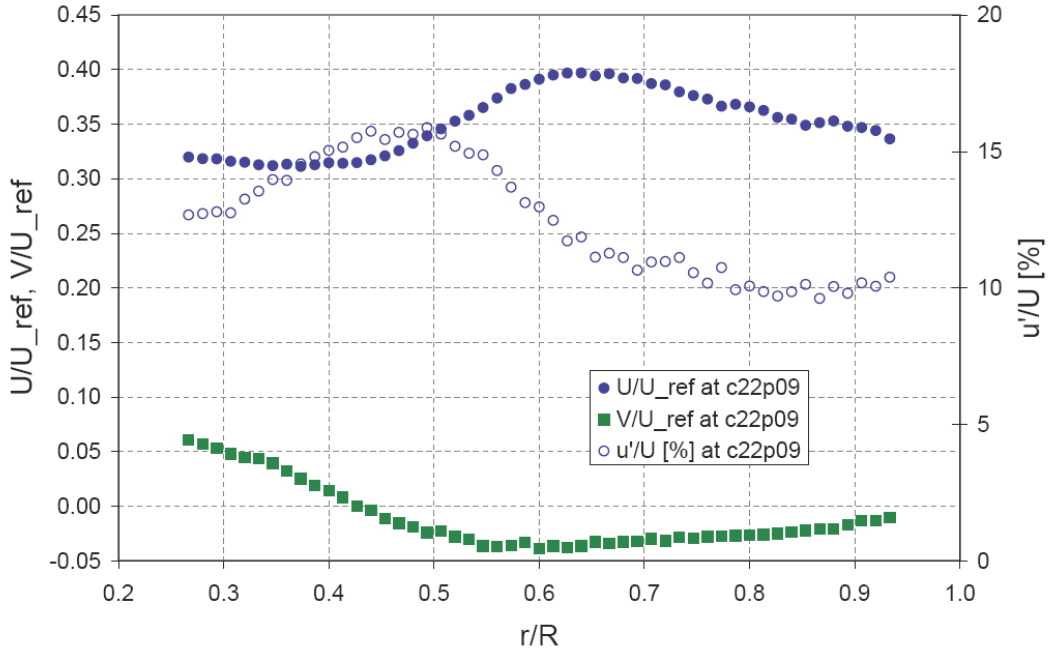

Figure 55. Streamwise (*U*) and azimuthal (*V*) mean velocity, and streamwise turbulence intensity at measurement position p09 at corner #2, position 2.

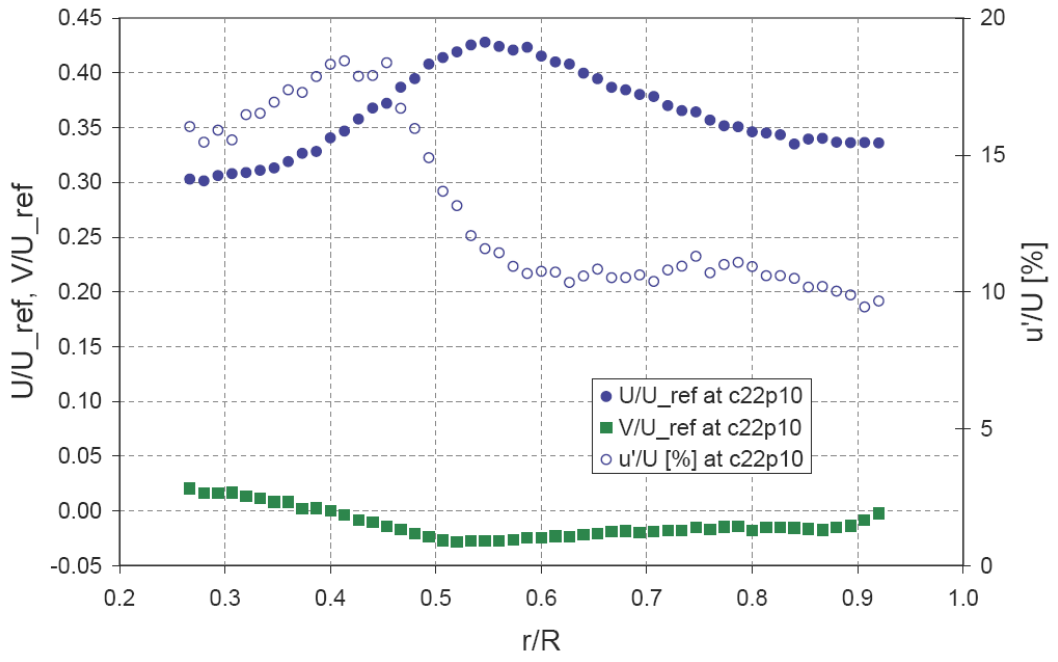

Figure 56. Streamwise (*U*) and azimuthal (*V*) mean velocity, and streamwise turbulence intensity at measurement position p10 at corner #2, position 2.

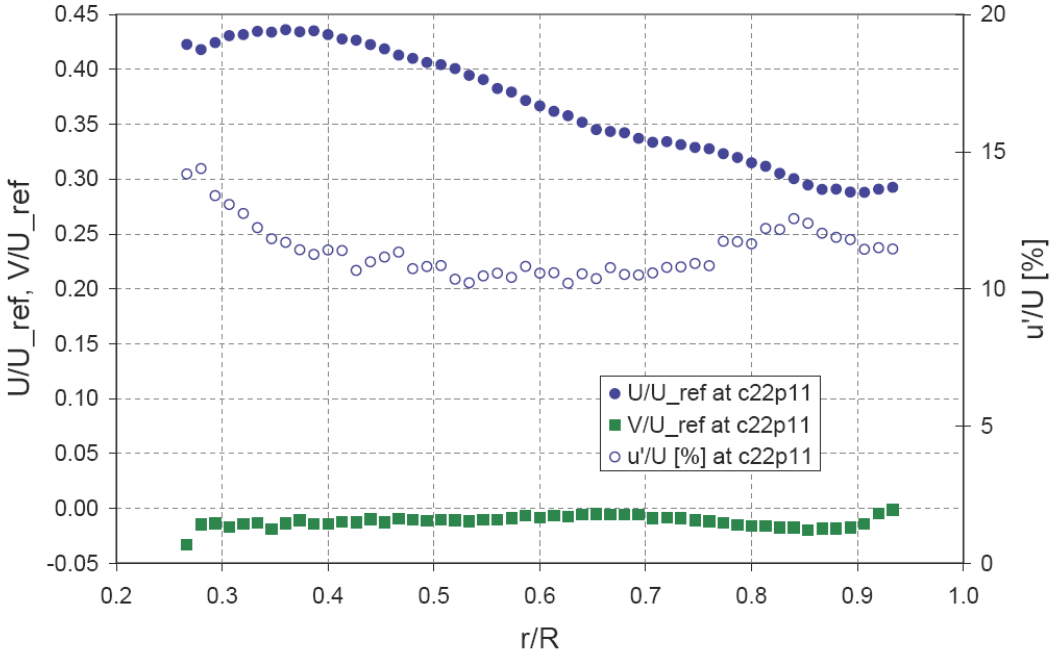

Figure 57. Streamwise (*U*) and azimuthal (*V*) mean velocity, and streamwise turbulence intensity at measurement position p11 at corner #2, position 2.

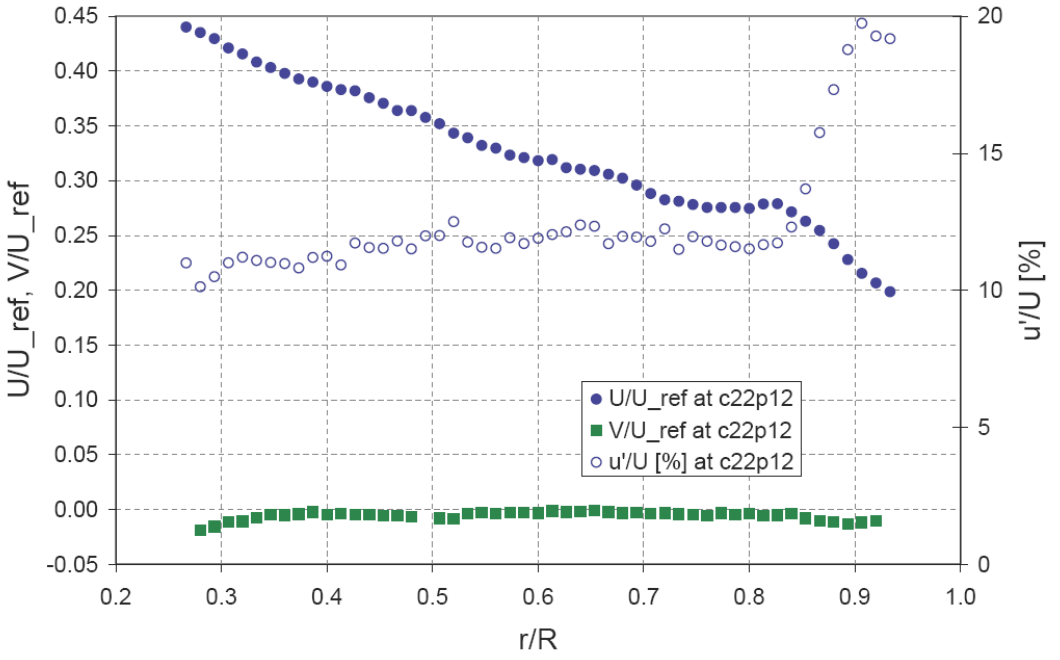

Figure 58. Streamwise (*U*) and azimuthal (*V*) mean velocity, and streamwise turbulence intensity at measurement position p12 at corner #2, position 2.

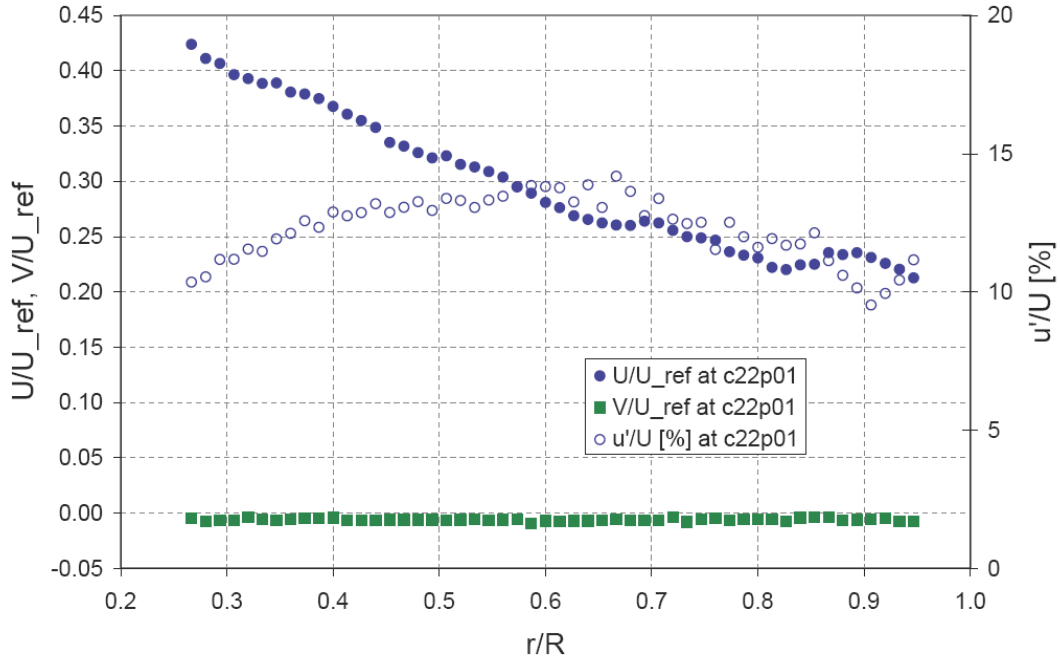

Figure 59. Streamwise (*U*) and azimuthal (*V*) mean velocity, and streamwise turbulence intensity at measurement position p01 at corner #2, position 2.

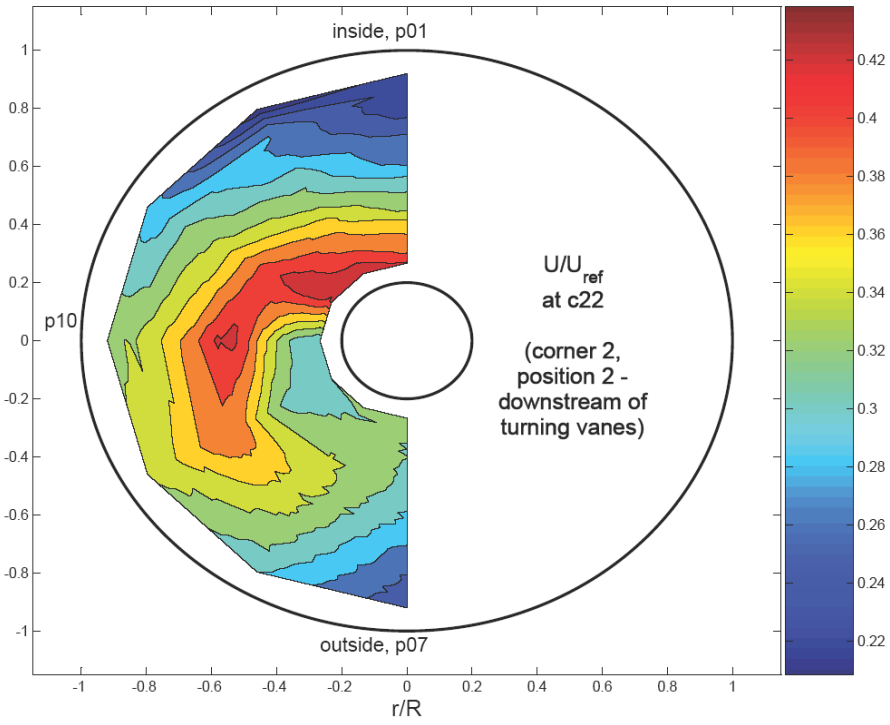

Figure 60. Normalized mean velocity at corner 2, position 2.

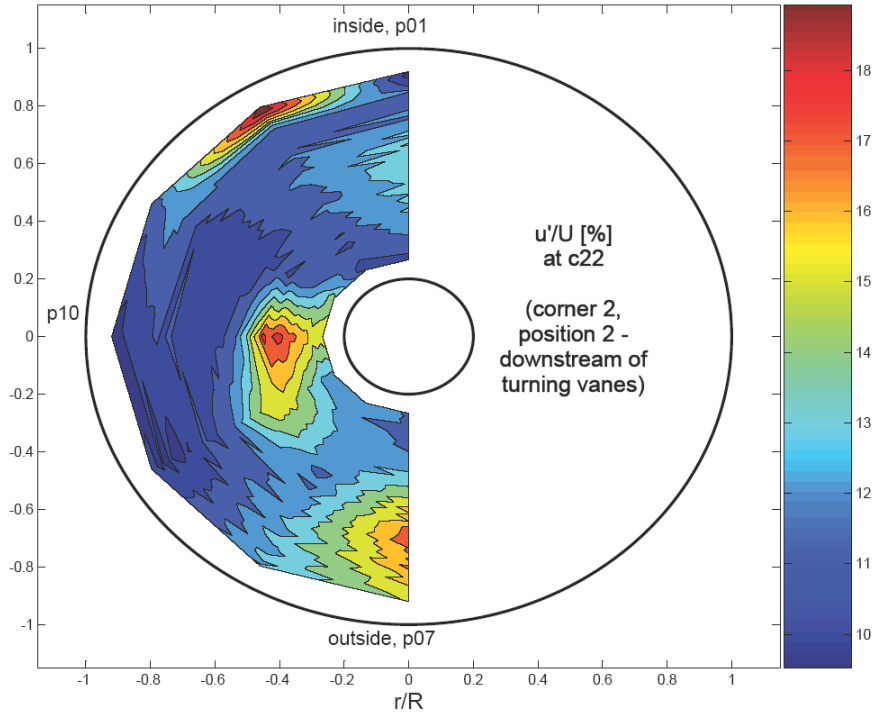

Figure 61. Local turbulence intensity at corner 2, position 2.

4.7. Pump inlet

After corner No. 2 follows a straight section of pipe leading to the pump inlet. At the pump inlet measurement windows (made from 1/8 inch acrylic, recessed into the 1/8 inch steel using a collar) were provided at 12 locations, spaced 30 degrees apart, thus covering a full 360 degree circle. A circular positioning plates for the LDV traversing slide was mounted on a frame on the outside of the model tunnel, and was aligned with the axis of the tunnel using a bearing-supported shaft and a micrometer. Again, shims were used to make the plates flat to within 0.025".

Figure 62 shows the circular positioning plate with the LDV mounted, as well as LDV measurements at various windows.

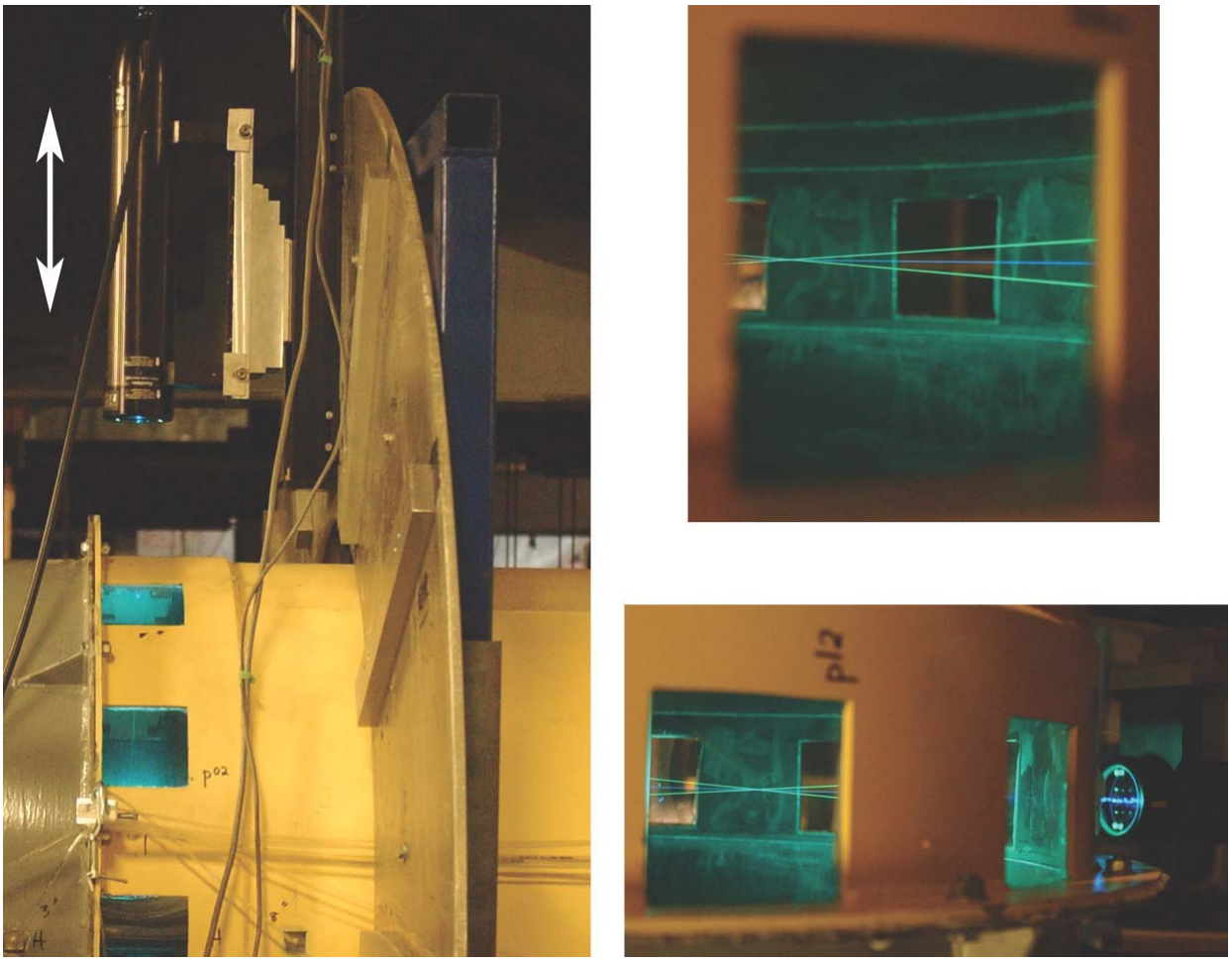

Figure 62. LDV measurements at the pump inlet.

First, velocity profiles in the tunnel plane of symmetry are presented. Figure 63 shows the positions of LDV traverses p01 and p07, and Figure 64 shows the data from these traverses, acquired from both sides and measured up to the non-rotating modeled pump shaft. In this cut through the plane of symmetry it appears that the pump shaft wake has fully recovered, and that the mean velocity profile is skewed just slightly towards the outside. There is a negligible azimuthal component of mean velocity.

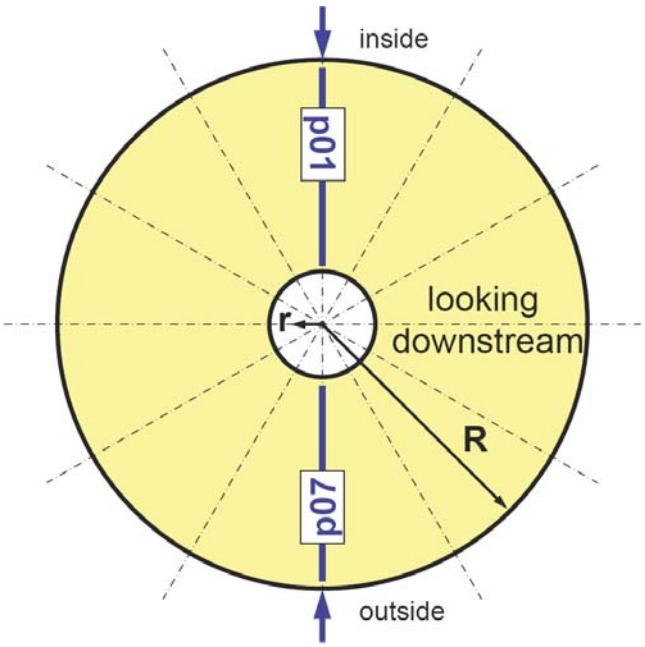

Figure 63. LDV velocity profile measurement positions in the tunnel plane of symmetry at pump inlet, in prototype orientation looking downstream. *U* is positive in streamwise direction, $V_{azimuthal}$ is positive in the clockwise direction.

Next, all 12 velocity measurements at the pump inlet are presented. Figure 65 shows the positions of the respective LDV traverses, and Figures 66 through 59 show the data from these traverses.

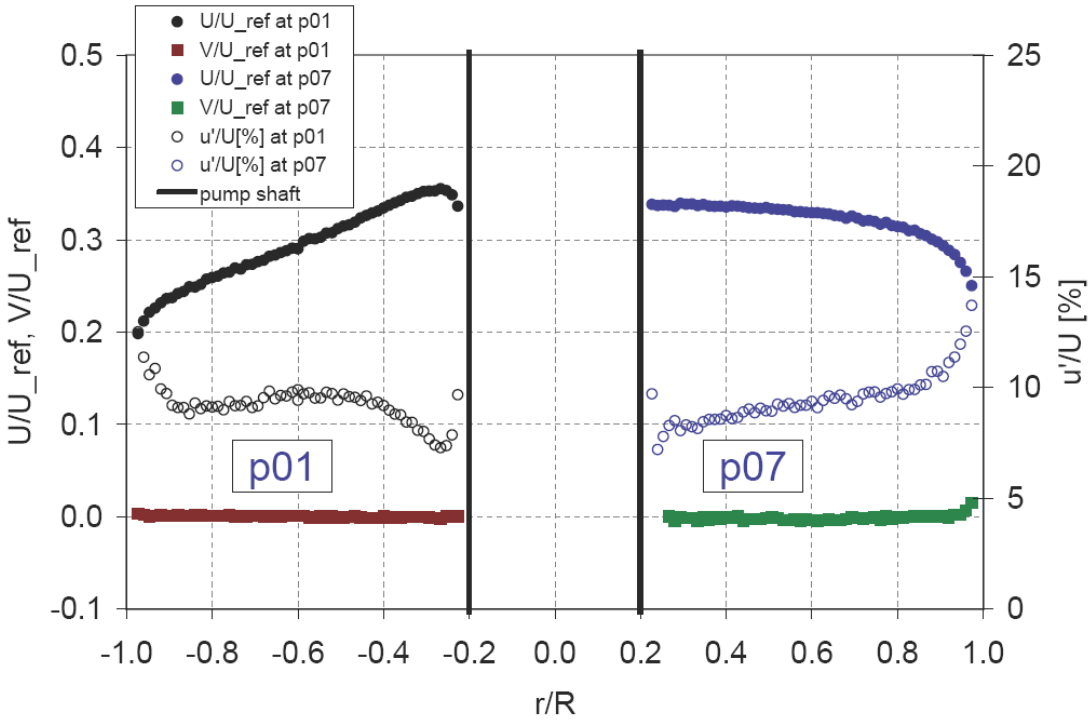

Figure 64. Streamwise (*U*) and azimuthal (*V*) mean velocity, and streamwise turbulence intensity in the tunnel plane of symmetry at pump inlet.

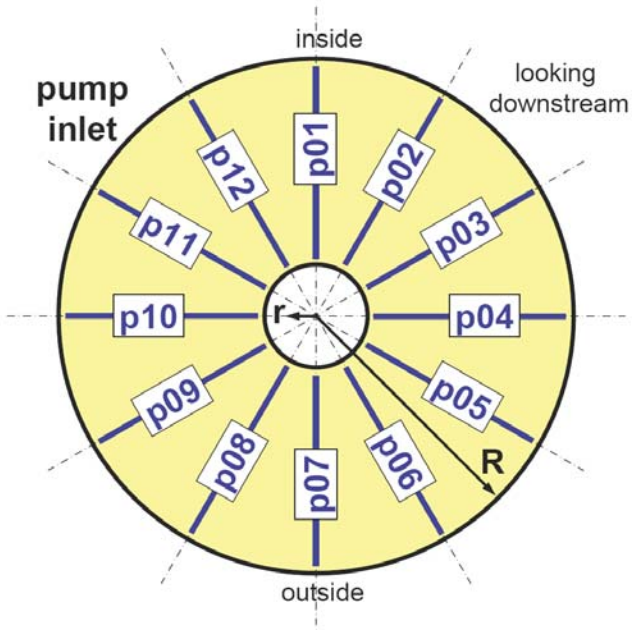

Figure 65. LDV velocity profile measurement positions at pump inlet, in prototype orientation, looking downstream. Radial traversing paths every 30 degrees, *U* is positive in streamwise direction, $V_{azimuthal}$ is positive in clockwise direction.

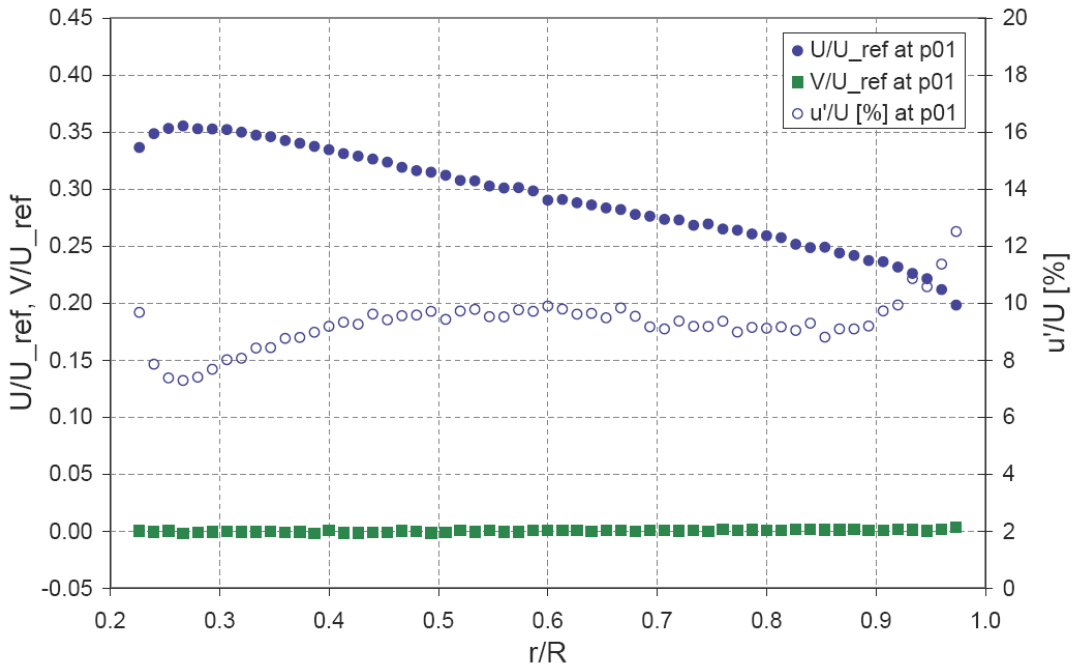

Figure 66. Streamwise (*U*) and azimuthal (*V*) mean velocity, and streamwise turbulence intensity at position p01 at pump inlet.

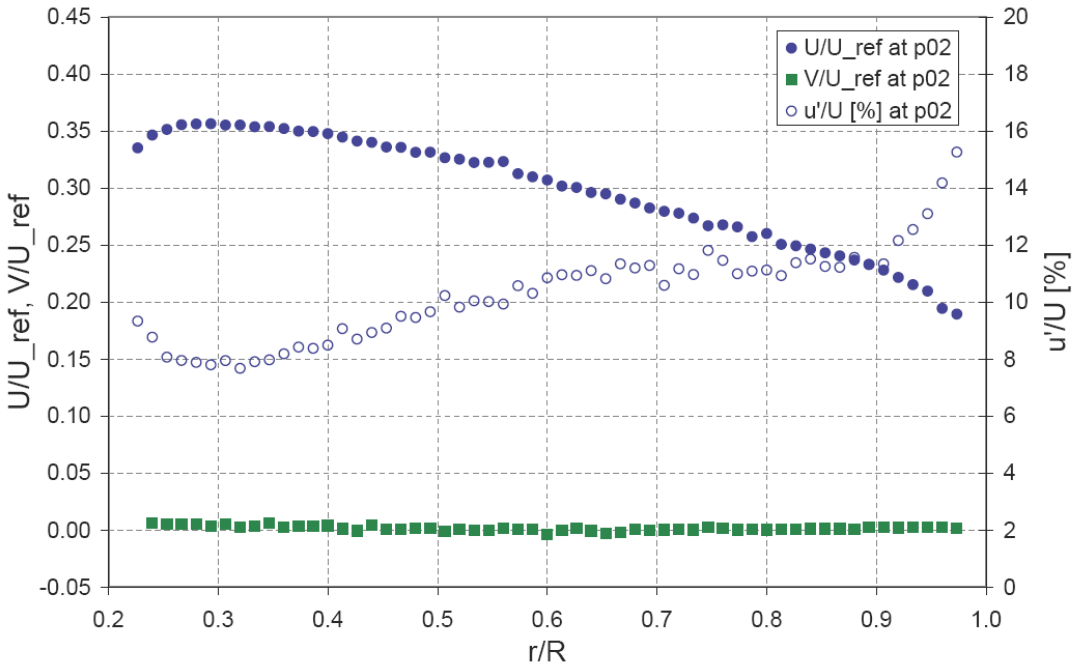

Figure 67. Streamwise (*U*) and azimuthal (*V*) mean velocity, and streamwise turbulence intensity at position p02 at pump inlet.

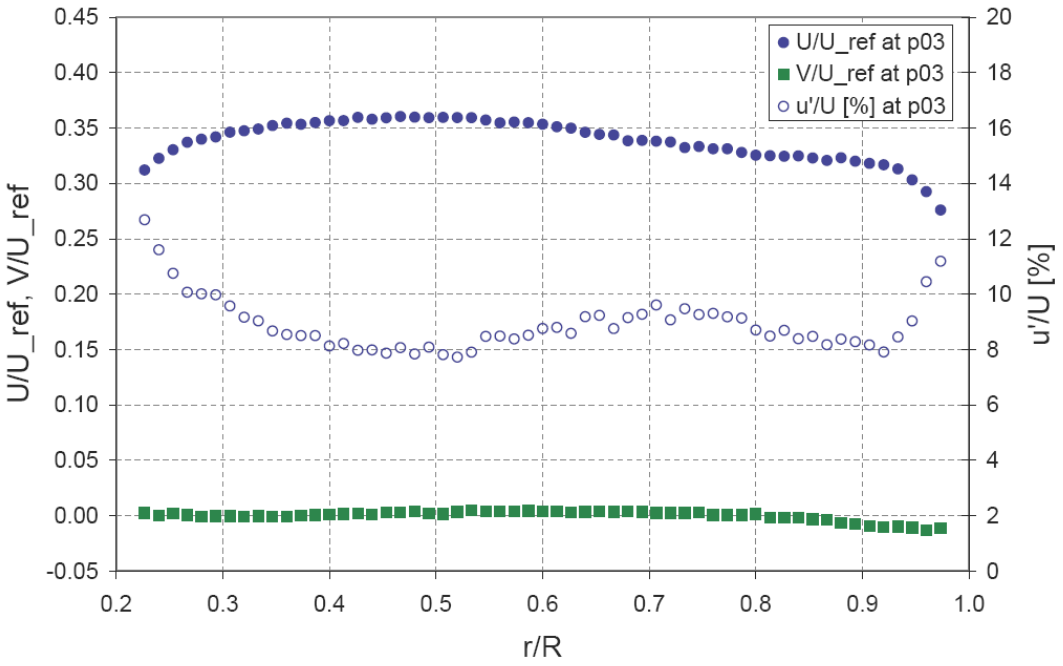

Figure 68. Streamwise (*U*) and azimuthal (*V*) mean velocity, and streamwise turbulence intensity at position p03 at pump inlet.

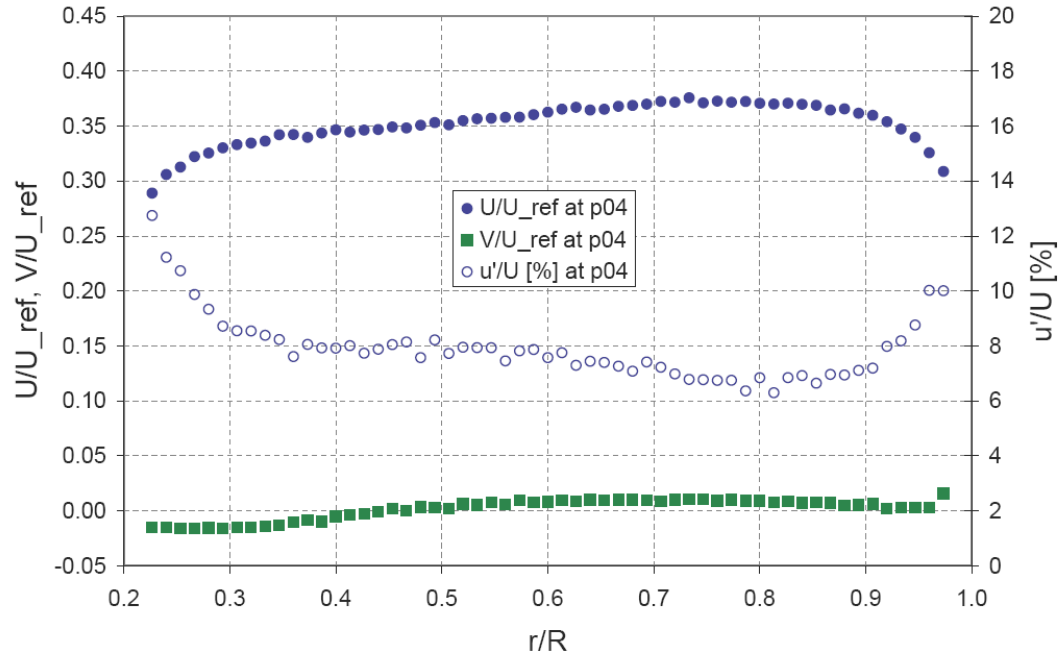

Figure 69. Streamwise (*U*) and azimuthal (*V*) mean velocity, and streamwise turbulence intensity at position p04 at pump inlet.

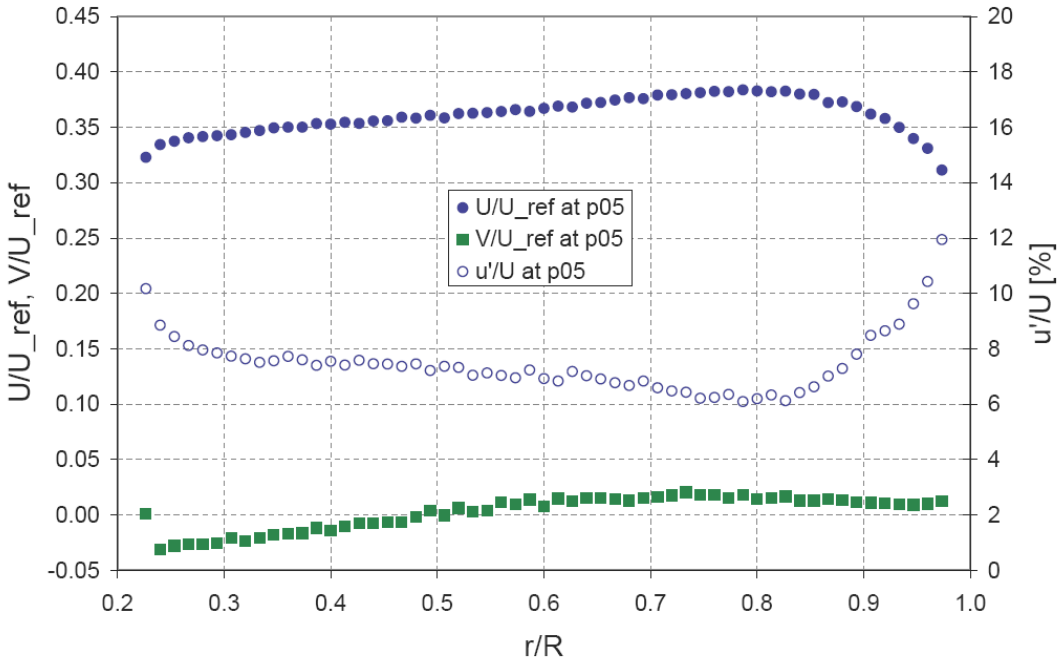

Figure 70. Streamwise (*U*) and azimuthal (*V*) mean velocity, and streamwise turbulence intensity at position p05 at pump inlet.

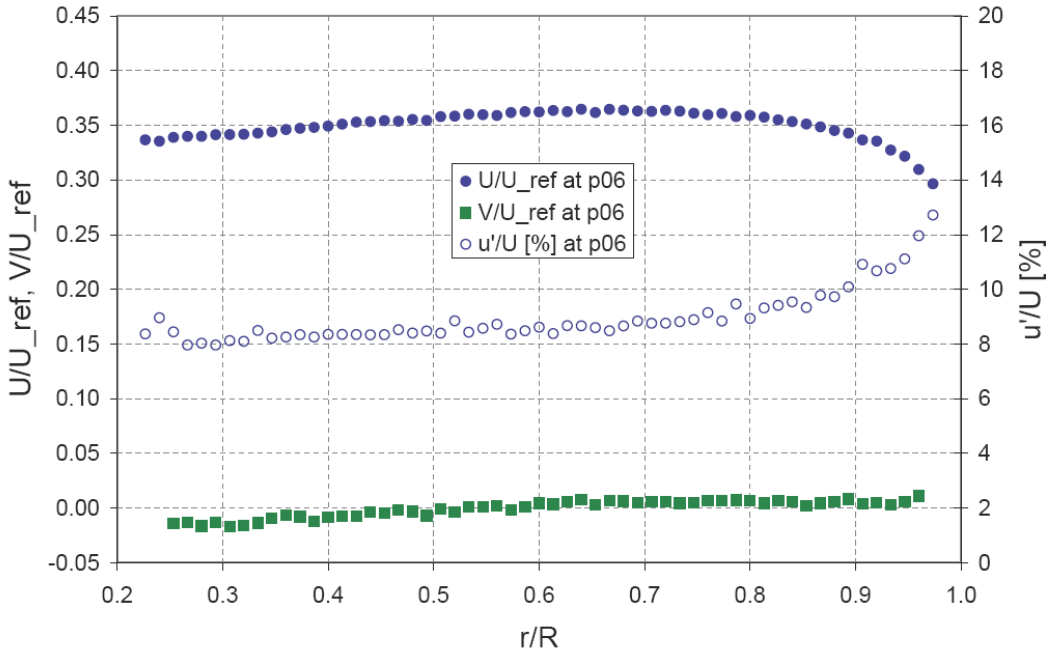

Figure 71. Streamwise (*U*) and azimuthal (*V*) mean velocity, and streamwise turbulence intensity at position p06 at pump inlet.

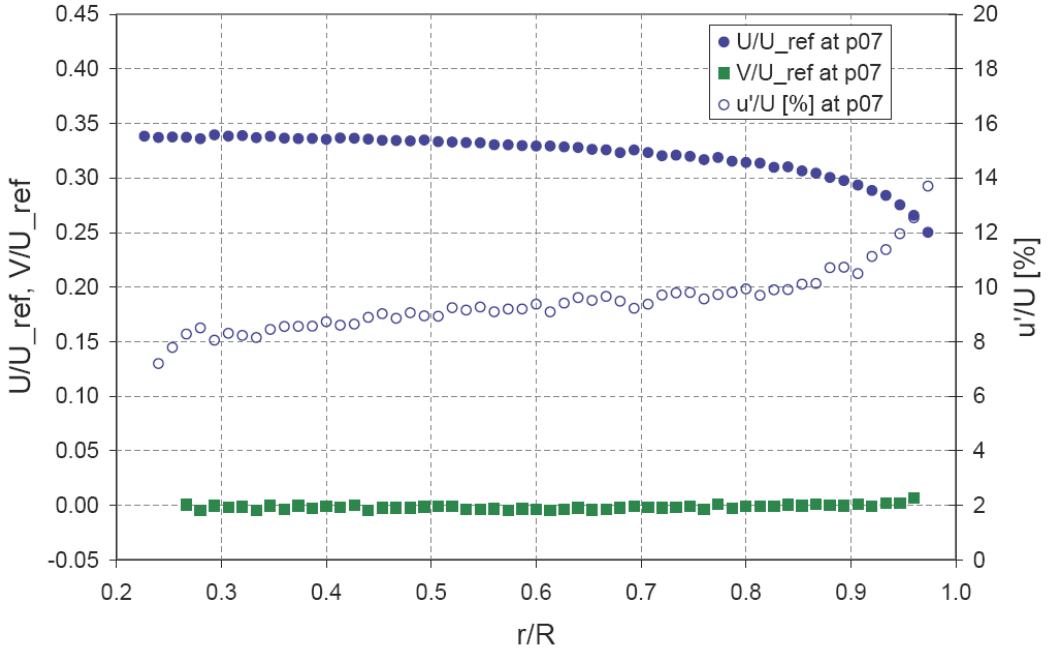

Figure 72. Streamwise (*U*) and azimuthal (*V*) mean velocity, and streamwise turbulence intensity at position p07 at pump inlet.

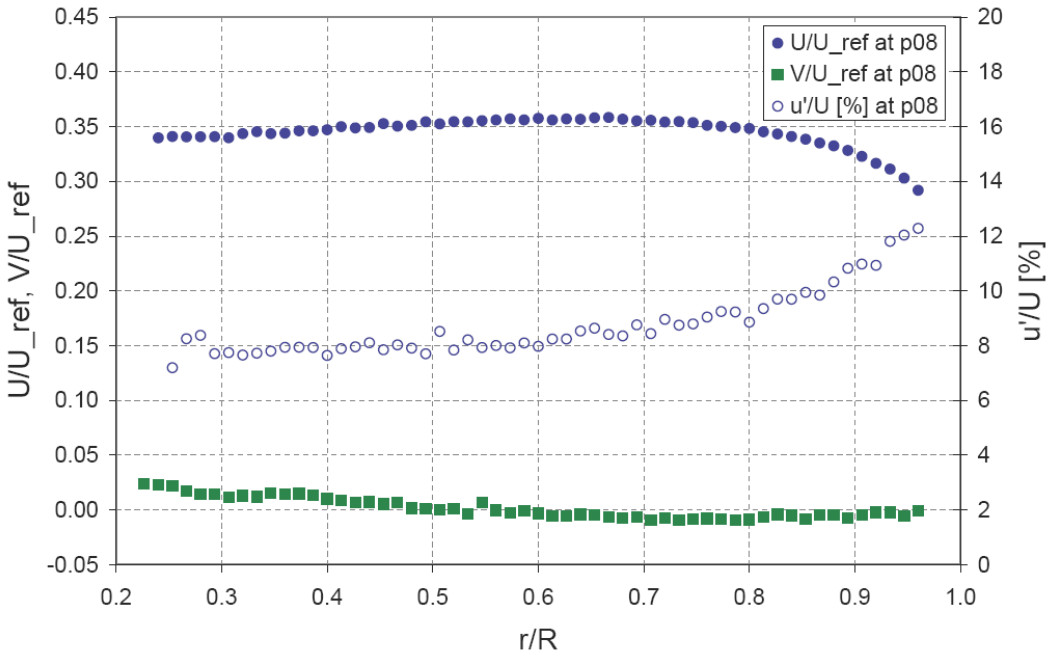

Figure 73. Streamwise (*U*) and azimuthal (*V*) mean velocity, and streamwise turbulence intensity at position p08 at pump inlet.

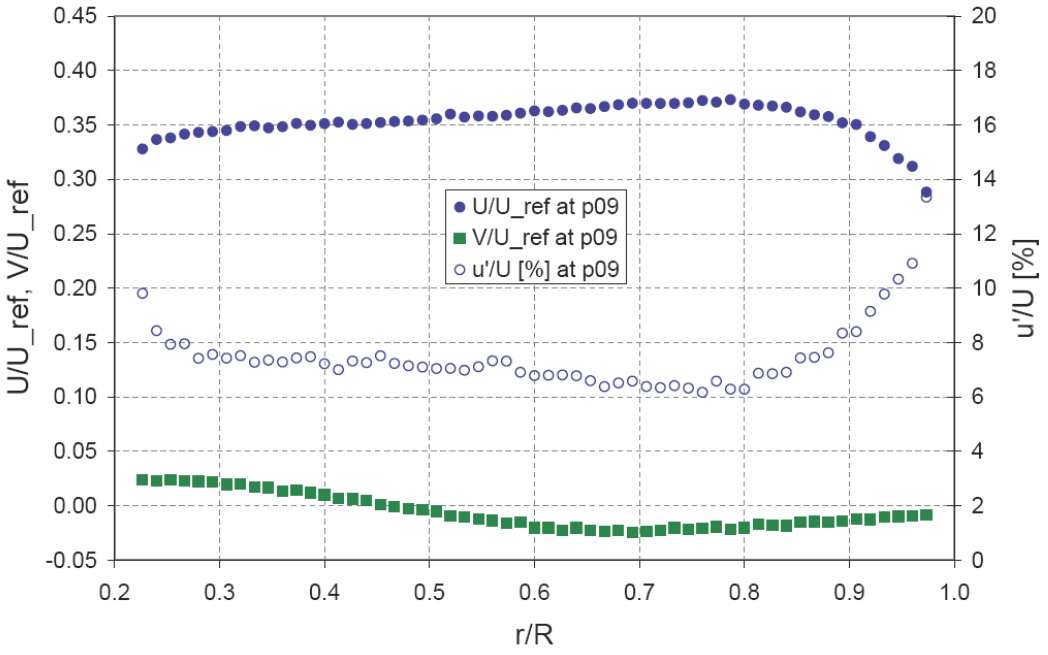

Figure 74. Streamwise (*U*) and azimuthal (*V*) mean velocity, and streamwise turbulence intensity at position p09 at pump inlet.

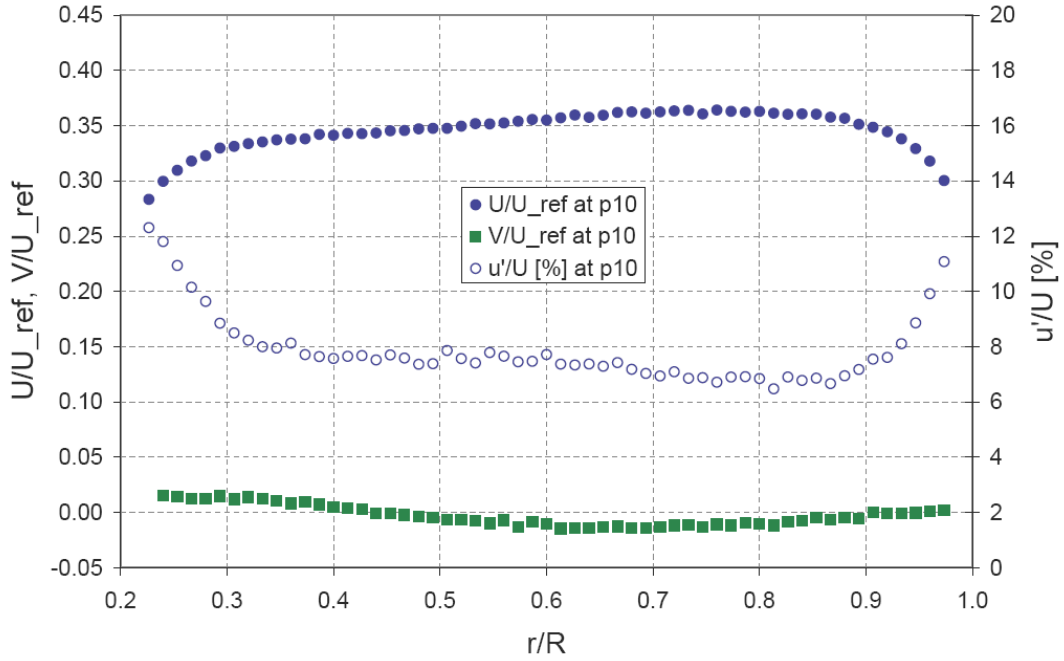

Figure 75. Streamwise (*U*) and azimuthal (*V*) mean velocity, and streamwise turbulence intensity at position p10 at pump inlet.

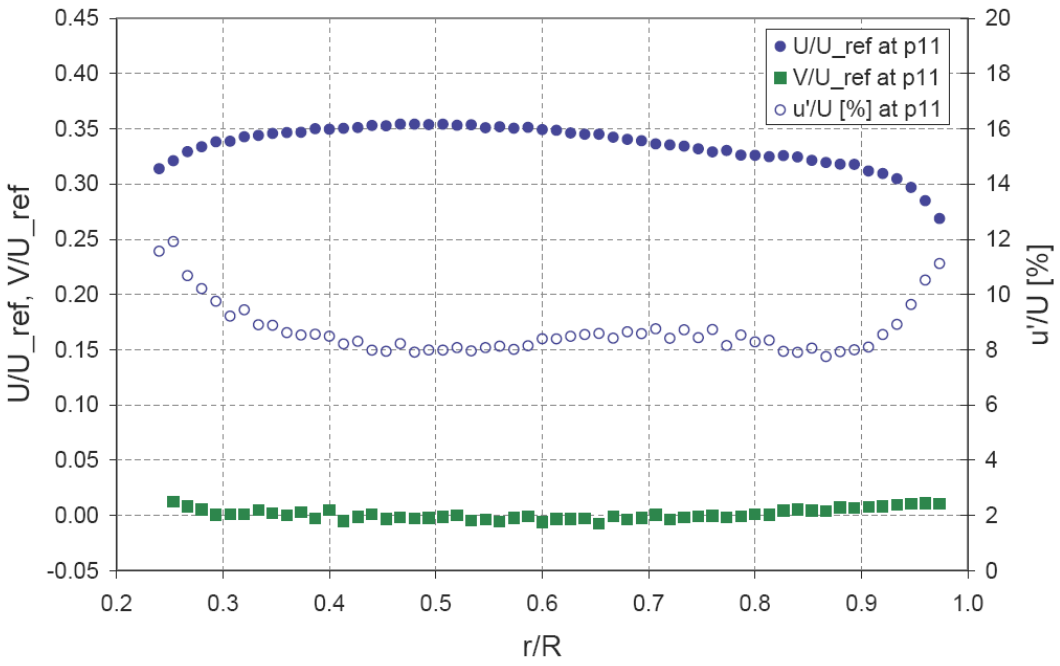

Figure 76. Streamwise (*U*) and azimuthal (*V*) mean velocity, and streamwise turbulence intensity at position p11 at pump inlet.

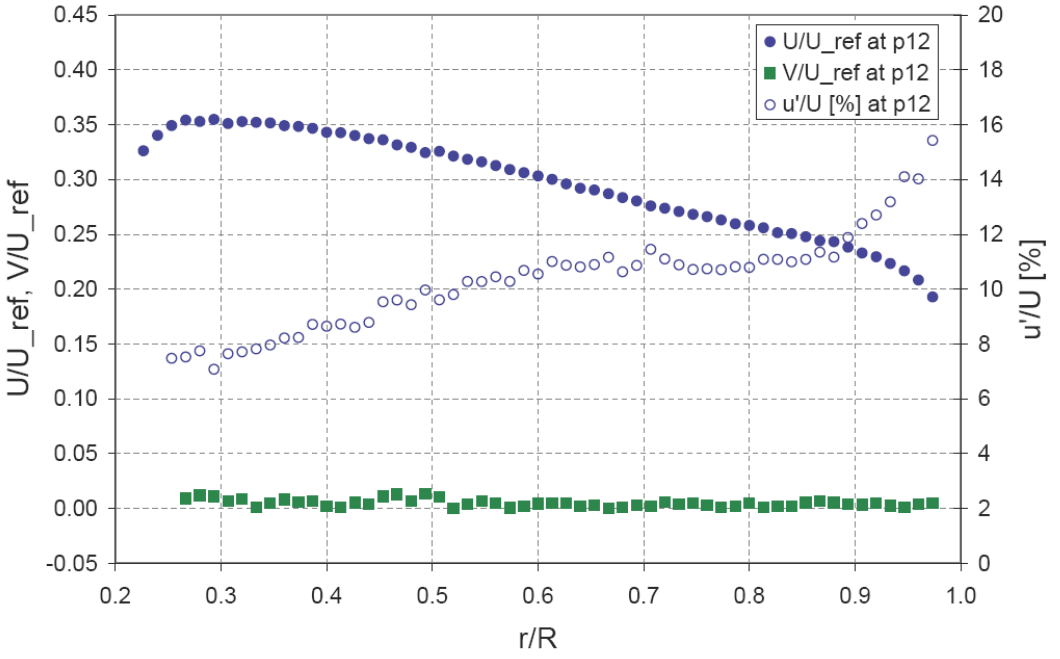

Figure 77. Streamwise (*U*) and azimuthal (*V*) mean velocity, and streamwise turbulence intensity at position p12 at pump inlet.

From the data of the these 12 traverses, contour maps for mean streamwise velocity, turbulence intensity and mean azimuthal velocity (swirl) were computed, shown in Figure 78, 79 and 80, respectively. The contour plots show that the wake region downstream of the modeled pump shaft still exists, and that the mean flow is skewed towards the outside. While there is a hint of a pump shaft wake region in the turbulence intensity contours in Figure 79, the regions of higher turbulence intensity observed in Figure 61 appear to have decayed. There is little swirl at the pump inlet, as the azimuthal component of mean velocity is very small (note the scale).

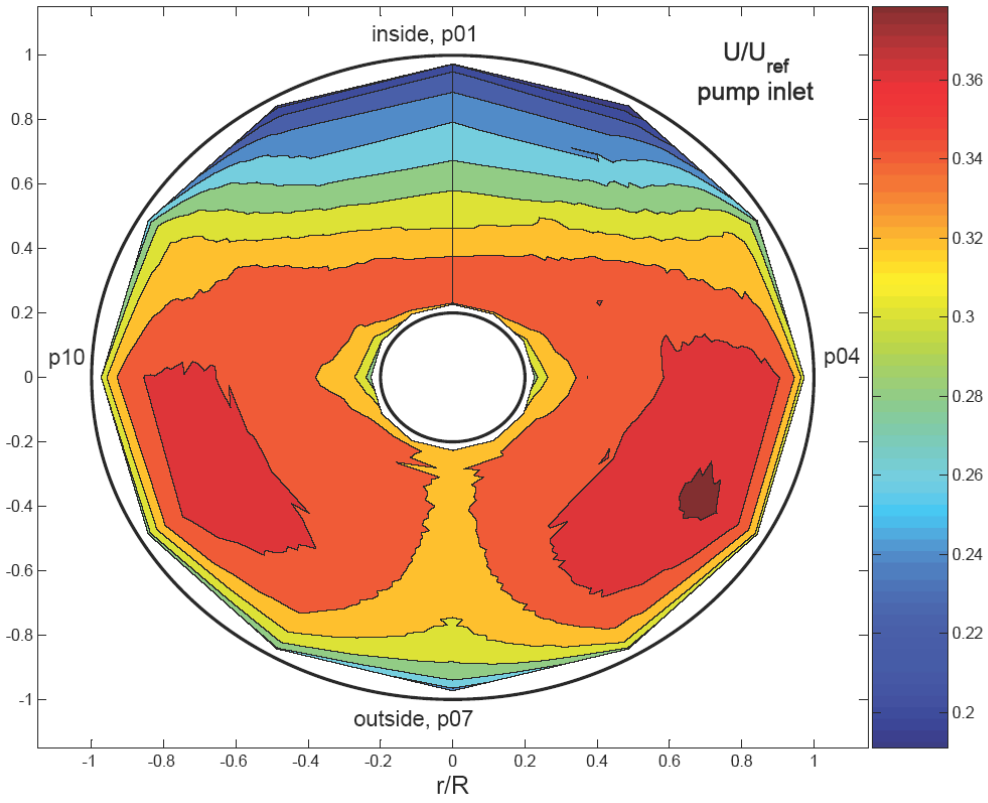

Figure 78. Normalized streamwise mean velocity at pump inlet.

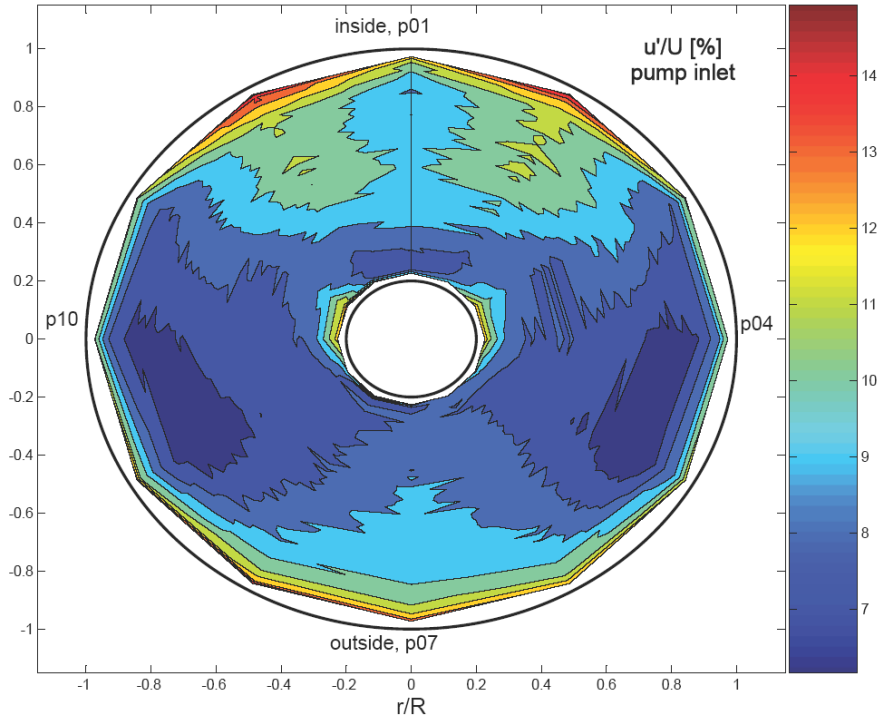

Figure 79. Local streamwise turbulence intensity at pump inlet.

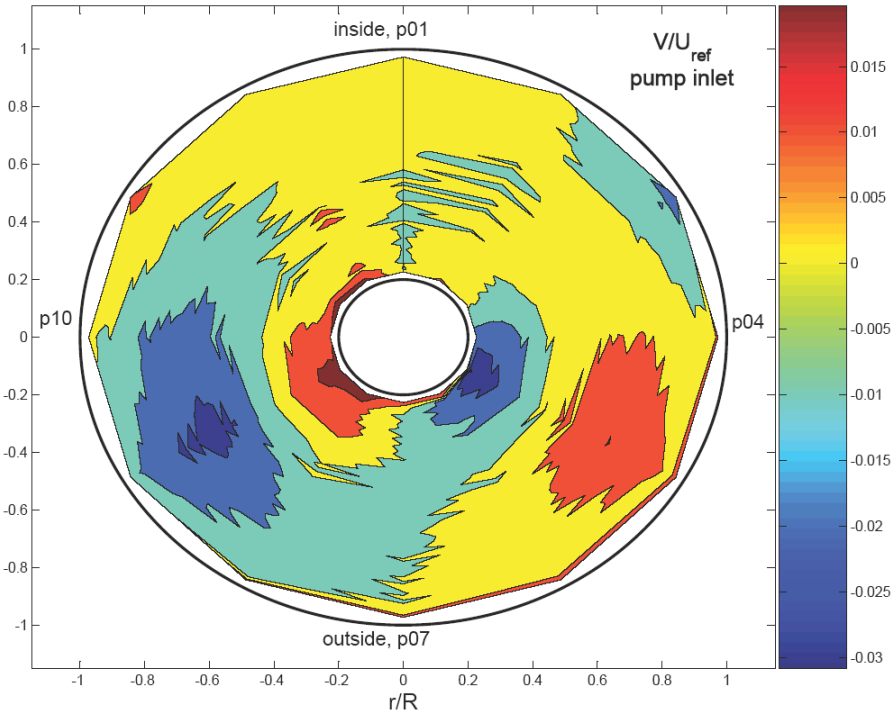

Figure 80. Normalized azimuthal mean velocity at pump inlet.

4.8. Flow uniformity - comparison of center-plane and quarter-plane

To check the flow uniformity, additional measurements at the quarter-plane, $z/W = 0.25$, of all rectangular cross-sections were performed. The position of the quarter-plane LDV traverse is shown in Figure 22.

Beginning with corner No.4, it can be seen in Figure 81 that the flow is reasonable uniform at inflow before the turning vanes. At quarter width, $z/W = 0.25$, it is slightly slower and more uniform across in the cross-stream direction y than at the plane of symmetry. This small difference is carried through the turning vanes, as can be seen in Figure 82. However, the difference diminishes through the honeycombs, and both mean velocity and turbulence intensity match very well at the plane of symmetry, $z/W = 0$, and quarter width, $z/W = 0.25$, as can be seen in Figures 83 and 84. From Figure 84 it can be concluded that the flow is very uniform across the width z, but not the height y, before it enters the contraction.

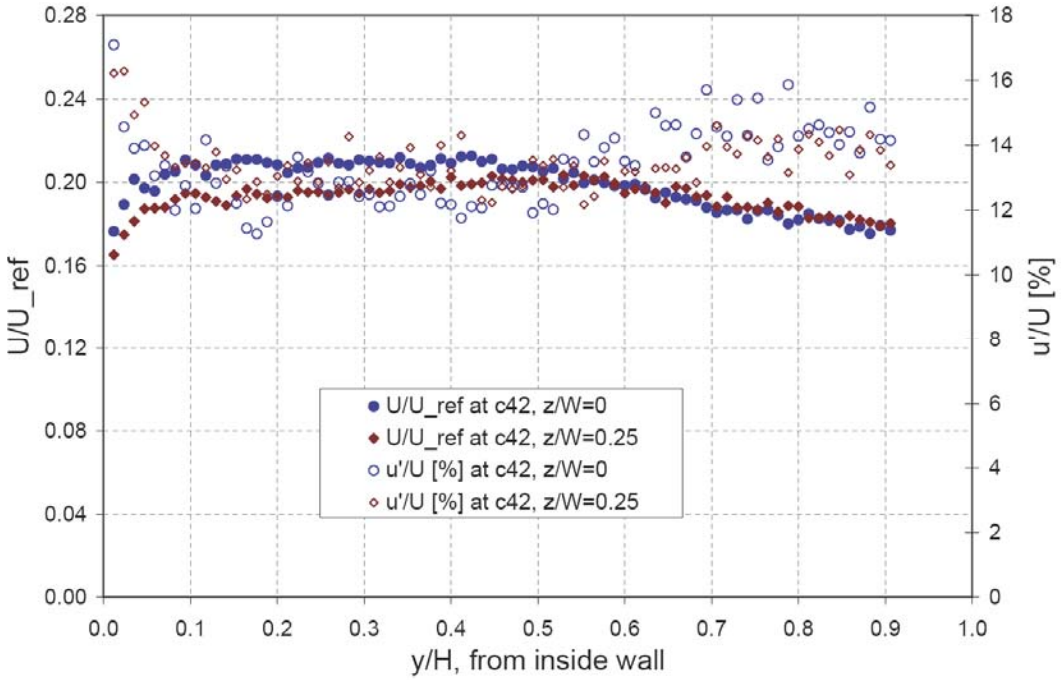

Figure 81. Comparison of streamwise mean velocity and turbulence intensity in the tunnel plane of symmetry (z/W=0) and at quarter width (z/W=0.25) at corner #4, position 2 (before turning vanes).

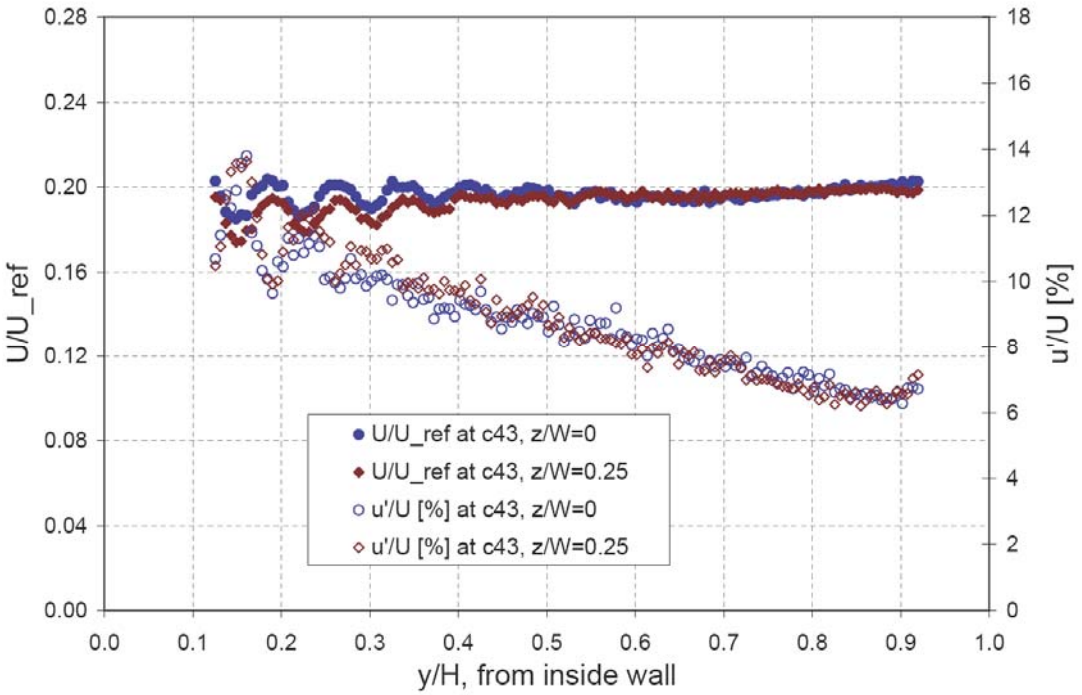

Figure 82. Comparison of streamwise mean velocity and turbulence intensity in the tunnel plane of symmetry (*z/W*=0) and at quarter width (*z/W*=0.25) at corner #4, position 3.

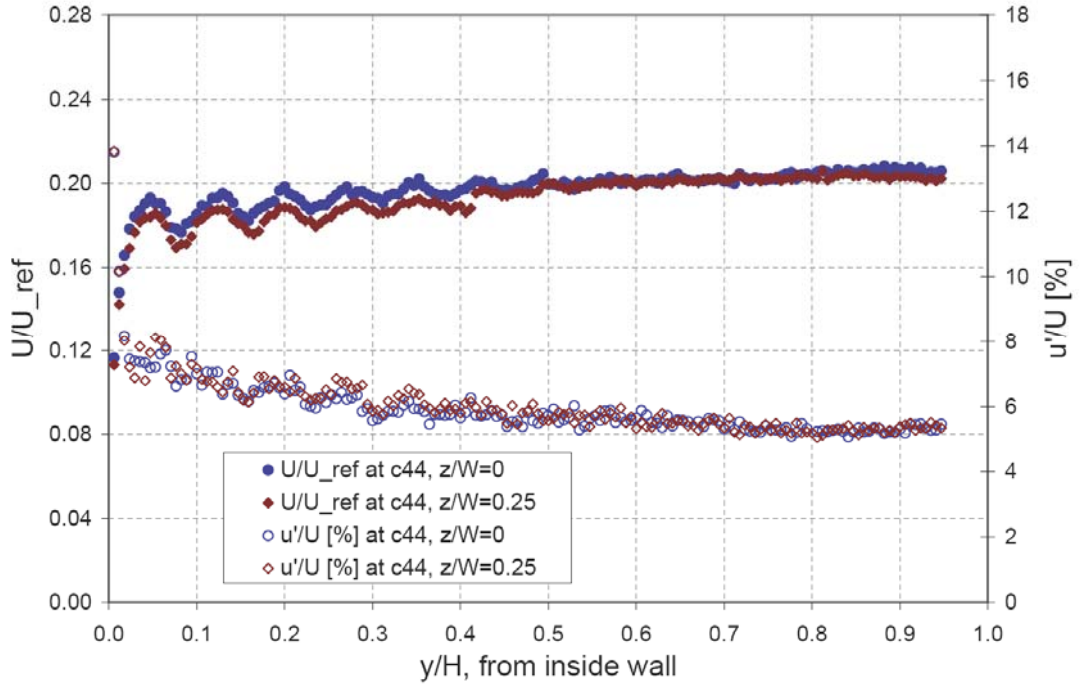

Figure 83. Comparison of streamwise mean velocity and turbulence intensity in the tunnel plane of symmetry (*z/W*=0) and at quarter width (*z/W*=0.25) at corner #4, position 4.

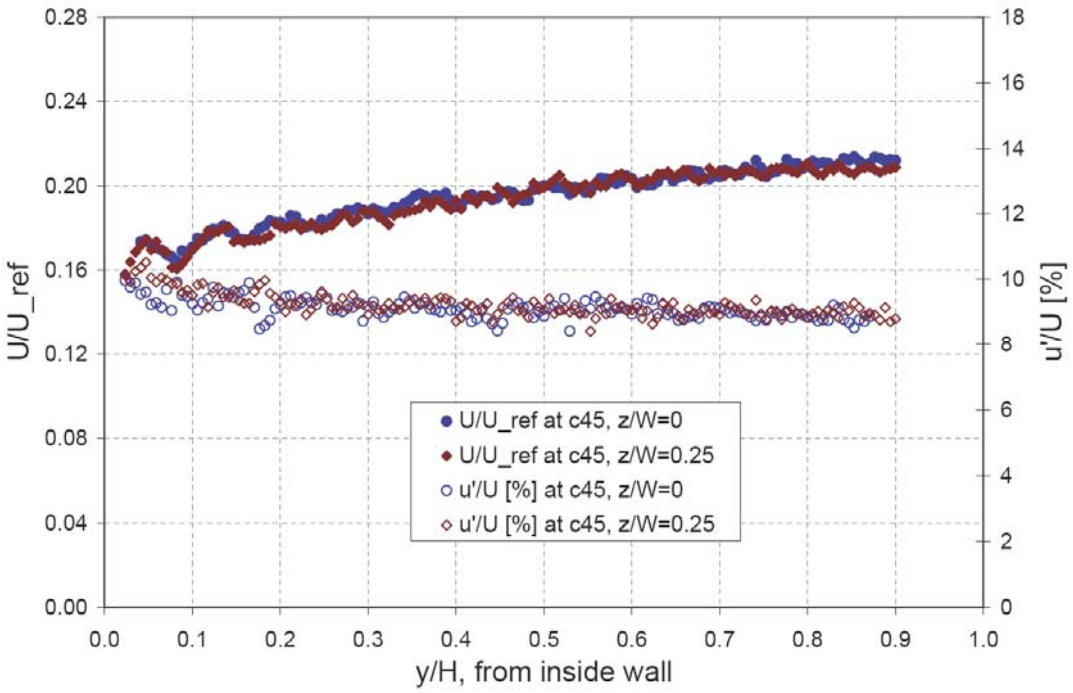

Figure 84. Comparison of streamwise mean velocity and turbulence intensity in the tunnel plane of symmetry (*z/W*=0) and at quarter width (*z/W*=0.25) at corner #4, position 5.

A comparison of streamwise (*U*) and cross-stream (*V*) mean velocity, and streamwise turbulence intensity between the plane of symmetry (*z/W* = 0) and at quarter width (*z/W* = 0.25) at the test section inlet is shown in Figure 85. All three quantities match up very well between *z/W* = 0 and *z/W* = 0.25, further proof that the flow in the test section is very uniform. Streamwise (*U*) and cross-stream (*V*) mean velocity, and streamwise turbulence intensity at the test section exit are compared between the plane of symmetry (*z/W*=0) and at quarter width (*z/W*=0.25) in Figure 86, again matching up very well.

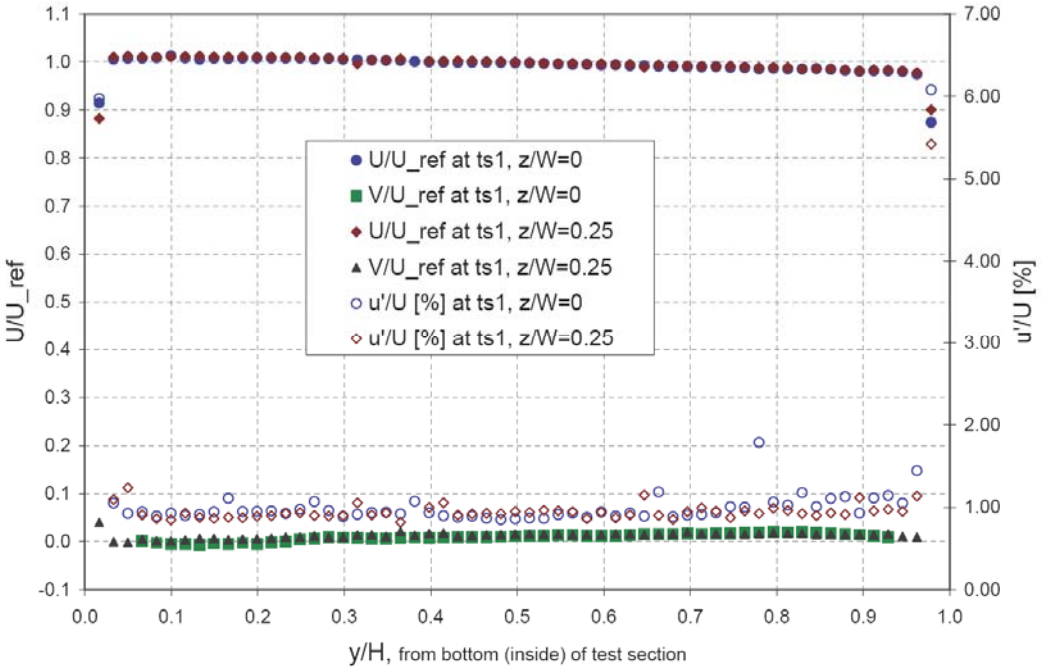

Figure 85. Comparison of streamwise (*U*) and cross-stream (*V*) mean velocity, and streamwise turbulence intensity at the test section inlet in the plane of symmetry (*z*/*W*=0) and at quarter width (*z*/*W*=0.25).

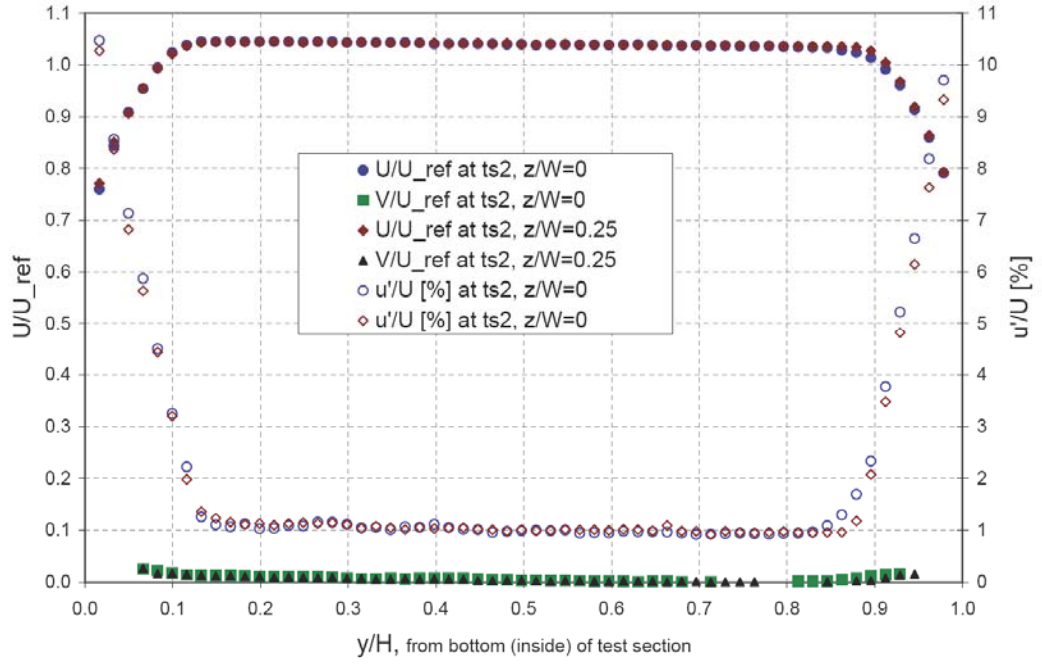

Figure 86. Comparison of streamwise (*U*) and cross-stream (*V*) mean velocity, and streamwise turbulence intensity between the plane of symmetry (*z*/*W*=0) and at quarter width (*z*/*W*=0.25) at the test section exit.

In Figure 87 the streamwise mean velocity (U) and streamwise turbulence intensity at corner #1, position 1 (before turning vanes), are compared in in the plane of symmetry ($z/W = 0$) and at quarter width ($z/W = 0.25$). The maximum velocity at $z/W = 0.25$ is not as high as at $z/W = 0$, because the position $z/W = 0.25$ is within the thick boundary layer created by the diffuser. Accordingly, the local turbulence intensities are higher, since they are computed with a lower mean reference velocity. Outside of the center, values for both the mean velocities and the turbulence intensities compare well.

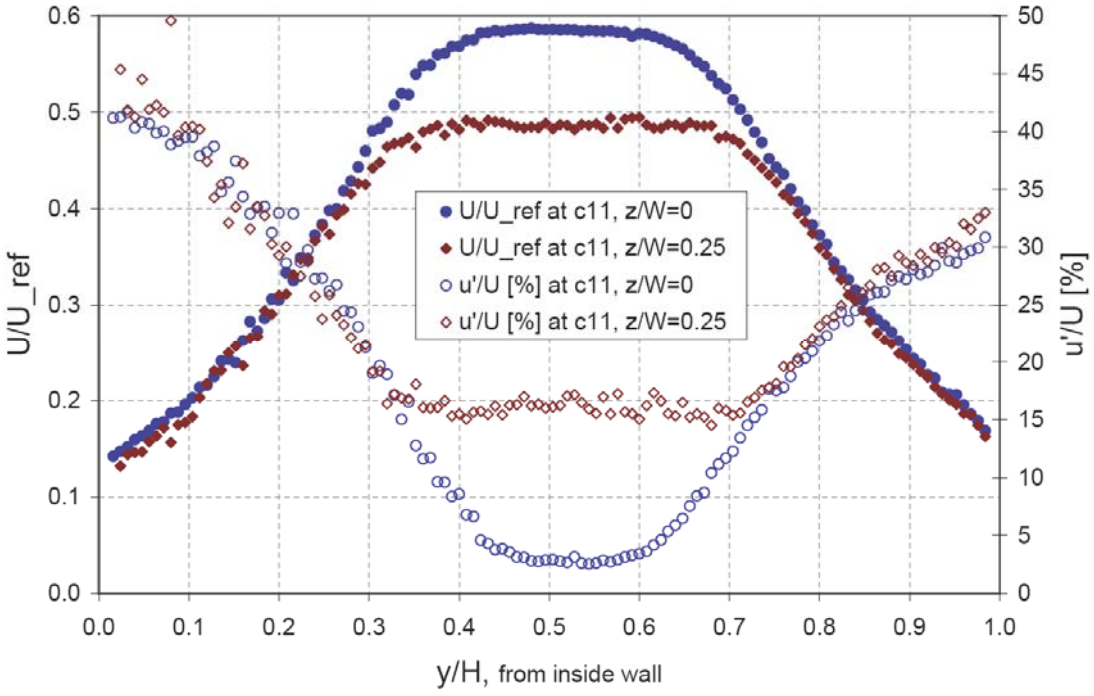

Figure 87. Comparison of streamwise mean velocity (U) and streamwise turbulence intensity at corner #1, position 1 (before turning vanes), in the plane of symmetry (z/W=0) and at quarter width (z/W=0.25).

In Figure 88 the streamwise mean velocity (U) and streamwise turbulence intensity at corner #1, position 2 (after turning vanes), are compared in the plane of symmetry ($z/W = 0$) and at quarter width ($z/W = 0.25$). The lower mean velocity in the center of the flow at $y/W = 0.25$ is also seen in Figure 88, as the thick boundary layers created by the diffusers are carried through the turning vanes. When comparing the mean velocities between $z/W = 0$ and $z/W = 0.25$ it can be seen that the wakes of the turning vanes are not horizontal (in prototype orientation), but are slightly skewed.

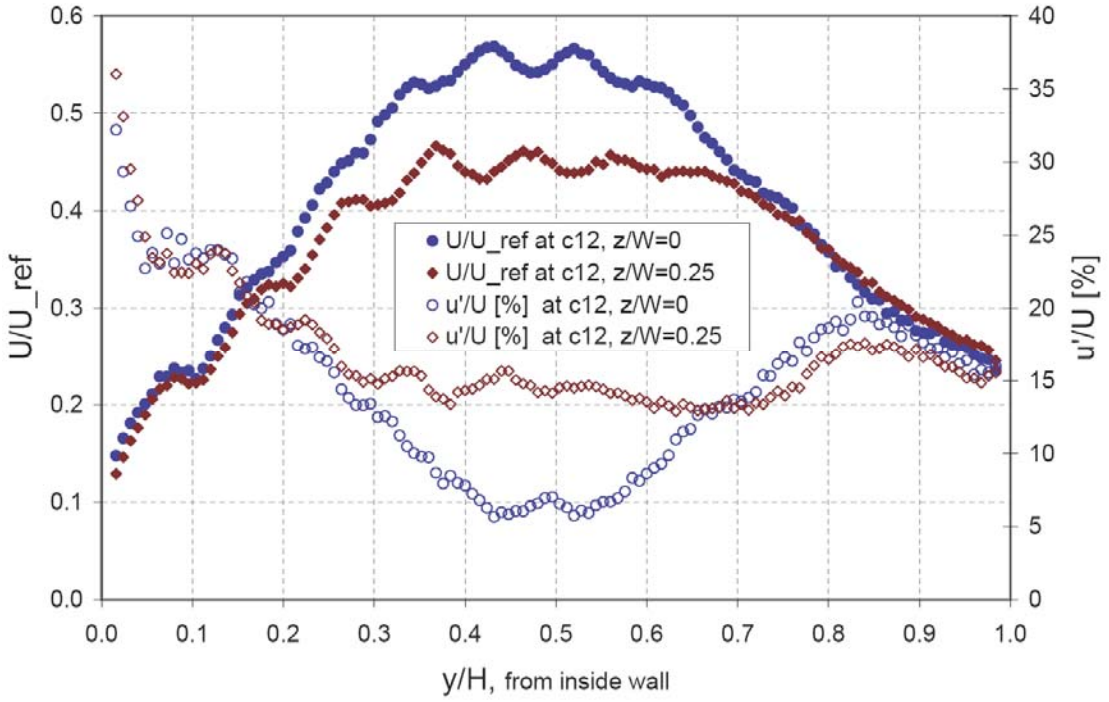

Figure 88. Comparison of streamwise mean velocity (U) and streamwise turbulence intensity at corner #1, position 2 (after turning vanes), in the plane of symmetry (z/W=0) and at quarter width (z/W=0.25).

5. Summary and recommendations

An experimental analysis and verification of the LOCAT design was carried out at St. Anthony Falls Laboratory (SAFL). Detailed pressure and velocity measurements were performed in a 1:6 scale physical model using air as a working fluid. High spatial resolution mean velocity and turbulence profiles were measured at 44 locations in the model, and mean pressure was measured at 183 locations.

The overall flow quality is satisfactory except a larger than expected variation of the mean flow in the test section. The flow in the diffuser is a highly turbulent adverse pressure gradient boundary layer, but does not separate. The turning vanes in corners #1 and #2 appear to still slightly under-turn the flow at 2 degree off design angle of attack (in an aerodynamic sense); additionally, asymmetries present in the mean flow before the corner are carried through the turning vanes. At the pump inlet, the flow is skewed towards the outside of the pipe and the wake signature of the pump shaft is still present; however, the flow is uniform enough for common pump designs to handle.

Measurements at the plane of symmetry and the quarter plane compared favorably; the flow in the LOCAT model is reasonably uniform at rectangular cross sections. In a sense, this 1:31 scale, low Reynolds number dynamical model provides a worst-case scenario for the design goals that were not achieved in the model study, and it is expected that the LOCAT design will perform better at prototype Reynolds numbers. However, several results of this model study should be looked at more carefully, and some small design modifications should be considered.

The installation of corner fillets, on the order of 5% of local height, may be helpful to prevent secondary flows in the corners (corner vortices), which may affect the performance of contraction and test section.

In section 4.3 it was shown that the wakes of the turning vanes persist through both honeycombs. It is recommended that the first honeycomb be placed further downstream from the turning vanes of corner #4 and that both honeycombs be given adequate space for the honeycomb-generated turbulence to decay (a minimum of 40 mesh sizes, preferably more). The turbulence management section was shortened by 1.5m (prototype) in the design process. If at all possible, it

is suggested to bring it back closer to the original length. Further study is recommended for the performance of the turbulence management system. One issue that should be looked at more carefully is how non-uniform turbulence intensity will affect the mean velocity profile as it goes through a honeycomb.

The results of the physical model presented here can be used for further comparison to numerical simulations at model Reynolds number, which can then be extrapolated to prototype Reynolds numbers to predict the performance of the full scale LOCAT.

References

Blake WK (1983) Differential Pressure Measurement. In Fluid Mechanics Measurements, Goldstein RJ, editor, Hemisphere Publishing.

Song CSS; Wetzel JM; Yuan M; Arndt REA; Killen JM (1987) Hydrodynamic Analysis of the HYKAT. Project Report No. 261, St. Anthony Falls Hydraulic Laboratory, University of Minnesota, June 1987.

Song CSS; Wetzel JM; Killen JM; Arndt REA (1988) Physical and Mathematical Modeling of the HYKAT. Project Report No. 282, St. Anthony Falls Hydraulic Laboratory, University of Minnesota, December 1988.

Song CSS (2006) Preliminary results of numerical modeling of LOCAT. Presented at meeting between J. Kim, R. Arndt, C. Song and M. Wosnik at St. Anthony Falls Laboratory, University of Minnesota, 19 April 2006.

Wetzel J; Arndt REA (1994) Hydrodynamic Design Considerations for Hydroacoustic Facilities: I. Flow Quality. J Fluids Engineering, vol.116.

Wetzel J; Arndt REA (1994) Hydrodynamic Design Considerations for Hydroacoustic Facilities: I. Pump Design Factors. J Fluids Engineering, vol.116.

Wosnik M; Ding A; Plante M; Ellis C; Barnacle T; Mullin J; Christopher D; Mohseni O (2006) Design and construction of a 1:6 scale physical model of a large, low-noise cavitation tunnel (LOCAT), Project Report No. 487, St. Anthony Falls Hydraulic Laboratory, University of Minnesota, November 2006.